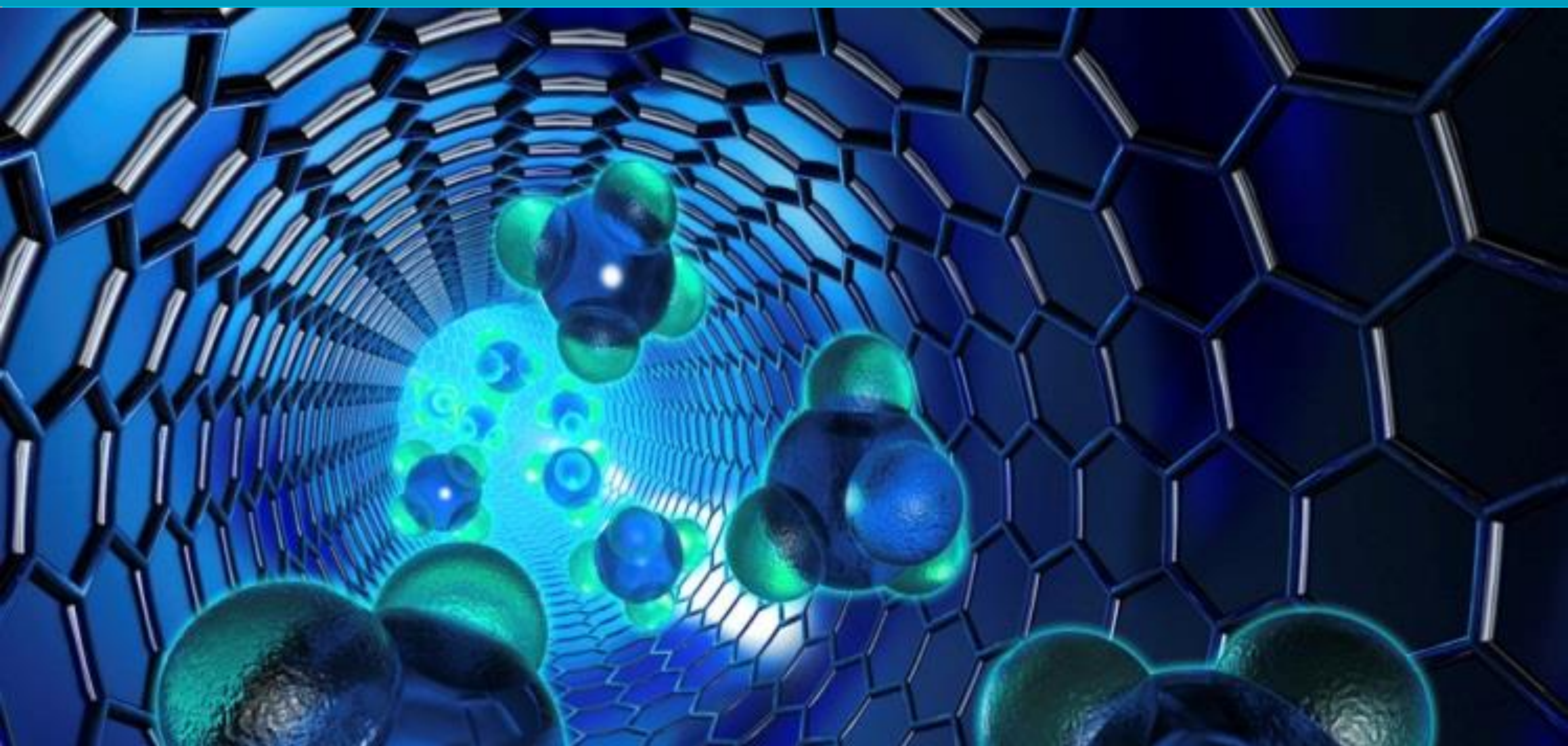


e-ISSN: 2602-277X

International Journal of Chemistry and Technology



Volume:3, Issue:2

31 December 2019

E - Journal

<http://dergipark.org.tr/ijct>

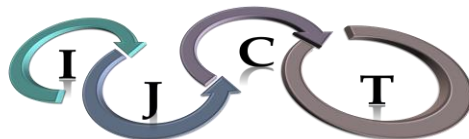


International Journal of Chemistry and Technology

JOURNAL INFO

Journal Name	International Journal of Chemistry and Technology
Journal Initial	IJCT
Journal Abbreviation	Int. J. Chem. Technol.
ISSN (Online)	2602-277X
Year of Launching	2017, August
Editor-in-Chief and Managing Editor	Prof. Dr. Bilal Acemioğlu
Manager of Publication	Assist. Prof. Mehmet Akyüz
Scope and Focus	Chemistry, Material Science, Technology
Review Type	Peer Review Double-Blinded
Ethical Rules	Plagiarism check, copyright agreement form, conflict of interest, ethics committee report
Access Type	Open Access
Publication Fee	Free
Article Language	English
Frequency of Publication	Biannually
Publication Issue	June, December
Publisher	Prof. Dr. Bilal Acemioğlu
Web Page	http://dergipark.org.tr/ijct
Contact E-mail address	ijctsubmission@gmail.com, ijctsubmission@yahoo.com
Contact Address and Executive address	Kilis 7 Aralik University, Faculty of Science and Arts, Department of Chemistry, 79000, Kilis
Contact Telephone	90 5535983054 (Editor-in-Chief), 90 530 3645222 (Manager of Publication), 90 532233 17 38 (Secretary)
Publication Date	31/12/2019
Technical Editor	Assist. Prof. Dr. Evrim Baran Aydın
Spelling Editor	Dr. Oğuzhan Koçer, MSc. Rabia Acemioğlu
Language (Grammar) Editor	Assit. Prof. Dr. Muhittin Kulak, Assist. Prof. Dr. Muhammet Karaman, Msc. Lawali Yabo Dambagi
Secretary	Dr. Oğuzhan Koçer, MSc. Rabia Acemioğlu

All detailed information including instructions for authors, aim and scopes, ethical rules, manuscript evaluation, indexing info, and manuscript template etc. can be found on the main web page of IJCT (<http://dergipark.org.tr/ijct>).



International Journal of Chemistry and Technology

Volume: 3, Issue: 2, 31 December 2019

Founder of IJCT

Prof. Dr. Bilal Acemiođlu

EDITORIAL BOARD

Editor-in-Chief

Prof. Dr. Bilal Acemiođlu

(Physical Chemistry, Kilis 7 Aralık University, Kilis, Turkey)

Associate Editors

Prof. Dr. İbrahim Demirtaş
(Organic Chemistry and Phytochemistry,
İğdır University, İğdır, Turkey)

Prof. Dr. M. Hakkı Alma
(Material Science and Technology,
K.Maraş Sütçü İmam/İğdır University, Turkey)

Prof. Dr. Ekrem Köksal
(Biochemistry, Erzincan Binali Yıldırım University,
Erzincan, Turkey)

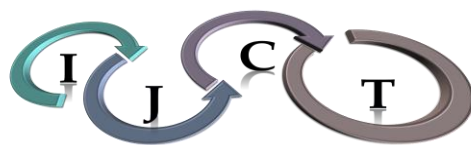
Prof. Dr. Fevzi Kılıçel
(Analytical Chemistry, Karamanođlu Mehmet
Bey University, Karaman, Turkey)

Prof. Dr. Yuh-Shan Ho
(Chemical and Environmental Engineering,
Asia University, Taichung City, Taiwan)

Prof. Dr. Yahya Güzel
(Theoretical Chemistry and Polymer Chemistry,
Erciyes University, Kayseri, Turkey)

Prof. Dr. Mustafa Arık
(Physical Chemistry, Atatürk University,
Erzurum, Turkey)

Prof. Dr. Mehmet Sönmez
(Inorganic Chemistry, Gaziantep University,
Gaziantep, Turkey)



International Journal of Chemistry and Technology

Advisory Editorial Board

Prof. Dr. Harun Parlar
(Technical University of Munich, München,
Germany)

Prof. Dr. Shaobin Wang
(Curtin University, Perth, Australia)

Prof. Dr. Ana Beatriz Rodriguez Moratinos
(University of Exramadura, Badajoz, Spain)

Prof. Dr. Jon-Bae Kim
(College of Health Sciences, South Korea)

Prof. Dr. Rashid Ahmad
(University of Malakand, Chakdara, Pakistan)

Prof. Dr. Guang-Jie Zhao
(Beijing Forestry University, Beijing, China)

Prof. Dr. Jaine H. Hortolan Luiz
(Federal University of Alfenas, Unifal-MG, Brazil)

Prof. Dr. Papita Das
(Jadavpur University, Jadavpur, India)

Prof. Dr. Vagif Abbasov
(Nef-Kimya Prosesleri Institutu, Baku, Azerbaijan)

Prof. Dr. Atiqur Rahman
(Islamic University, Kushita, Bangladesh)

Prof. Dr. Mika Sillanpaa
(LUT Lappeenranta University of Technology,
Lappeenranta, Finland)

Prof. Dr. Salah Akkal
(University of Mentouri Consatntine,
Consatntine, Algeria)

Prof. Dr. Gilbert Kapche Deccaux
(University of Yaounde I, Yaounde, Cameroon)

Prof. Dr. Gelu Bourceanu
(Alexandru Ioan Cuza University, Romania)

Prof. Dr. Ahmet Çakır
(Kilis 7 Aralık University, Kilis, Turkey)

Prof. Dr. M. Salih Ağırtaş
(Yüzüncü Yıl University, Van, Turkey)

Prof. Dr. Nurullah Saraçoğlu
(Atatürk University, Erzurum, Turkey)

Prof. Dr. Rahmi Kasımoğulları
(Dumlupınar University, Kütahya, Turkey)

Prof. Dr. Ahmet Baysar
(Inonu University, Malatya, Turkey)

Prof. Dr. Hamdi Temel
(Dicle University, Diyarbakır, Turkey)

Prof. Dr. Ö. İrfan Küfrevioğlu
(Atatürk University, Erzurum, Turkey)

Prof. Dr. Ömer Şahin
(Siirt University, Siirt, Turkey)

Prof. Dr. Anatoli Dimoglu
(Düzce University, Düzce, Turkey)

Prof. Dr. Mehmet Uğurlu
(Sıtkı Kocman University, Muğla, Turkey)

Prof. Dr. Şükrü Beydemir
(Anadolu University, Eskişehir, Turkey)

Prof. Dr. Ramazan Solmaz
(Bingöl University, Bingöl, Turkey)

Prof. Dr. Mahfuz Elmastaş
(Health Sciences University, İstanbul, Turkey)

Prof. Dr. Mehmet Doğan
(Balıkesir University, Balıkesir, Turkey)

Prof. Dr. Giray Topal
(Dicle University, Diyarbakır, Turkey)

Prof. Dr. Birgül Yazıcı
(Cukurova University, Adana, Turkey)



International Journal of Chemistry and Technology

Advisory Editorial Board

Prof. Dr. Mehmet Muhtar Kocakerim
(Çankırı Karatekin University, Çankırı, Turkey)

Prof. Dr. Murat Alanyalıoğlu
(Atatürk University, Erzurum, Turkey)

Prof. Dr. T. Abdulkadir Çoban
(Erzincan Binali Yıldırım University, Erzincan, Turkey)

Prof. Dr. İsmet Kaya
(18 Mart University, Çanakklae, Turkey)

Prof. Dr. Barbaros Nalbantoğlu,
(Yıldız Technical University, İstanbul, Turkey)

Prof. Dr. Ömer Işıldak
(Gaziosmanpaşa University, Tokat, Turkey)

Prof. Dr. Halim Avcı
(Kilis 7 Aralık University, Kilis, Turkey)

Prof. Dr. Ahmet Tutar
(Sakarya University, Sakarya, Turkey)

Prof. Dr. Duygu Ekinci
(Atatürk University, Erzurum, Turkey)

Prof. Dr. Metin Bülbül
(Dumlupınar University, Kütahya, Turkey)

Prof. Dr. Ali Kara
(Uludağ University, Bursa, Turkey)

Assoc. Prof. Dr. Mahjoub Jabli
(University of Monastir, Monastir, Tunisia)

Assoc. Prof. Niyaz M. Mahmoodi,
(Institute for Color Science and Technology, Tehran, Iran)

Assoc. Prof. Chin-Hung Lai (Chung Shan Medical University, Taiwan)

Assoc. Prof. Dr. Şenay Şimşek
(North Dakota State University, Fargo, USA)

Assoc. Prof. Dr. Metin Açıkyıldız
(Kilis 7 Aralık University, Kilis, Turkey)

Assoc. Prof. Dr. Muhammet Köse
(Sütçü İmam University, K.Maraş, Turkey)

Assoc. Prof. Dr. Mustafa Karataş
(Aksaray University, Aksaray, Turkey)

Assoc. Prof. Dr. Serhan Uruş
(Sütçü İmam University, K.Maraş, Turkey)

Assoc. Prof. Dr. Murat Saraçoğlu
(Erciyes University, Kayseri, Turkey)

Assoc. Prof. Dr. Murat Sadıkoğlu
(Gaziosman Paşa University, Tokat, Turkey)

Assoc. Prof. Dr. Mustafa Özdemir
(Süleyman Demirel University, Isparta, Turkey)

Assist. Prof. Dr. Mutasem Z. Bani-Fwaz
(King Khalid University, Asir-Abha, Saudi Arabia)

Assist. Prof. Masood Ayoub Kaloo
(Govt. Degree College Shopian, J &K, India)

Dr. Zineb Tribak
(Sidi Mohamed Ben Abdellah University, Fez Morocco)

Assist. Prof. Dr. Bakhtiyor Rasulev
(North Dakota State University, Fargo, USA)

Dr. Ramadan E. Ashery
(Damanhour University, Egypt)

Dr. Sameer Ahmed Awad
(University of Anbar, Ramadi, Iraq)



International Journal of Chemistry and Technology

Reviewers for December 2019, Vol: 3, Issue: 2

- | | |
|---|--|
| Prof. Dr. Mahfuz Elmastaş
(University of Health Sciences, İstanbul, Turkey) | Prof. Dr. Suna Erdoğan
(Hacettepe University, Ankara, Turkey) |
| Prof. Dr. Şükrü Beydemir
(Anadolu University, Eskişehir, Turkey) | Prof. Dr. Kani Arıcı
(Kilis 7 Aralık University, Kilis, Turkey) |
| Prof. Dr. Şükrü Karataş
(Sütçü İmam University, Kahramanmaraş, Turkey) | Prof. Dr. Şükrü Özğan
(Sütçü İmam University, Kahramanmaraş, Turkey) |
| Prof. Dr. Nezir Yıldırım
(Bingöl University, Bingöl, Turkey) | Prof. Dr. Kemal Güven
(Dicle University, Diyarbakır, Turkey) |
| Prof. Dr. Anatoli Dimoglo
(Düzce University, Düzce, Turkey) | Prof. Dr. İlhami Gülçin
(Atatürk University, Erzurum, Turkey) |
| Prof. Dr. Hamdi Karaoğlu
(Muğla Sıtkı Koçman University, Muğla, Turkey) | Prof. Dr. Ekrem Köksal
(Erzincan Binali University, Erzincan, Turkey) |
| Assoc. Prof. Dr. Hamit Alyar
(Çankırı Karatekin University, Çankırı, Turkey) | Assoc. Prof. Dr. Murat Saraçoğlu
(Erciyes, Kayseri, Turkey) |
| Assoc. Prof. Dr. Ali Şamil
(Sütçü İmam University, Kahramanmaraş, Turkey) | Assist Prof. Dr. Ahmet Altay
(Erzincan Binali University, Erzincan, Turkey) |
| Assoc. Prof. Dr. Hakan Söyüt
(Uludağ University, Bursa, Turkey) | Assist. Prof. Dr. Mustafa Okant
(Harran University, Şanlıurfa, Turkey) |
| Assist Prof. Dr. Mutasem Z. Bani-Fwaz
(King Khalid University, Saudi Arabia) | |



International Journal of Chemistry and Technology

TABLE OF CONTENTS

Review Articles	Pages
1. Quality and composition of lipids used in biodiesel production and methods of transesterification: A review (Biyodizel üretiminde kullanılan yağların kalitesi, kompozisyonu ile transesterifikasyon yöntemleri: Bir derleme) Ihsan Ekin	77-91
Research Articles	Pages
2. Recombinant human G-CSF production as a protein based drug candidate for hematology and oncology (Hematoloji ve onkoloji için protein esaslı bir ilaç adayı olarak rekombinant insan G-CSF üretimi) Yasemin Bozkurt, Sema Bilgin, Seçil Erden Tayhan, İsmail Furkan Turan, İsa Gökçe	92-100
3. Variation of Coster-Kronig enhancement factors at different excitation energies of the elements in the atomic number range $41 \leq Z \leq 49$ (Atom numarası $41 \leq Z \leq 49$ arasındaki elementlerin farklı uyarma enerjilerinde Coster-Kronig şiddetlendirme faktörlerinin değişimi) Rafet Yılmaz, Turgay Özmen, Tahir Çakır	101-112
4. Cytotoxic activity of zinc oxide/titanium dioxide nanoparticles on prostate cancer cells (Çinko oksit/titanyum dioksit nanopartiküllerin prostat kanser hücreleri üzerinde sitotoksik aktivitesi) Ayca Tas, Nese Keklikcioglu Cakmak, Tugba Agbektas, Yavuz Silig	113-120
5. Quantitative modeling for prediction of boiling points of phenolic compounds (Fenolik bileşiklerin kaynama noktalarının belirlenmesi için kantitatif modelleme) Soumaya Kherouf, Nabil Bouarra, Djelloul Messadi	121-128
6. Effect of measurement frequency on admittance characteristics in Al/p-Si structures with interfacial native oxide layer (Doğal oksit arayüzey tabakalı Al/p-Si yapılarında admittans karakteristikleri üzerine ölçüm frekansının etkisi) Muhammed Can Özdemir, Ömer Sevgili, İkram Orak, Abdülmecit Türüt	129-135
7. Adsorption of basic red 2 dye by activated biomass charcoal in batch and column systems (Bazik kırmızı 2 boyasının kesikli ve kolon sistemlerinde aktifleştirilmiş biyokütle kömürü tarafından adsorpsiyonu) Bilal Acemioğlu, Neslihan Karataş, Melike Hilal Güler, Murat Ertaş, Mehmet Hakkı Alma	136-145

8. Inhibition effects of commonly used some antibacterial and antiviral drugs on purified human serum paraoxonase-1 (hPON1) 146-150
(Sık kullanılan bazı antibakteriyel ve antiviral ilaçların saflaştırılmış insan serum paraoksonaz-1 (hPON1) üzerine inhibisyon etkileri)
Hakan Soyut
9. The substituent group activity in the anion of cholinium carboxylate ionic liquids on thermo-physical, chemical reactivity, and biological properties: A DFT study 151-161
(Kolinium karboksilat iyonik sıvıların anyonundaki süstitüe grubun thermo-fiziksel, kimyasal reaktivite ve biyolojik özellikler üzerine aktivitesi: Bir DFT çalışması)
Afroza Zannat, Ajoy Kumar, Md. Nuruzzaman Sarker, Sunanda Paul



Quality and composition of lipids used in biodiesel production and methods of transesterification: A review

İhsan EKİN*

on the last page

Department of Energy System Engineering, Engineering Faculty, Şırnak University, Şırnak, Turkey

Received: 22 September 2019; Revised: 16 October 2019; Accepted: 18 October 2019

*Corresponding author e-mail: ekinihsan@gmail.com

Citation: Ekin, İ. <i>Int. J. Chem. Technol.</i> 2019, 3 (2), 77-91.

ABSTRACT

This study presents a brief overview of the composition and properties of various oils used in biodiesel production and the alkali, acidic and enzymatic transesterification reactions used in production. Nowadays, vegetable and microalgae oils are mostly used in biodiesel production. Recently, however, animal fats, processed oils, industrial oils and yeast and bacterial oils have also gained importance. Although all fats and oils are roughly similar, their saturated fatty acids (SFA), polyunsaturated fatty acids (PUFA), monounsaturated fatty acids (MUFA), free fatty acids (FFA), cholesterol or glycerol contents may be different and affect the production and efficiency of the biodiesel. Triglycerides are the most significant lipids in biodiesel production. Triglycerides in vegetable oils dominantly contain C18:1 ω 9 and C18:2 ω 6 fatty acids. Whereas, triglycerides in animal fats mostly include C16:0 and C18:1 ω 9 fatty acids. Microalgae are rich in long-chain fatty acids such as C20 and C22. Also, fatty acids such as C14:0, C16:1 ω 7, C18:0, C20:0, C22:0, C24:0, C22:1 ω 9, C18:3 ω 6, C20:4 ω 6 and C20:5 ω 6 are present in oils and fats. However, their proportions change from feedstock to feedstock. Rendered animal-originated fats include larger quantities of FFA than waste vegetable oils and, as known, excessive amounts of FFA generate soap in reactions with the alkaline catalyst, reducing biodiesel efficiency. For this reason, generally vegetable and microalgal oils containing a large number of triglycerides and less FFA are preferred for biodiesel production. Bacteria can synthesize branched fatty acids. It has been reported that biodiesel produced from branched fatty acids has advantages according to biodiesel produced from other lipids. Consequently, the use of correct and reliable lipids in biodiesel production is very important for the quality of fuel.

Keywords: Fatty acids, lipid feedstocks, biodiesel, transesterification.

Biyodizel üretiminde kullanılan yağların kalitesi, kompozisyonu ile transesterifikasyon yöntemleri: Bir derleme

ÖZ

Bu çalışma, biyodizel üretiminde kullanılan çeşitli yağların kompozisyonu ve özelliği ile üretimde kullanılan alkali, asidik ve enzimatik transesterifikasyon reaksiyonlarına kısa bir bakış sunmaktadır. Günümüzde, bitkisel ve mikroalg yağları çoğunlukla biyodizel üretiminde kullanılmaktadır. Ancak son zamanlarda hayvansal yağlar, işlenmiş yağlar, endüstriyel yağlar ve maya ve bakteri yağları da önem kazanmıştır. Bütün sıvı ve katı yağlar kabaca birbirine benzer olsada, onların doymuş yağ asiti (DYA), çoklu doymamış yağ asiti (ÇDYA), tekli doymamış yağ asiti (TDYA), serbest yağ asiti (SYA), kolesterol ve gliserol içerikleri farklı olabilir ve bu da biyodizel üretimini ve verimini etkiler. Trigliseritler biyodizel üretiminde en önemli lipitlerdir. Bitkisel yağlardaki trigliseritler, baskın olarak C18:1 ω 9 ve C18:2 ω 6 yağ asitlerini içerirler. Oysa hayvansal yağlardaki trigliseritler çoğunlukla C16:0 ve C18:1 ω 9 yağ asitlerini ihtiva ederler. Mikroalgler C20 ve C22 gibi uzun zincirli yağ asitleri bakımından zengindirler. Ayrıca, C14:0, C16:1 ω 7, C18:0, C20:0, C22:0, C24:0, C22:1 ω 9, C18:3 ω 6, C20:4 ω 6 ve C20:5 ω 6 gibi yağ asitleri, katı ve sıvı yağların çoğunda bulunurlar. Fakat oranları hammaddeden hammaddeye değişmektedir. İşlenmiş hayvan kaynaklı yağlar, atık bitkisel yağlardan daha büyük miktarlarda FFA içerir ve bilindiği üzere, aşırı miktarda FFA, alkali katalizörle reaksiyonlarda sabun üreterek biyodizel verimliliğini azaltır. Bu nedenle, genel olarak çok sayıda trigliserit ve daha az FFA içeren bitkisel ve mikroalgal yağları biyodizel üretimi için tercih edilir. Bakteriler ise dallanmış yağ asitlerini sentezleyebilirler. Dallanmış yağ asitlerinden üretilen biyodizelin, diğer yağlar ile üretilen biyodizellere göre avantajlara sahip olduğu rapor edilmiştir. Sonuç olarak, biyodizel üretiminde doğru ve güvenilir lipidlerin kullanılması yakıtın kalitesi için çok önemlidir.

Anahtar Kelimeler: Yağasitleri, lipit ham maddeleri, biyodizel, transesterifikasyon.

1. INTRODUCTION

Lipids can be classified into three groups, simple lipid (neutral lipids), complex lipid (phospholipids, lipoproteins, glycolipids), and primary lipid (fatty acids and sterols). In detail, lipids contain a variety of structural types, including fatty acids, triglycerides, diglycerides, monoglycerides, lipoprotein, glycolipids, terpenoids, terpenes, steroids, sphingolipids, phospholipids, eicosanoids, and waxes. They are often known by high solubility in nonpolar solvents such as chloroform, hexane and diethyl ether.

Physically, fats are solid and oils are liquid at room temperature. Lipids from fats and oils include triglycerides synthesized from three long-chain fatty acids and a glycerol molecule. Because of the high viscosity of the lipids, they cannot be directly used as fuel in a standard diesel engine. For this reason, triglycerides are converted into fatty acid methyl esters (FAME) by transesterification reaction to reduce viscosity. Hence, three molecules of FAME and one molecule of glycerine are picked up from one molecule of triglycerides. Glycerine is taken away as by-product, and FAME is used as biodiesel.¹

Most of the lipids are comprised of fatty acids containing long saturated or unsaturated aliphatic hydrocarbon chains and a terminal carboxyl group. Fatty acids generally have unbranched chains with even number of carbon atoms, usually 14 to 28 carbon-containing and they are mostly found in triglycerides and phospholipids. Saturated carbon chains containing fatty acids are called fats (mostly found in animals) having higher melting points than the unsaturated ones like vegetable oils. If a single fatty acid is not bonded to other molecules, it is called free fatty acid (FFA). The major fatty acids of the feedstocks are stearic (C18:0), palmitic (C16:0), oleic (C18:1 ω 9) and linoleic (C18:2 ω 6) acids with a low degree of unsaturation. It has been reported that density and viscosity of biodiesel can be predicted by the fatty acid profile of feedstock. If the main fatty acids of the feedstock have a long chain of carbon and low degree of unsaturation, the viscosity of the biodiesel will be high, and vice versa. Consequently, the increasing number of double bonds and reducing chain length make density higher.²

Biodiesel consists of a mixture of fatty acid formed chain length between C14-C22 alkyl esters, obtained from a sustainable lipid feedstock, such as animal fat, vegetable or algae oil. Just in case of using ethanol or methanol as reactants, the mixture of fatty acid ethyl esters (FAEE) or FAME is formed, respectively. By any means, methanol is generally used in transesterification reactions by its low-priced and availability. Sometimes butanol and isopropanol might also be used in transesterification reactions instead of conventional alcohol. Water content is the main factor for primary alcohol. Water is not good for biodiesel production because it can give rise to poor yields and converts FFA

and triglycerides to soap.³ FAME is the most important part of biodiesel and can be used in conventional diesel engines with no significant modifications. The advantages of biodiesel over diesel fuel are its non-toxic feature, higher combustion performance, biodegradability, renewability, higher cetane number, portability, easy availability, lower aromatic and sulfur content, safer handling and better emission profile.^{4,5} Compared to petroleum-based fuels, biodiesel is less toxic and has a low environmental impact with its emissions and does not include sulfur, therefore SO_x is not emitted. On the other hand, proper combustion can be achieved because of the high flash point of biodiesel and producing lower emissions of hydrocarbons, CO, CO₂, and NO₂.

High-quality vegetable oils such as soybean, sunflower, rapeseed (canola), corn, and safflower are generally used as biodiesel raw materials. These raw materials have a high-cost, which is currently responsible for 85% of biodiesel production expenses.⁶ Recently, a variety of investigations are released on biodiesel production from low-priced feedstocks. Therefore, there are a lot of explorations on new generation oily seeds, rendered and frying oils, different animal fats, algae oils, and microbial lipids. The most efficient and low-priced feedstock has not been advanced exactly.⁷ More than 95% of total biodiesel production is edible oil feedstock. For example, sunflower oils (13%) and rapeseed oils (84%) are major feedstock in biodiesel synthesis followed by palm oil (1%). The other is produced from groundnut, corn, coconut, peanut, soybean, and canola (2%).⁸ Some of the non-edible oil sources utilized for biodiesel are rubber (*Ficus elastica*), *Jatropha* (*Jatropha curcas*), karanja (*Milletia pinnata*), polanga (*Calophyllum inophyllum*), tobacco (*Nicotiana tabacum*), castor (*Ricinus communis*) and mahua.⁹⁻¹¹ Animal-originated products such as poultry fat, tallow, and lard have also been explored for their capacities as raw materials of biodiesel.^{7,12} The restaurants and food processing oils such as rendered cooking oil and other waste oil have been evaluated as feedstock.¹³ Animal fats derived biodiesel has the superiority of a higher cetane number, the most significant indicator of diesel combustion property as compared to vegetable originated biodiesel.¹⁴ Nonetheless, the biodiesel from animal fats has higher cold filter plugging point due to the high content of saturated fatty acids,¹⁵ and it is less stable to oxidation owing to the lack of natural antioxidants which is mostly found in the biodiesel from vegetable oil.¹⁶ Thereby, biodiesel from animal fat may not be appropriate to use it 100% pure in vehicles during cold weather; however, it can be utilized as 100% pure in the boiler systems for heat generation.¹⁷

This review paper describes the lipid composition of all kinds of feedstocks mentioned up to now such as vegetable oil, animal fat, algal oil, waste, and industrial oil and microbial lipids to be used in transeste-

rification reactions for producing biodiesel, as well as comparing the advantages, disadvantages and positive and negative aspects of biodiesel feedstocks. Thence, the purpose of this work is to present an overview of the different type of raw materials adopted for the production of biodiesel, and additionally it describes alkaline, acidic and enzymatic transesterification methods.

2. TYPES OF FEEDSTOCKS AND THEIR QUALITIES

2.1. Composition of vegetable oils as a feedstock for biodiesel

More than 95 % of biodiesel primarily has been obtained from edible vegetable oils, biodiesel first generation, which is substantially obtainable from the agricultural industry.⁹ Most countries are searching for different types of vegetable oils as a supplement for their diesel fuels depending on their climate conditions and soil types. The purpose is to grow plants that are cheaper and have higher oil content. Latterly biodiesel is predominantly produced from rapeseed in Canada, soybean in the USA, sunflower in Europe, palm in Southeast Asia (mainly in Malaysia and Indonesia), and safflower in India and rarely in the Middle East. Furthermore, the rapeseed and the sunflower are produced in the north of Europe and the Mediterranean countries, respectively. Sunflower oil has good properties in biodiesel production. However, to obtain economical biodiesel, the high cost of sunflower oil is a serious problem. For this reason, a large scale of biodiesel production from edible oils has nowadays been of great concern because they compete with food materials.¹⁸ Let's not miss it; the malnourished human proportion is approximately 60% across the world,^{19,20} the largest producers of biodiesel were the European Union, the United States, Brazil, and Indonesia, which used edible oil for about 8.6 million tones of biodiesel production. The approximate development in using edible oil for biodiesel production was 6.6 million tons from 2004 to 2007, which would ascribe to 34% of the increase in global consumption to biodiesel.²⁰ Alternative vegetable oil from *Cynaracurdunculus* (*Cardoon*), *Brassica carinata* (*Ethiopian mustard*), *Camelina sativa*, *Crambeabyssinica*, *Pogianus*, *Jathophacurcas* are recently been the raw material for biodiesel. Additionally, some of the non-edible oils containing plants, e.g. *Jatropha*, *pongamia* and *karanji* play a noteworthy role in resources. Both these plants may be grown on a massive scale on agricultural, degraded or wastelands.²¹

The majority of vegetable oils mostly have shown similar fatty acids profiles, usually dominated with monounsaturated or polyunsaturated fatty acids. On the other hand, they can show similarities in total but also contain differences in detail. Knowing the fatty acid content of a plant helps to achieve a high quality and

efficient biodiesel production. Rapeseed oil is distinguished by low level (7%) of saturated fatty acids and considerable amounts of monounsaturated fatty acids and polyunsaturated fatty acids, including 61% C18:1 ω 9, 21% C18:2 ω 6 and 11% C18:3 ω 3, plant sterols (0.53-0.97%).²² In some other studies, it is stated that rapeseed has contained 60% of C18:1 ω 9 and soybeans have contained 50-60% of C18:2 ω 6 (Table 1).²³ The saturated fatty acid contents of rapeseed, safflower, sunflower, corn, olive, and soybean oil is determined at low levels; however, the ratio of monounsaturated fatty acid in canola and the ratio of polyunsaturated fatty acid in safflower, sunflower, corn, olive, and soybean are detected at a high level. On the other hand, coconut has contained most than 90% saturated fatty acids.²⁴ Soybean contains a significant amount of triglycerides, primer neutral lipids. There is a high content of unsaturated fatty acids in soybean oil, as approximately all the triglyceride molecules contain at least two unsaturated fatty acids.²⁵ Palm oil has equivalent fatty acid compositions in which the level of saturated fatty acid is nearly equal to unsaturated fatty acids. Palmitic acids (44-45%) and C18:1 ω 9 (39-40%) are major fatty acids along with C18:2 ω 6 (10-11%).²⁶ Total ratio of the safflower seed oil ranges between 30 and 45% based on the dry weight and its oil is used by both food industry and food producers. Safflower oil which contains high C18:2 ω 6 ratio is mostly used in human nutrition, however, recent market demand has drastically shifted from the traditional high C18:2 ω 6 to high C18:1 ω 9. High C18:1 ω 9 safflower oil is lower in the saturated fatty acids and higher in the monounsaturated fatty acids compared to olive oil. High C18:1 ω 9 safflower oil has promising solutions for the environment as a pollutant-reducing diesel fuel due to reducing smoke and particulate emissions. In Europe, canola oil is seen as a major source of oil, as well as contributing nearly 85% of the oil for biodiesel production, additionally, sunflower, soybean, and palm oils are the other three important vegetable oils for biodiesel. Some other resources for vegetable oil extraction to be used in biodiesel production are coconut kernel, castor berry, cotton seed, palm pulp, palm kernel oil, peanut grain, and babassu kernel.²⁷ In a study on some non-traditional seed oils, fatty acid profiles of seed oils of 75 plant species having 30% or more fixed oil in their seed/kernel were analyzed. FAMES of the oils from 26 species including *Calophyllum inophyllum*, *Jatropha curcas*, *Pongamia pinnata*, and *Azadirachta indica* showed these plants as most proper species for biodiesel production and they meet the correct definition of biodiesel standards of USA, Germany and European Standard Organization. The FAMES of the other 11 species meet the specification of USA biodiesel standard. It is concluded that perceived plants have a great potential for biodiesel.²⁸

The carbon number of the diesel fuel is roughly,¹⁵ nearly; it is similar to vegetable oil with 14-18 carbons.²⁹

Table 1. The average fatty acid compositions of some vegetable oils and animal fats.²³

Fatty acids	C12:0	C14:0	C16:0	C16:1	C18:0	C18:1	C18:2	C18:3	C20:4	> C20
Vegetable oils										
Soybean	-	0.1	6-10.2	-	2-5	20-30	50-60	-	-	-
Rapeseed	0.2	0.1	3.9	0.2	1.7	60	18.8	9.5	-	4.0
Corn	-	1-2	8-12	0.1	2-5	19-49	34-62	0.7	-	2.0
Olive	-	-	9-10	-	2-3	73-84	10-12	Traces	-	-
Cotton	-	-	20-25	-	1-2	23-35	40-50	Traces	-	-
Animal fats										
Lard	0.1	1-2	23.6-30	2.8	12-18	40-50	7-13	0-1	1.7	1.3
Tallow	0.1	3-6	23.3-32	4.4	19-25	37-43	2-3	0.6-0.9	0.2	1.8
Fish	0.2	6.1	14.3	10.0	3.0	15.1	1.4	0.7	0.7	56.5
Butter	-	7-10	24-26	-	10-13	1-2.5	2-5	-	-	-
Chicken	0.1	1-1.3	17-20.7	5.4	6-12	42.7	20.7	0.7-1.3	0.1	1.6

The major dissimilarity between animal fat and vegetable oils their fatty acid content. Vegetable oils have a high content of unsaturated fatty acids, mostly C18:1 ω 9 and C18:2 ω 6, whereas animal fat has a higher proportion of saturated fatty acids.²³ Although there are lots of economical oil and fats for example waste oils and unused animal fats, their major problem is the high amount of FFA. Their conversions to biodiesel are quite difficult by transesterification reactions. For biodiesel largely the materials including triglycerides are preferred. Vegetable oil contains more triglycerides and thus preferentially has been preferred for biodiesel.³⁰ Molecular weights of triglycerides are between 800 and 900 g mol⁻¹ and for this reason, they are nearly four times larger than typical diesel (C₁₆H₃₄) fuel.³¹ Because of higher molecular weights, vegetable oils have low volatility and due to their unsaturation, they are naturally more reactive than diesel fuels. For these reasons, they are much more susceptible to oxidation and thermal polymerization reactions.³¹ Thus, the triglycerides are preferred for formation of FAME by transesterification.

A lot of vegetable oils are differentiated by their different fatty acid compositions. The types of fatty acids in triglycerides are important for biodiesel quality. In triglycerides of vegetable oil, the dominant fatty acids are C16:0, C18:1 ω 9 and C18:2 ω 6. Additionally, the fatty acids C14:0, C16:1 ω 7, C18:0, C20:0, C22:0, C24:0, C22:1 ω 9 and C18:3 ω 6 are generally present in vegetable oils and their proportions may vary from plant to plant.

2.2. Composition of animal fats as a feedstock for biodiesel

The inedible tallow, fats, edible tallow, lard, yellow and brown grease, all these raw materials are mainly

from animals such as beef, pork, chicken fat, and poultry, as these are most used on a large scale in the food industry and for biodiesel production.³² Mixtures of vegetable oils and animal fats can be used as yellow greases. It is also known to be lower-quality grades of the cow or sheep fat (tallow); however, it usually comes from vegetable oil and termed waste oil, cooking oil or used vegetable oil. The tallow is made of beef fat, the lard is pork fat and the chicken fat is from poultry. Brown grease comes from restaurant fats and sewage plants. The brown grease is gelatinized at room temperature. Yellow, brown grease and tallow can be used for biodiesel, in spite of the high costs of processing and low yield of biodiesel.³³ Each year, over 1.4 billion gallons of used cooking oil and animal fat are provided by the United States. Indeed, nearly 74% of the inedible tallow and grease are fabricated as animal feed and also the remainder is used to make lubricants, soaps, biodiesel and other products.³³ Due to their high content of saturated fatty acids, animal fats have high viscosity and are in solid form at room temperature. Incomplete combustion and poor atomization of fuel are based on the high viscosity of the fuel.²⁴ Subsequently, particulate in the exhaust gas and high emissions of pollutants increases.³⁴

Animal fats are easily existing due to good managing product control and handling procedures of meat industries. Animal fats are mostly used as animal feeds, however; this application recently decreases owing to the possible diseases. For this reason, the using of animal fats for biodiesel is a good alternative to evaluate the wastes.⁷ Another problem is that biodiesel from animal fat and cooking oil is less resistant to cold weather than biodiesel from vegetable oils. Therefore, additive products have been developed particularly for biodiesel

production.³³ The biggest problem of animal fats for biodiesel is that they contain a large quantity of FFA that is very difficult to be converted to biodiesel by alkaline transesterification because of formation of fatty acids salts (soap). Soaps can prevent the dissociation of the biodiesel from glycerine fraction and cause poor quality. In research about alkaline transesterification of beef tallow, it has been stated that FFA content needs to be kept below 0.5% (1 mg KOH g⁻¹); this means that the fats and vegetable oils must be refined to remove FFA.³⁵ FFA content influences the yield of biodiesel and causes a delay in the process of biodiesel production. Immiscibility of methanol and animal fats is another problem in biodiesel production. Stirring the solution does not thoroughly form an emulsion, resulting in low production of FAME. For this reason, the solution should contain catalysts because it helps to the conversion of triglycerides to biodiesel.

Tallow which is one of the most important animal fats has been used mostly in recent work on biodiesel. The fatty acids contents of tallow mainly comprise of C18:1 ω 9 (26-50%), C18:0 (6-40%), C16:0 (17-37%), C14:0 (1-8%), C18:2 ω 6 (0-5%) and other branched-chain acids.³⁵ It has been also reported that C18:0 (19-25%) is the most abundant fatty acid, C18:1 ω 9 is found between 37-43% in tallow.²³ On the other hand, in lard, C16:0 (23.6-30%), C18:0 (12-18%) and C18:2 ω 6 (40-50%) have been found to be predominant fatty acids (Table 1).²³ In the tallow, the fatty acids are mostly saturated and monounsaturated fatty acids and only a minimum amount of essential fatty acids can be found.³⁶ Additionally, tallow has a high cholesterol level and lacks in natural antioxidants.³⁷ In another study, it is stated that the fatty acid composition of lard basically comprises C18:1 ω 9 (41.6%), C16:0 (23.9%) and some C18:2 ω 6 (13.2%), and it contains (67.3%) of C16:0 in the sn-2 position of triglycerides.³⁸ Because of its composition, the lard can be melted easily physically. Besides, the lard contains high levels of cholesterol and does not contain natural antioxidants, so the level of oxidation must be preserved by adding natural or synthetic antioxidants³⁸ for preventing oxidation of fatty acids. It is normal to have different results regarding animal fats. Because, in the analysis of fatty acids, animal fats from different regions have been selected. It is emphasized that fatty acids which are detected at high levels in the fat are dominant in many studies. On average, the lipid composition of the animal fat is between 38-43% for saturated fatty acids, 56-62% for unsaturated fatty acids, 47-50% for monounsaturated fatty acids and 6-10% for polyunsaturated fatty acids.³⁹

The content of fatty acids in milk fats, rendered animal fats, and fish oil are determined at different levels. The short-chain fatty acids from milk are larger than other fats, varying between C4:0 to C10:0 carbon-

containing fatty acids.⁴⁰ Animal fats have more saturated fatty acids and monounsaturated fatty acids whereas fish oils consist of more polyunsaturated fatty acids.³⁵ The composition of fatty acids in animal fats is important for qualified biodiesel production. There are many reasons affecting the fatty acid ratio of animals. Genetic, feeding behavior, animal physiology, environmental and climatic factors are some of these factors, but the most important factor is nutrition. For instance, the fatty acids composition (particularly C18:2 ω 6) can be altered by increasing the grains in the animal diet, in poultry. Increases in peanut and corn in pig diet could produce softer lard.³⁸

However, when compared with biodiesel based on vegetable oil, animal fat originated biodiesel has some important advantages as follows:⁴¹ the animal biodiesel blend (B20) cetane number is higher than standard diesel fuel, and therefore, the engine runs very smoothly with animal fat-based biodiesel. It has higher calorific value and higher cetane number and low sulfur and aromatic contents. Net sulfur dioxide (SO₂) and carbon dioxide (CO₂) emissions are reduced by 100%, preventing in this way global warming, acid rain, and visible smoke and noxious odors. Without any major modification in machines, animal FAME as biodiesel blended with diesel fuel can be used in conventional diesel engines, generators, and boilers. Magnesium and nickel-based additives reduce the pour point, flash point and viscosity of biodiesel. Additionally, it is a clean liquid fuel and biodegradable in aqueous solution, 95% resolve within 28 days. A flashpoint of 150°C which compares very favorably to diesel oil whose value is 50°C. Several studies in the U.S. have shown that biodiesel reduces by 90% the risk of cancer. Positive health reduces the effects of carcinogenic aromatic polycyclic hydrocarbon (PAH), particularly following cancer-causing agents: benzofluorantren 56% reduction, benzopyrenes 71% reduction and fenantren 97% reduction. Hydrocarbons and soot emissions are reduced by 10-50% and 40-60%, respectively. The major disadvantages of animal fat originated biodiesel are that having a higher cold filter plugging point owing to the greater content of SFA and being less stable to oxidation on account of the absence of antioxidants.^{12,41}

2.3. Composition of algae lipids as a feedstock for biodiesel

In comparison to higher plants, microalgae have several advantages as higher photosynthetic efficiency, growth rate, the production rate of biochemicals and so on. In addition to the high content of lipids, microalgae biomass encompasses a significant amount of carbohydrates, proteins, and some other nutrients, therefore the residual biomass from biodiesel production processes can be used potentially as animal feed also.

Other constituents apart from lipids, e.g. pigments, proteins, carbohydrates in microalgae have commercial importance as nutraceuticals and pharmaceuticals. These constituents can be produced from microalgae in an integrated biorefinery approach along with biodiesel production.⁴² Some of the residual biomass may be used to produce methane by anaerobic digestion, for generating the necessary electrical power for running the microalgae biomass production facility. Overall, it is used as a very outstanding raw material in producing of biodiesel due to the high content of the oil. In comparison to other oil crops, microalgae have beneficial potentials in biodiesel production. When compared to land plants, First, much land is not needed for the cultivation of microalgae.⁴³ Also, biodiesel from microalgae does not compromise the production of food and other products obtained from crops. Second, microalgae grow more rapidly and algal species are rich in oils than conventional crops.⁴⁴ Oil from microalgae does not burn entirely and form deposits in the fuel injector of diesel engines due to low volatility and high viscosity (about 10-20 times higher than diesel fuel). However, the transesterification of microalgae oils will greatly reduce the original viscosity and increase the fluidity.

Unlike other oil crops, microalgae grow pretty quickly and most of them are fairly rich in oil. They can multiply twice their biomass within 24 h. In some microalgae, lipid quantity can exceed 80% by weight of dry biomass.^{45,46} The proportion of algae lipid generally ranges from 20 to 80% varying from species to species. Medium composition, temperature, illumination intensity, the ratio of light/dark cycle and aeration rate can affect the composition and fatty acid profile of lipids extracted from particular algal species.⁴⁷ Some certain microalgae can accumulate the substantial amounts of lipids up to 50% of dry cell weight,⁴³ which is 40 times more oil per acre than other plants used for biodiesel.⁴⁸ There are numerous microalgae species including high lipid on the basis of dry weight, for instance *Dunaliellatertiolecta* (37-40%), *Chlorella protothecoides* (38-51%), *Chlorella ellipsoidea* (84%), *Botryococcusbraunii* (68%-74%), *Nitzschia* (49-51%), *Nannochloropsis sp.* (39-42%), *Schizochytriumsp* (50-77%) and *Neochlorisoleoabundans* (35-54%) (Table 2).^{43,49} Microalgae producing lipid with higher triglycerides more opt for the biodiesel production⁴³ because triglycerides are the main lipid class for biodiesel. The synthesis of triglycerides in microalgae may provide of the formation of acetyl coenzyme A in the cytoplasm, the denaturation, and elongation of the carbon chain of fatty acids and the biosynthesis of triglycerides.²⁹ Above all, the development of new algal species by genetic recombination should be considered that for higher triglyceride synthesis, fast reproduction ability, and more lipid accumulation capacity.

In place of microalgae, lipid-producing heterotrophic microorganisms grown on natural resources of organic carbon such as sugar is considered to be used for biodiesel production; yet, heterotrophic production of lipid is not as effective as photosynthetic microalgae production.^{50,51} For why, the prolongable organic carbon sources for heterotrophic microorganisms are constructed by crop plant photosynthesis. The production of algae lipids is related to the fact that high amounts of lipid-rich microalgae biomass can be produced inexpensively compared to the other organisms.⁴³ Commonly, both organic carbon sources such as glucose, acetate, etc. and inorganic carbon (CO₂) can be used by microalgae for the production of lipids.²⁹

Microalgae usually contain long-chain fatty acids like C20 and C22, and the ratio and type of fatty acids vary from species to species. Generally, short-chain fatty acids like C14 and C18 carbon-containing which are the main constituents of biodiesel are predominant fatty acids in *Chlorella sp.*; however, hydrocarbons and high amount of long-chain fatty acids can be seen in some particular microalgae species. Therefore, it is essential to distinguish convenient microalgae species as raw materials for biodiesel production. Microalgal lipids are contrary to most vegetable oils in being pretty rich in PUFA with four or more double bonds.⁵² For instance, docosahexaenoic acid (DHA, C22:6 ω 3) and eicosapentaenoic acid (EPA, C20:5 ω 3) can be found in algal oils. Fatty acids and FAME with four and more double bonds are vulnerable to oxidation during storage and for this reason, their suitability for biodiesel becomes decreasing. Some vegetable oils such as canola oil containing large proportions of C18:2 ω 6 and C18:3 ω 3 have also this problem. Even though these fatty acids have much higher oxidative steadiness compared with C22:6 ω 3 and C20:5 ω 3, the European Standard Institute limits C18:2 ω 6 and C18:3 ω 3 methyl esters content in biodiesel for the vehicle to 12% (mol).⁴³ The fatty acid content of some important algae has been emphasized in many studies. For instance, *Nannochloropsis sp.* contains 28.83% C16:0, 32.93% C16:1 ω 7 and 21.16% C18:1 ω 9; *Chlamydomonas reinhardtii* contains 23.77% C16:0, 25.49% C18:3 ω 3; *Scenedesmus sp.* contains 18.42% C16:0 and 49.64% C18:1 ω 9 (Table 3). The high content of saturated and monounsaturated fatty acids in these algae indicates that they may be a good raw material for biodiesel.

One of the essential macro nutrients in the production of lipids is nitrogen. Complex nitrogen source can be better to simple nitrogen source in the heterotrophic culture of microalgae due to providing vitamins, amino acids, and essential growth factors. For the cultivation of microalgae, industrial nitrogen-rich wastewater can also be evaluated. Diluted monosodium glutamate waste is well treated as an inexpensive fermentation medium for *Rhodotorulaglutinis* to synthesize lipids.⁴⁴

Table 2. Total lipid concentration of some popular microalgae based on % dry weight^{43,49}

Algal species	Total lipid content (% dry weight)
<i>Anabaena cylindrica</i>	4-7
<i>Aphanizomenonflos-aquae</i>	3
<i>Arthrospira maxima</i>	6-7
<i>Botryococcusbraunii</i>	68-74
<i>Chlamydomonasrheinhardii</i>	21
<i>Chlorella pyrenoidosa</i>	2
<i>Chlorella ellipsoidea</i>	84
<i>Chlorella vulgaris</i>	14-22
<i>Dunaliellabioculata</i>	8
<i>Dunaliellasalina</i>	6
<i>Euglena gracilis</i>	14-20
<i>Porphyridiumcruentum</i>	9-14
<i>Prymnesiumparvum</i>	22-38
<i>Scenedesmusdimorphus</i>	16-40
<i>Scenedesmusobliquus</i>	12-14
<i>Scenedesmusquadricauda</i>	21
<i>Spirogyra sp.</i>	11-21
<i>Spirulina maxima</i>	6-7
<i>Spirulinaplatensis</i>	4-9
<i>Synechococcus sp.</i>	11
<i>Tetraselmismaculata</i>	3
<i>Chlorella sp.</i>	28-32
<i>Chlorella protothecoides</i>	38-51
<i>Cryptocodiniumcohnii</i>	20
<i>Cylindrotheca sp.</i>	16-37
<i>Dunaliellaprimolecta</i>	23
<i>Dunaliellatertiolecta</i>	37-40
<i>Isochrysis sp.</i>	25-33
<i>Monallanthussalina</i>	>20
<i>Nannochloris sp.</i>	20-35
<i>Nannochloropsis sp.</i>	39-42
<i>Neochlorisoleoabundans</i>	35-54
<i>Nitzschia sp.</i>	49-51
<i>Phaeodactylumtricornutum</i>	20-30
<i>Schizochytrium sp.</i>	50-77
<i>Tetraselmussueica</i>	15-23

Many microalgae have increased the lipid content even further by nitrogen restriction. In a study, it has been stated that *Porphyridiumcruentum* can duplicate its total lipid content especially neutral lipids, under nitrogen

starvation.⁵³ Also, a study of microalgae has showed that *Chlorella pyrenoidosa* can be induced to accumulate 70% of its dry weight as lipids by nitrogen starvation.⁵⁴ Nonetheless, nitrogen starvation cannot always finish in a boost in total lipid content in microalgae but can alter their lipid composition. Zhila and co-workers⁵⁵ reported that the algae *Botryococcusbraunii* deposited high content (28.4-38.4%) of C18:1 ω 9 under nitrogen limitation, however, the scope of total lipids and triglycerides did not change.

2.4. Composition of rendered oils and fats as a feedstock for biodiesel

The annual percentage of recycled vegetable oil obtained from potato processing plants, cookie factories, fast-food restaurants, industrial deep fryers is often more than expected. If all of this can be recycled, it can be protected partly the petroleum fuel in place. Waste cooking oil is mostly obtained from large quantities of oil used for fried food, since it needs full immersion of the food at temperatures above 180°C. The high temperature causes the changes in the chemical and physical composition of the oil and food, and in its organoleptic features which affect both the oil and food quality.⁶² Physically and chemically altered oils and fats directly affect the productivity and quality of the biodiesel. Increasing FFA and unsaturated fatty acid chains are undesirable molecules in oils and fats during biodiesel production.

Recently, the rendered animal fats have got attention as raw material for biodiesel industry, because they are easily obtainable may be found in excess quantity with relatively low-priced in regions with excessive livestock. Most of the waste cooking oil collected from eating houses and food-service places contain animal fats. Biodiesel produced from animal-originated fats by a transesterification includes substantial quantities of long-chain saturated FAME, resulting in low temperature properties. Another hardship is that the waste of animal-derived fats comprises larger quantities of FFA than waste vegetable oil, and the FFA forms soap in the reactions with the alkaline catalyst reducing biodiesel efficiency.⁶³ The soaps can stop to the separation of the biodiesel from the glycerine fraction. An alternative arrangement is to use acid catalysts, which can esterify FFA.⁶⁴ Black and yellow greases are present among the important industrial waste fats. Black greases are elucidated loosely as greases arising from sewage or other unusual oil sources. It has a low conversion factor to biodiesel on account of its high FFA content. Brown greases are largely described as a composition of greases and obtained from the slaughter industry. Yellow greases consist of the oils and greases coming from the fast-food industry.³³ Many investigations have been carried through the fatty acid composition of rendered fats and oils. It is not possible to give clear information about the fatty acid content of rendered oils. Because the fatty acid

Table 3. Lipid composition and fatty acid profile of some strains of microalgae (1 and 4⁵⁶, 2 and 3⁵⁷, 5⁵⁸, 6⁵⁹, 7⁶⁰, 8⁶¹) (based on % wet weight)

Microalgae	C16:0	C16:1 ω 7	C18:0	C18:1 ω 9	C18:2 ω 6	C18:3 ω 3	SFA	MUFA	PUFA
1. <i>Chlorella vulgaris</i>	14.55	1.18	10.51	23.62	13.8	32.1	25.06	24.8	45.9
2. <i>Scenedesmus</i> sp.	18.42	2.31	3.43	49.64	11.30	8.26	21.85	51.95	22.82
3. <i>Nannochloropsis</i> sp.	28.83	32.93	0.98	21.16	2.24	-	35.18	54.09	8.57
4. <i>Chlamydomonas reinhardtii</i>	23.77	1.94	4.41	19.73	6.58	25.49	18.18	22.88	32.07
5. <i>Chlorococcum</i> sp.	19	4	3	63	4	-	-	-	-
6. <i>Monoraphidium</i> sp.	22.6	-	1.2	-	4.2	42.2	23.8	-	68
7. <i>Neochloris oleoabundans</i>	23-30	0.6-3.5	0.9-11	30-43	18-23	5-12	-	-	-
8. <i>Selenastrum capricornutum</i>	45.62	5.96	-	4.27	11.75	-	48	10	17

compositions of the rendered oils mostly depend on raw material types.

Rendered waste oil contains decomposition products which degrade the quality of the oil and leads to a loss of efficiency in the transesterification reaction. Accordingly, this can cause unwanted by-products, damaging the final output. Therefore, it is significant to refine rendered waste oil for biodiesel production. Such purification has an effect of 67% to 87% in reaction yield after bleaching. The processes that can be applied to assess the adequacy of waste oils are de-acidification, filtration, neutralization, and bleaching. The processes of de odorization and degumming are not required since the oils have been treated previously before use. Although odors appear during degradation, its removal is not requisite for the biodiesel production.⁶²

The rendered oils and fats must have a low acid amount, to prepare high yielding esters to use alkaline catalysis. The acid amount is an indication of the number of acidic functional groups in a sample and is evaluated in terms of the quantity of potassium hydroxide which is needed to neutralize the sample. In the alkali-catalyzed transesterification reaction, the FFA is converted into the ester by reaction with the catalyst to form soap. In acid-catalyzed processes, the reaction of FFA with alcohol forms ester, and water is produced which restricts the transesterification of triglycerides.⁶⁴ The association between free FFA level and triglycerides transesterification in the course of acid-catalyzed biodiesel is investigated in a study. The sample compounds were made ready by adding C16:0 to soybean oil to acquire FFA level of 5-33%. The transformation rate of soybean oil to methyl ester decreased from 90.54% to 58.77% as the FFA level rose from 5% to 33%.⁶⁵

2.5. Composition of yeast and bacteria lipids as a feedstock for biodiesel

In recent years, very important and comprehensive researches have been done on biodiesel production capacities of microorganisms. Most of the microorganisms, particularly yeast and bacteria, are seen as a hopeful source for obtaining high-value lipids and supply considerable advantages over conventionally used vegetable or animal-based oils and fats. The yeasts can produce lipids in a very short time with a low cost. Additionally, bacteria have a less complicated genome and metabolism and can produce a wider variety of lipids than multicellular eukaryotes. On the other hand, they can generally be genetically altered more readily to obtain optimized strains that increase further the prolificacy of the entire process.^{66,67} The production of "third-generation biofuels" purposes to create efficient processes for the production of the lipids obtained from organic wastes of microorganisms. In some studies, it is expressed that special anaerobic microorganisms accumulate lipid of triglycerides during wastewater treatment.⁶⁸ Oleaginous photosynthetic microorganisms efficiently convert carbon dioxide to lipids via photosynthesis. It is known that microalgae store triglycerides under nutritional and environmental stress, some cyanobacteria accumulate lipid in the form of diglycerides in significant quantities on their thylakoid membranes and may even be genetically engineered to provide overproduction of FFA.⁶⁹

In a paper on yeast, with some applications, yeast could accumulate lipids up to 37% of its dry weight, which is normally around 5%. It has been found that biodiesel produced by yeast has a very similar structure

compared to biodiesel generated with animal or plant-based raw materials in which C16 and C18 fatty acid chains are predominant. Furthermore, the study stated that FAME obtained from yeast grown under normal condition showed only four distinguished peaks of C16:0, C16:1 ω 7, C18:0 and C18:1 ω 9; whereas, the product of yeast cultivated in metabolic stress circumstances has given peaks of C16:0, C16:1 ω 7, C18:0, C18:1 ω 9, C18:2 ω 6, C20:0 and C22:0 of FAME along with several other peaks of structural lipids. In the experiment, the cells were forced to accumulate lipids by stress condition, so the concentration of the fatty acids had increased up to detectable quantities.⁷⁰ With stress-based experiments and genetic modifications applied to the yeast, these microorganisms could allow them to accumulate higher lipid concentration. So that biodiesel can be obtained more cheaply and easily in the future.

Like yeast, bacteria also accumulate high amount of lipid in their bodies. For instance, the bacteria such as *Arthrobacter*, *Dietzia*, *Gordonia*, *Nocardia*, *Rhodococcus*, and *Streptomyces* have the ability of accumulation of triglycerides in significant amounts as intracellular storage deposits. However, *Rhodococcus opacus* commonly known with impressive triglycerides content of up to about 80%. At the same time, it is seen as a very encouraging strain for industrial lipid production by rapid growth, the acceptance of high substrate tolerance and a large carbon source.⁷¹ Though *Arthrobacter* was announced several years ago to gather similar high quantity, this strain has not been employed in further studies. *Gordonia* or *Rhodococcus* strains expressly seem suitable for the conversion of industrial waste materials for example wastes from agro-industrial processes, molasses, dairy wastewater, etc. or lignocellulose hydrolysates, whilst a *Streptomyces* can make use of cellobiose to build up to 50% fatty acids. Unlike triglyceride synthesized by *Rhodococcus*, which are primarily composed of straight-chain of C16 and C18 fatty acid molecules, *Streptomyces* obtain the special capability to synthesize branched-chain fatty acids.^{72,73}

As an alternative, ethanol can be used to get biodiesel from fatty acid ethyl esters (FAEE), which can exhibit superior physicochemical properties as per FAME, while a large majority of biodiesel is now produced with methanol derived from fossil sources to produce FAME.⁷⁴ In a study, some initiatives were undertaken to entirely synthesize FAEE de novo from irrelevant carbon sources in *Escherichia coli*. In a study, the overexpression of a WS/DGAT gene was normally joined with the ethanol synthesis pathway from *Zymomonas mobilis*.⁷⁵ Up to now, the highest FAEE amounts of 1.5 g l⁻¹ have been obtained only in glucose and small-scale cultivations. The major handicap of *Escherichia coli* is that it could not metabolize lignocellulose, but the first evidence of passage could be obtained by establishing an

optimized strain using switchgrass hydrolysis.⁷⁶

Another important property of bacteria is that they can synthesize branched fatty acids. Biodiesel produced from branched fatty acids has advantages over biodiesel produced from other feedstock. In a study, it is stated that the synthesis of fatty acid alkyl esters from branched short-chain alcohols and branched fatty acids (e.g. isoamyl alcohol or isobutanol); making use of the biosynthesis pathway for branched-chain amino acid synthesis is getting importance recently. There are advantages of biodiesel produced mainly from branched fatty acids found in microorganisms. For instances, branched fatty acid esters exhibit improved quality at low temperatures, where conventional biodiesel generally has relatively low efficiency. On the other hand, the synthesis of branched FAEE is still not achieved in significant quantities. Alternatively, bacteria incorporating inherently branched fatty acids into triglycerides such as *Streptomyces* may be favorable for biodiesel production with a mixture of branched and straight-chain fatty acid remnants.⁷⁷

3. COMMON TRANSESTERIFICATION REACTIONS FOR BIODIESEL

Vegetable oils or animal fats are not preferred to be used directly as fuel. They have high viscosity, and it is necessary to keep down their viscosity to use them in a common diesel engine. There are generally four methods used to reduce the viscosity; blending with petrodiesel, pyrolysis, micro-emulsification, and transesterification. The products produced by the transesterification reaction are generally known as biodiesel.⁷⁸ Biodiesel is usually obtained by transesterification of fats and oils from lipid-containing raw materials such as soya, safflower, corn, palm, rapeseed, sunflower, jatropha, pongamia, cottonseed, tallow, lard, yellow and brown grease, cooking and waste oils. Clearly speaking, transesterification is done by monoglycerides, diglycerides and triglycerides from the almost all types of lipids of raw materials and can be affected by various factors including raw material composition, catalyst type, catalyst ratio, content of FFA, water concentration, the ratio of alcohol to triglycerides, alcohol type, pressure, temperature, mixing time, etc. Many studies have evaluated the variables that affect fatty acid alkyl esters known as biodiesel yields and their interactions.⁷⁹⁻⁸¹

The transesterification is the reaction of fats or oils (mostly 15 and 23 carbon atoms containing glycerides) with alcohol of low molecular weight (CH₃OH or C₂H₅OH) by using an alkaline, acidic or enzymatic catalyst, to produce fatty acid alkyl esters and glycerine. Triglycerides are converted to diglycerides followed by monoglycerides and at last glycerol. One molecule of a fatty acid alkyl ester is produced at each step.

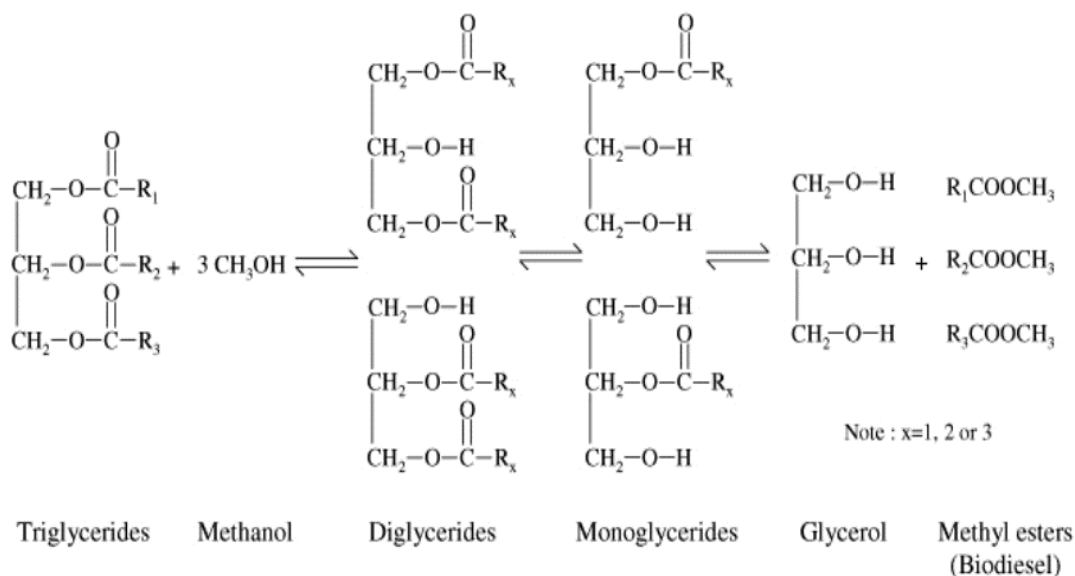


Figure 1. Transesterification of triglycerides to biodiesel.³¹

The transesterification process consists of three continuous steps: firstly, the conversion of triglycerides to diglycerides, secondly the conversion of diglycerides to monoglycerides and then lastly, the transformation of monoglycerides to fatty acid alkyl ester and glycerine.²⁷ One fatty acid alkyl ester molecule is produced from each conversion of fats and oils by alcohol as shown in Figure 1.³¹ When methanol alcohol opts-in transesterification reaction, the process is called methanolysis and the product is known as FAME; however, when ethanol alcohol is used, the process is called ethanolsis and the product is known as FAEE. Methanolysis is the most common process for producing biodiesel.

Generally, acid, alkaline and enzymatic catalysts are used to increase the rate of transesterification reaction.²⁷ Using the right catalyst may affect the rate of reaction, purification process and quality of biodiesel.⁸² FFA can react with the alkaline catalyst to form water and soap, which leads to the loss of the alkaline catalysts during the reaction. For this reason, additional catalysts should be added to compensate for the catalyst loss to soap. If the FFA level is over 5%, the produced soap will prevent disconnection of the methyl esters and glycerol from each other, resulting in emulsion formation during the water washing. Thereby, it is essential to convert FFA to methyl esters firstly to decrease their contents, and then transesterification is carried out with an alkaline catalyst to convert the pretreated triglycerides with low FFA to methyl esters. On the contrary, the enzymes used in transesterification are well tolerated at FFA proportion of the raw material, but the enzymes increase the cost and may not ensure the required degree of reaction.²⁹

3.1. Alkali catalyzed transesterification

Alkali-catalyzed transesterification of triglycerides is nearly 4000 times faster than the acid-catalyzed reaction. Alkali-catalyzed transesterification requires a lower amount of catalyst to accomplish the reaction. Sodium hydroxide (NaOH) and potassium hydroxide (KOH) are regularly used as commercial catalysts at a percentage of about 1% by weight of oil or fat. Alkoxides like sodium methoxide (NaOCH₃) are even better catalysts. Use of lipase provides important benefits, however are not currently practicable on account of the relatively high price of the enzyme catalyst.⁸³ On the other hand, alkaline catalysts sometimes have drawbacks. Especially, they are very sensitive to the lipid raw materials and need a pretreatment to enhance the transesterification purity, mainly by operating in batch mode by needing large reaction times to obtain a complete transformation of oil, and also has complex biodiesel purification stages after the reaction.^{84,85} Alkaline catalysts produce soap from FFA in oils and fats. For this reason, if the lipid contains a high amount of FFA, it is not suitable for biodiesel production by an alkaline catalyst.⁸⁶ With the high amount of alkaline catalyst, alkaline will react with the fatty acids and form emulsions between water and soap molecules. More soap will be produced which consume the catalyst and reduces the catalytic efficiency as the catalyst concentration increases. When the high concentration of KOH is used as catalyzer, crude biodiesel will be purified by washing with sodium chloride (NaCl) solution.⁸⁶ Saponification will also bring other problems such as the formation of gels, increases in viscosity and difficulty in achieving

separation of glycerine. Elimination of these saponified catalysts is technically arduous and it requires extra expenditure.⁸⁷ Alkaline catalyst transesterification is used extensively throughout the world for vegetable, algal and used oils with low FFA content despite all these drawbacks.

Homogeneous alkaline catalysis is mostly used for biodiesel production because it reacts at low temperature and high conversion output can succeed in a short period.⁸⁶ The basic reason for this is that it is kinetically much faster than heterogeneously catalyzed transesterification and is economically effective. Ethanol, methanol, or butanol is preferred in the reactions to obtain methyl, ethyl, or butyl esters, respectively. Generally, the ratio of alcohol and oil is 6:1, at a reaction temperature of about 60°C if methanol is used, or 70°C if ethanol is used. The amount of catalyst used in the mixture is in the range of 0.5-1.0% (w/w).^{84,85}

3.2. Acid-catalyzed transesterification

Direct use of animal fats and vegetable oil is generally considered to be objectionable because of low volatility and high kinematic viscosity and leads to operational problems in a diesel engine, for instance, the formation of deposits and injector coking due to poorer atomization in the combustion chamber.⁸⁸ Different methods have been devised to achieve sufficient engine compatibility for high-quality diesel fuels produced from vegetable oils and animal fats, including derivatization (transesterification, hydrotreating, and ozonation), dilution, blending, pyrolysis, gasification, and micro-emulsification. Transesterification process takes away glycerol from the triglycerides and alters it with alcohol mostly methanol. The process reduces the viscosity, however preserves heating value and the cetane number.⁸⁹ Transesterification reaction reduces the viscosity of the lipid to a range (usually 4-5 mm²s⁻¹) adjacent to that of petrodiesel.⁸⁸

In the existence of water and FFA, saponification reactions occur during alkaline catalysts because FFA reacts with the alkaline catalyst to produce soap, thus reduce FAME yield and even inhibit the transesterification reaction. Therefore, it is more convenient to use an acid catalyst for transesterification of triglycerides and esterification of FFA. Strong acid catalysts are less susceptible to FFA and can perform in transesterification and esterification reactions simultaneously. Despite all these advantages, alkaline-catalyzed reactions are still preferred today, because acid-catalyzed reactions are much slower than alkaline catalyzed reactions. During the acid-catalyzed reactions, the FFA can react with alcohol to form biodiesel and more suitable for converting FFA with high biodiesel yield.⁷ High acidic animal fat (more than 2.5% w/w of FFA) requires pretreatment to minimize their FFA content. This is normally fulfilled by acid-catalyzed

esterification, using methanol as a reagent and H₂SO₄ as catalyst.⁶⁴

The acid-catalyzed transesterification reaction is usually done by HCl, BF₃, H₃PO₄, H₂SO₄, and R-SO₂OH. Especially R-SO₂OH and H₂SO₄ are mostly utilized acids. These acid catalysts give very high efficiency in alkyl esters as biodiesel; however, the reaction is quite slow, needing temperatures above 100°C and from 3-48 h to catch up complete conversion.⁹⁰ Besides the type of catalyst used, the type of alcohol used also affects the rate and efficiency of the reaction. In a study, it was stated that soybean oil methanolysis in the existence of 1 mol % of H₂SO₄, with an alcohol/oil molar ratio of 30:1 at 65°C, prolongs 50h to completed reactions (>99%); whereas, the butanolysis (at 117°C) took 3 h and ethanolysis (at 78°C) took 18 h with the equal quantities of catalyst and alcohol.⁹¹ In fact, a way of accelerating these slow-acid catalyzed reactions has been emphasized in some studies. By the use of an extensive amount of acid catalyst, transesterification reaction rates may be increased. In most of the papers, acidic catalyst percentage (H₂SO₄) in the reaction mixture varies from 1 to 5 wt %.⁹¹ However, the use of acid in such a high concentration is not preferred because it will ascend the cost of biodiesel production protein.

3.3. Enzyme catalyzed transesterification

In enzyme-catalyzed transesterification reactions, the lipase enzyme and alcohol are used to convert lipids to alkyl esters. Lipase enzymes are mostly obtained from bacteria and fungi because of their high enzyme yield and reproducibility in dense quantities. The microorganisms used to obtain the lipase enzyme are mostly: *Burkholderia cepacia*, *Candida antarctica* (Novozyme 435), *Aspergillus niger*, *Bacillus thermoleovorans*, *Fusarium heterosporum*, *F. oxysporum*, *C. cylindracea*, *C. rugosa*, *Chromobacterium viscosum*, *Geotrichum candidum*, *Thermomyces lanuginose*, *Mucormiehei*, *Humicola lanuginose*, *Pseudomonas cepacia*, *P. roqueforti*, *P. aeruginosa*, *P. putida*, *R. arrhizus*, *P. fluorescens*, *Rhizomucormiehei*, *Oosporalactis*, *Rhodotorula rubra*, *Saccharomyces cerevisiae* and *Staphylococcus hyicus*, *Penicillium cyclopium*, *Rhizopus oryzae*, *R. japonicus* (NR400), *R. stolonifer* (NRRL1478), *R. chinensis*, *R. delemr*, *R. fusiformis*, *R. circinans*.^{92,93} Among these microorganisms, *C. antarctica*, *C. rugosa*, *R. miehei*, *R. chinensis*, *P. cepacia*, *P. fluorescens*, *R. oryzae* and *T. lanuginosa* have produced the most effective lipase enzymes.⁹⁴ Lipases can be classified based on their extracellular and intracellular applications. Extracellular lipases are extracted and purified from organisms; while intracellular lipases are enzymes that are present within the organisms.⁹⁵

The conventional synthesizing method of biodiesel, which includes acid and alkaline catalyst, is accomplished at a high temperature closer to methanol or ethanol boiling point; therefore some unwanted by-products such as soap are created.⁷ To put away these drawbacks, it has been proposed that the enzymes can be used instead of chemical catalysts owing to their mild operative circumstances and high particularity. Besides, there is no need for feedstock purification because biocatalysts like lipase can esterify feedstock FFA along with the transesterification of triglycerides.³² Some studies have indicated essential data about the temperature tolerances of the enzymes from microorganisms. *C. antarctica* was fulfilled in a temperature between 25 and 55°C by methanolysis. The optimum temperature was detected at 40°C, the temperature above 40°C leads to a diminution in conversion.⁹⁶ *P. cepacia* was performed in a temperature extended from 20 to 70°C and found the optimal temperature to be 50°C after 1 h which decreased to 40°C after 2 h by butanolysis.⁷⁸ Methanolysis with *R. chinensis* enzymes had an optimal temperature of 30°C.⁹⁷

There are many advantages of using enzymes instead of acid and alkaline catalysts including absence of soap formation, producing a higher quality glycerol, ability to process large variation in raw material, having ability to esterify both FFA and triglycerides in one stage without the need for a washing step, works under milder conditions leading to less energy consumption, and high FFA consisting animal fat and waste oil can be catalyzed with completely to alkyl esters.^{93,98} On the other hand, enzymatic transesterification has many disadvantages, such as longer response time, requiring a higher catalyst amount to complete the reaction and high fabrication cost. Additionally, lipase becomes ineffective in 100 days of application, although it can be used repeatedly after immobilization of the lipase on the carrier.^{93,96}

4. CONCLUSIONS

To overcome the energy crisis in the world, the search for biologically lipid-rich materials for using in biodiesel productions effectively has attracted much interest. New modified microbial, animal, algal and vegetable raw materials are considered positively for biodiesel production in terms of short development cycles, high lipid content, and ease of replacement via biotechnological methods. Raw materials commercially exploited by countries constitute mostly edible lipids commonly supplied from soybean, rapeseed, coconut, corn, palm, sunflower, safflower, etc. It is thought that the use of such edible oil to produce biodiesel in the world is not correct because such oils have a big gap in supply and demand around the world. Increasing pressure to increase edible oil production also limits the biodiesel

production. For this reason, many of today's examinations are related to algae and microbial lipids which are of great promise for biodiesel.

Generally, short-chain fatty acids like C14 and C18 carbon-containing raw materials are more suitable for biodiesel productions. Saturated fatty acids have got more advantages than unsaturated fatty acids because FAME with four and more double bonds is susceptible to oxidation during storage, and for this property, their acceptability for use in biodiesel becomes decreasing. Less FFA content in the oils or fats is more advantageous because it prevents the formation of soap. The importance of lipid content in a high proportion of acylglycerol provides a greater advantage, even if the raw material has high oil content.

Biodiesel has several important advantages. Most of which can be listed as follows: the emission profile of the biodiesel is much better than petroleum diesel, reducing emissions of unburned hydrocarbons, sulfates, carbon monoxide, nitrated polycyclic aromatic hydrocarbons, and particulate matter. It is non-toxic renewable and biodegradable fuel, besides it can be used as blended or pure with petrodiesel in engines without any modifications. Transportation and storage of the biodiesel are less dangerous than the petroleum diesel because the flash point temperature of biodiesel is nearly 170°C, whereas it is 60 to 80°C for petroleum diesel. The combustion process is better than petrodiesel and smoke is lesser. It can diminish unburned hydrocarbons emissions by 90%. Higher lubrication capacity prolongs engine life. The biodiesel embodies at least 11% oxygen and it causes better burning than petroleum diesel. On the other hand, it reduces the release of PAH (Polycyclic aromatic hydrocarbons) (cancer-causing compound). The CO₂ released from biodiesel combustion is an approximate amount for photosynthesis of plants. In other words, the vegetable oil carbon percentage is nearly 77.8%, the average percentage of animal fats is 76.1%, whereas carbon percentage of fossil diesel is 86.7%.

To sum up, biodiesel production recently has attracted much attention due to its many advantages over traditional energy sources. At present, the high cost of oily raw materials is the main problem preventing commercial biodiesel production. For this reason, to develop new transesterification technologies and to obtain cheap raw materials that are rich in fat or oil content seem like the most important solution for an efficient biodiesel production.

ACKNOWLEDGEMENTS

I am thankful to Osman Baysal for his texting and technical supports.

Conflict of interests

Author declares that there is no a conflict of interest with any person, institute, company, etc.

REFERENCES

- Fazal, M. A.; Haseeb, A. S. M. A.; Masjuki, H. H. *Renew. Sustain. Energy Rev.* **2011**, 15(2), 1314-1324.
- Refaat, A. A. *Int. J. Environ. Sci. Technol.* **2009**, 6, 677-694.
- Lam, M. K.; Lee, K. T.; Mohamed, A. R. *Biotechnol. Adv.* **2010**, 28(4), 500-518.
- Lapuerta, M.; Armas, O.; Rodríguez-Fernández, J. *Prog. Energy Combust. Sci.* **2008**, 34, 198-223.
- Balat, M.; Balat, H. *Appl. Energy* **2010**, 87(6), 1815-1835.
- Moser, B. R. *Energy Fuels* **2008**, 22, 4301-4306.
- Encinar, J.M.; Sánchez, N.; Martínez, G.; García, L. *Bioresour. Technol.* **2011**, 102(23), 10907-10914.
- Atabani, A. E.; Silitonga, A. S.; Badruddin, I. A.; Mahlia, T. M. I.; Masjuki, H. H.; Mekhilef, S. *Renew. Sustain. Energy Rev.* **2012**, 16, 2070-2093.
- Gui, M. M.; Lee, K. T.; Bhatia, S. *Energy* **2008**, 33, 1646-1653.
- Sharma, Y. C.; Singh, B.; Upadhyay, S. N. *Fuel* **2008**, 87, 2355-2373.
- Tan, T.; Lu, J.; Nie, K.; Deng, L.; Wang, F. *Biotechnol. Adv.* **2010**, 28, 628-634.
- Dias, J. M.; Alvim-Ferraz, M. C. M.; Almeida, M. F.; Diaz, J. D. M.; Polo, M. S.; Utrilla, J. R. *Fuel* **2012**, 94, 418-425.
- Meng, X.; Chen, G.; Wang, Y. *Fuel Proces. Technol.* **2008**, 89, 851-857.
- Tong, D.; Hu, C.; Jiang, K.; Li, Y. *J. Am. Oil Chem. Soc.* **2011**, 88, 415-423.
- Lebedevas, S.; Vaicekauskas, A.; Lebedeva, G.; Makareviciene, V.; Janulis, P.; Kazancev, K. *Energy Fuels* **2006**, 20, 2274-2280.
- Sendzikiene, E.; Makareviciene, V.; Janulis, P. *Pol. J. Environ. Stud.* **2005**, 14, 335-339.
- Hemmat, Y.; Ghobadian, B.; Loghavi, M.; Kamgar, S.; Fayyazi, E. *Int. Res. J. Appl. Bas. Sci.* **2013**, 5(1), 84-91.
- Refaat, A. A. *Int. J. Environ. Sci. Technol.* **2010**, 7(1), 183-213.
- Pimentel, D.; Marklein, A.; Toth, M. A.; Karpoff, M. N.; Paul, G. S.; McCormack, R.; Kyriazis, J.; Krueger, T. *Hum. Ecol.* **2009**, 37, 1-12.
- Ahmia, A. C.; Danane, F.; Bessah, R.; Boumesbah, I. *Rev. Energ. Renouv.* **2014**, 17 (2), 335-343.
- Barnwal, B. K.; Sharma, M. P. *Renew. Sustain. Energy Rev.* **2005**, 9, 363-378.
- Lin, L.; Allemekinders, H.; Dansby, A.; Campbell, L.; Durance-Tod, S.; Berger, A.; Jones, P. J. *Nutr. Rev.* **2013**, 71(6), 370-385.
- Rostagno, H. S.; Albino, L. F. T.; Donzele, J. L.; Gomes, P. C.; Oliveira, R. F.; Lopes, D. C.; Ferreira, A. S.; Barreto, S. L. T.; Euclides, R. F. Food Composition and Nutritional Requirements. In: *Brazilian tables for poultry and swine*: Viçosa Federal University, Viçosa, MG, Brazil, 2011. pp. 252.
- Dhiraj, S. D.; Mangesh, M. D. *Int. J. Emerg. Technol. Adv. Eng.* **2012**, 2(10), 179-185.
- List, G. R.; Emken, E. A.; Kwolek, W. F.; Simpson, T. D.; Dutton, H. J. *J. Am. Oil Chem. Soc.* **1977**, 54, 408-413.
- Tan, B. K.; Oh, F. C. H. *PORIM Technol.* **1981**, 4, 1-6.
- Leung, D. Y. C.; Wu, X.; Leung, M. K. H. *Appl. Energy* **2010**, 87(4), 1083-1095.
- Azam, M. M.; Waris, A.; Nahar, N. *Biomass Bioenerg.* **2005**, 29(4), 293-302.
- Huang, G.; Chen, F.; Wei, D.; Zhang, X.; Chen, G. *App. Energy* **2010**, 87, 38-46.
- Demirbas A. *Energy Conver. Manag.* **2002**, 43, 2349-2356.
- Shereena, K. M.; Thangaraj, T. *Electron. J. Biol.* **2009**, 5(3), 67-74.
- Al-Zuhair, S.; Hussein, A.; Al-Marzouqi, A. H.; Hashim, I. *Biochem. Eng. J.* **2012**, 60, 106-110.

DOI: <http://dx.doi.org/10.32571/ijct.623165>

E-ISSN:2602-277X

33. Tickell, J. Biodiesel America: How to achieve energy security, Free America from Middle-east oil dependence and make money growing fuel. Yorkshire Press, USA, 2006.
34. Kerihuel, A.; Kumar, M. S.; Bellettre, J.; Tazerout, M. *Fuel* **2006**, 85(17-18), 2371-2684.
35. Ma, F.; Clements, L. D.; Hanna, M. A. *Trans. Am. Soc. Agric. Eng.* **1998**, 41, 1261-1264.
36. Canakci, M.; Monyem, A.; Gerpen, J. V. *Trans. ASAE*. **1999**, 42, 1565-1572.
37. Nelson, L. A.; Foglia, T. A.; Marmer, W. N. *J. Am. Oil Chem. Soc.* **1996**, 73, 1991-1994.
38. Yang, T.; Xu, X.; He, C.; Li, L. *Food Chem.* **2003**, 80, 473-481.
39. Pacheco, J. W. Guia técnico ambiental de frigoríficos - industrialização de carnes (Bovina e suína). São Paulo, Brazil, CETESB (Série P + L), 2008.
40. Balcao, V. M.; Malcata, F. X. *Biotechnol. Adv.* **1998**, 16, 309-341.
41. Dias, J. M.; Alvim-Ferraz, M. C. M.; Almeida, M. F. *Energy Fuel* **2008**, 22, 3889-3893.
42. Mutanda, T.; Ramesh, D.; Karthikeyan, S.; Kumari, S.; Anandraj, A.; Bux, F. *Biores. Technol.* **2011**, 102, 57-70.
43. Chisti, Y. *Biotechnol. Adv.* **2007**, 25(3), 294-306.
44. Xue, F.; Zhang, X.; Luo, H.; Tan, T. *Proc. Biochem.* **2006**, 4, 1699-1702.
45. Metting, B.; Pyne, J. W. *Enzyme Microb. Technol.* **1986**, 8, 386-394.
46. Spolaore, P.; Joannis-Cassan, C.; Duran, E.; Isambert, A. *J. Biosci. Bioeng.* **2006**, 101, 87-96.
47. Halim, R.; Danquah, M. K.; Webley, P. A. *Biotechnol. Adv.* **2012**, 30, 709-732.
48. Schenk, P. M.; Thomas-Hall, S. R.; Stephens, E.; Marx, U. C.; Mussnug, J. H.; Posten, C.; Kruse, O.; Hankamer, B. *BioEnergy Res.* **2008**, 1, 20-43.
49. Becker, E. W. *Biotechnol. Adv.* **2007**, 25, 207-210.
50. Ratledge, C. *Trends Biotechnol.* **1993**, 11, 278-284.
51. Ratledge, C.; Wynn, J. P. *Adv. Appl. Microbiol.* **2002**, 51, 1-51.
52. Belarbi, E. H.; Molina, E.; Chisti, Y. *Enzyme Microb. Technol.* **2000**, 26, 516-529.
53. Becker, E. W. *Microalgae: Biotechnology and microbiology*. Cambridge University Press, New York: 1994, pp 293.
54. Aach, H. G. *Arch. Mikrobiol.* **1952**, 17, 213-246.
55. Zhila, N. O.; Kalacheva, G. S.; Volova, T. G. *Botryococcus braunii Kutz IPPAS H-252. Russ. J. Plant Physiol.* **2005**, 52, 357-365.
56. Talebi, A. F.; Mohtashami, S. K.; Tabatabaei, M.; Tohidfar, M.; Bagheri-Zeinalabedini, M.; Hadavand-Mirzaei, H.; Mirzajanzadeh, M.; Shafaroudi, S. M.; Bakhtiari, S. *Algal Res.* **2013**, 2, 258-267.
57. Chen, L.; Liu, T.; Zhang, W.; Chen, X.; Wang, J. *Bioresour. Technol.* **2012**, 111, 208-214.
58. Halim, R.; Gladman, B.; Danquah, M. K.; Webley, P. A. *Bioresour. Technol.* **2011**, 102, 178-185.
59. Yu, X.; Zhao, P.; He, C.; Li, J.; Tang, X.; Zhou, J.; Huang, Z. *Bioresour. Technol.* **2012**, 121, 256-262.
60. Levine, R. B.; Costanza-Robinson, M. S.; Spatafora, G. A. *Biomass Bioenergy*. **2011**, 35, 40-49.
61. Song, M.; Pei, H.; Hu, W.; Ma, G. *Bioresour. Technol.* **2013**, 141, 245-251.
62. Carlos, A.; Guerrero, F.; Guerrero-Romero, A.; Fabio, E. Sierra. Biodiesel Production from Waste Cooking Oil, In: *Biodiesel-Feedstocks and Processing Technologies*; Margarita Stoytcheva and Gisela, Eds.; Intech Open Acces Publisher: Montero, 2011; .pp.23-44.
63. Tsukii, M.; Nakamori, H.; Hirano, K. *J. Japan Inst. Energy* **2008**, 87, 291-296.
64. Canakci, M. *Bioresour. Technol.* **2007**, 98, 1167-1175.
65. Canakci, M.; Gerpen, J. V. *Trans. ASAE*, **1999**, 42(5), 1203-1210.
66. Rude, M. A.; Schirmer, A. *Curr. Opin. Microbiol.* **2009**, 12, 274-281.
67. Kosa, M.; Ragauskas, A. J. *Trends Biotechnol.* **2011**, 29, 53-60.
68. Muller, E. E. L.; Sheik, A. R.; Wilmes, P. *Curr. Opin. Biotechnol.* **2014**, 30, 9-16.

DOI: <http://dx.doi.org/10.32571/ijct.623165>

E-ISSN:2602-277X

69. Liu, X.; Sheng, J.; Curtis, R. *Proc. Natl. Acad. Sci.* **2011**, 108, 6899-6904.
70. Gohel, H.R.; Ghosh, S.K.; Braganza, V.J. *Int. J. Renew. Energy Res.* **2013**, 3(1), 126-131.
71. Hetzler, S.; Steinbüchel, A. *Appl. Environ. Microbiol.* **2013**, 79, 3122-3125.
72. Alvarez, H. M.; Mayer, F.; Fabritius, D.; Steinbüchel, A. *Arch. Microbiol.* **1996**, 165, 377-386.
73. Olukoshi, E. R.; Packter, N. M. *Microbiol-SGM*, **1994**, 140, 931-943.
74. Röttig, A.; Wenning, L.; Bröker, D.; Steinbüchel, A. *Appl. Microbiol. Biotechnol.* **2010**, 85, 1713-1733.
75. Kalscheuer, R.; Stölting, T.; Steinbüchel, A. *Microbiol-SGM*, **2006**, 152, 2529-2536.
76. Steen, E. J.; Kang, Y.; Bokinsky, G.; Hu, Z.; Schirmer, A.; McClure, A.; Del-Cardayre, S. B.; Keasling, J. D. *Nature* **2010**, 463, 559-562.
77. Tao, H.; Guo, D.; Zhang, Y.; Deng, Z.; Liu, T. *Biotechnol. Biofuel.* **2015**, 8, 92-103.
78. Salis, A.; Pinna, M.; Monduzzi, M.; Solinas, V. *J. Biotechnol.* **2005**, 119, 291-299.
79. Helwani, Z.; Othman, M. R.; Aziz, N.; Fernando, W. J. N.; Kim, J. *Fuel Proces. Technol.* **2009**, 90(12), 1502-1514.
80. Vasudevan, P. T.; Fu, B. *Waste Biomass Valori.* **2010**, 35(5), 421-430.
81. Atadashi, I. M.; Aroua, M. K.; Aziz, A. *Renew. Sust. Energy Rev.* **2010**, 14 (7), 1999-2008.
82. Marchetti, J. M.; Miguel, V. U.; Errazu, A. F. *Fuel Proces. Technol.* **2008**, 89, 740-748.
83. Fukuda, H.; Kondo, A.; Noda, H. *J. Biosci. Bioeng.* **2001**, 92, 405-416.
84. Freedman B, Pryde E .H. Mounts, T. L. *J. Am. Oil Chem. ' Soc.* **1984**, 61, 1638-1643.
85. Kusdiana, D.; Saka, S. *Fuel* **2001**, 80, 693-698.
86. Silas, K.; Kwaji, H. B.; Gutti, B. *Int. J. Recent Res. Phys. Chem. Sci.* **2015**, 2 (1), 26-37.
87. Thanh, L. T.; Kenji, O.; Luu, V.; Yasuaki, M. *Catalysts* **2012**, 2, 191-222.
88. Ito, T.; Sakurai, Y.; Kakuta, Y.; Sugano, M.; Hirano, K. *Fuel Proces. Technol.* **2012**, 94, 47-52.
89. Salvi, B. L.; Panwar, N. L. *Renew. Sust. Energy Rev.* **2012**, 16, 3680-3689.
90. Ejikeme, P. M.; Anyaogu, I. D.; Ejikeme, C. L.; Nwafor, N. P.; Egbuonu, C. A. C.; Ukogu, K.; Ibemesi, J. A. *E-J. Chem.* **2010**, 7 (4), 1120-1132.
91. Freedman, B.; Butterfield, R. O.; Pryde, E. H. *J. Am. Oil Chem. ' Soc.* **1986**, 63, 1375-1380.
92. Akoh, C. C.; Chang, S.; Lee, G.; Shaw, J. J. *Agric. Food Chem.* **2007**, 55, 8995-9005.
93. Fjerbaek, L.; Christensen, K. V.; Norddahl, B. *Biotechnol. Bioeng.* **2009**, 102, 1298-1315.
94. Vasudevan, P. T.; Briggs, M. J. *Ind. Microbiol. Biotechnol.* **2008**, 35, 421-430.
95. Robles-Medina, A.; Gonzalez-Moreno, P. A.; Esteban-Cerdán, L.; Molina-Grima, E. *Biotechnol. Adv.* **2009**, 27, 398-408.
96. Jeong, G. T.; Park, D. H. *Appl. Biochem. Biotechnol.* **2008**, 14, 8131-8139.
97. Qin, H.; Yan, X.; Dong, W. *Chinese J. Catal.* **2008**, 29, 41-46.
98. Tamalampudi, S.; Talukder, R. M.; Hamad, S.; Numatab, T.; Kondo, A. *Biochem. Eng. J.* **2008**, 39, 185-189.

ORCID

<https://orcid.org/0000-0002-3682-9756> (İ. Ekin)



Recombinant human G-CSF production as a protein based drug candidate for hematology and oncology

Yasemin BOZKURT¹, Sema BİLGİN², Seçil ERDEN TAYHAN^{1,*}, İsmail Furkan TURAN¹, İsa GÖKÇE¹

on the last page

¹Department of Genetics and Bioengineering, Faculty of Engineering and Natural Sciences, Tokat Gaziosmanpaşa University, Tokat, Turkey

²Department of Chemistry, Faculty of Art and Science, Tokat Gaziosmanpaşa University, Tokat, Turkey

Received: 5 August 2019; Revised: 18 September 2019; Accepted: 20 September 2019

*Corresponding author e-mail: ysecilerden@gmail.com

Citation: Bozkurt, Y.; Bilgin, S.; Erden Tayhan, S.; Turan, İ. F.; Gökçe, İ. *Int. J. Chem. Technol.* 2019, 3 (2), 92-100.

ABSTRACT

The human granulocyte colony stimulating factor (hG-CSF) is a member of the CSF family. The first purpose of this study was production of recombinant human G-CSF (rhG-CSF) which is an important therapeutic protein for angiogenesis based clinical applications. rhG-CSF was produced as inclusion body in the *Escherichia coli* strain BL21 (DE3) pLysE with pTOLT vector system. The rhG-CSF was purified by Ni-NTA agarose affinity chromatography and characterized with SDS-PAGE analysis. The effects of this therapeutic protein on cell viability was measured by MTT assay. Additionally, angiogenic potential of produced rhG-CSF was investigated via HUVEC cell line by *in vitro* scratch assay. As a result, the purified protein induced cell proliferation and the EC50 value of protein based drug candidate was 0.051 mM. Additionally, it was determined that the migration ability of the HUVECs was promoted by rhG-CSF in a concentration-dependent manner by *in vitro* scratch assay.

Keywords: Granulocyte colony stimulating factor, recombinant proteins, angiogenesis, cell proliferation.

Hematoloji ve onkoloji için protein esaslı bir ilaç adayı olarak rekombinant insan G-CSF üretimi

ÖZ

İnsan granülosit koloni uyarıcı faktör (hG-CSF), CSF ailesinin bir üyesidir. Bu çalışmanın temel amacı, anjiyogenez bazı klinik uygulamalar için önemli bir terapötik protein olan rekombinant insan G-CSF (rhG-CSF)'sinin üretimi olarak belirlenmiştir. rhG-CSF, bir *Escherichia coli* suşu olan BL21 (DE3) pLysE'de pTOLT vektör sistemi ile inklüzyon cisimciği olarak üretilmiştir. rhG-CSF, Ni-NTA agaroz afinite kromatografisi aracılığıyla saflaştırılmış ve SDS-PAGE analizi ile karakterize edilmiştir. Bu terapötik proteinin hücre canlılığı üzerine etkisi MTT testi ile değerlendirilmiştir. Ek olarak, üretilen rhG-CSF'nin anjiyogenik potansiyeli, HUVEC hücre hattı ile gerçekleştirilen *in vitro* çizik analizi ile araştırılmıştır. Sonuçta, saflaştırılmış proteinin hücre proliferasyonunu arttırdığı görülmüş ve protein temelli bu ilaç adayının EC50 değeri, 0.051 mM olarak hesaplanmıştır. Ek olarak, HUVEC hücrelerinin migrasyon yeteneklerinin rhG-CSF ile konsantrasyona bağlı bir şekilde arttığı belirlenmiştir.

Anahtar Kelimeler: Granülosit koloni uyarıcı faktör, rekombinant proteinler, anjiyogenez, hücre proliferasyonu.

1. INTRODUCTION

The human granulocyte colony stimulating factor (hG-CSF), a glycoprotein, is a member of the CSF family.¹⁻³ It is a cytokine which have many functions such as stimulating of hematopoiesis and production of bone marrow neutrophilic granulocyte colonies.⁴ A

recombinant form of G-CSF is used to accelerate the treatment success of neutropenic after chemotherapy and allow higher-intensity treatment regimens in some cancer patients in oncology and hematology. Angiogenesis is the new blood vessel formation that occur with proliferation and migration of endothelial cells. These cells form the inner surface of the blood vessels that feed

the other surrounding cells with oxygen and nutrients. The effect of G-CSF on these cells is rarely investigated and the results are still uncertain.⁵ According to this comprehensive application, the rhG-CSF has been expressed in various expression host systems. Three forms of it are suitable for clinical use: a glycosylated form obtained by expression in mammalian cell line (*Chinese Hamster Ovary*) (such as Lenograstim), a non-glycosylated form expressed in an *E. coli* expression system (such as Filgrastim and Nartograstim) and second-generation G-CSF (such as Pegfilgrastim).⁶⁻⁸ Researches on the cloning, expression and purification of rhG-CSF have been carried out in order to eliminate the limitations of production efficiency and cost. Because in the pharmaceutical industry, the production of bioproducts requires a simple and cost-effective process that includes easier steps with high throughput. Therefore, studies on the expression of recombinant rhG-CSF using various expression hosts such as *P. Pastoris*,^{1,10-11} in tobacco BY-2 cells,¹⁰ in *S. cerevisiae*² and in *P. fluorescens*¹² by a number of research group have been performed (Table 1).

E. coli is a frequently used host for the production of recombinant protein.^{12,13} Additionally, the advantages of a low-cost and fast high density cultivation, and the availability of several of cloning vectors and engineered host strains enable *E. coli* to provide an average for the high yield and economic production of recombinant proteins.^{15,16} Nevertheless the *E. coli* recombinant protein production system has several disadvantages. For instance, overexpression of recombinant proteins in *E. coli* often results in insoluble and nonfunctional proteins, so called inclusion bodies (IBs).¹⁷ Various techniques are used to solve this problem, such as the use of different promoters and host strains, coexpression of chaperones and optimization culture conditions.^{13,14} On the other hand, the production of the recombinant protein referred to as inclusion body has not only disadvantages, but also has some advantages.^{15,18} The primary advantage is the ease of purification of IBs and it contains high degree purity of target protein.¹⁷ Additionally IBs are often an advantage when the yield of the native protein is low because of extensive proteolysis.¹⁸

In this study, codon-optimized mature hG-CSF gene was cloned into our patented inducible high-copy pTOLT expression plasmid and rhG-CSF-TolA-III fusion protein was produced as inclusion body in the *E. coli* strain BL21 (DE3) pLysE. In the pTOLT vector, the proteins bind to the C-terminus of TolAIII by a short linker containing the thrombin recognition site. Furthermore it also carries an N-terminal 6xHis-tag for the purpose of purification. TolAIII is small domain that is achieved high product yields as a soluble protein in the cytoplasm of *E. coli*. Thus, pTOLT, in which the TolAIII domain is

used as a fusion protein partner, is an expression vector with remarkable properties that enable proteins to be expressed at high levels in recombinant cells in a host cell. Up to 90 mg fusion protein per liter bacterial culture was obtained using pTOLT vector.^{19,21} Obviously human G-CSF protein has been recombinantly produced using several prokaryotic expression vectors (Table 1), but no recombinant human G-CSF (rhG-CSF) production using the pTOLT vector system. Using this vector system, it is aimed to produce hG-CSF in *E. coli* in higher amount. Because the increased production of recombinant proteins is important to obtain a higher amount of functional product per unit volume and per unit time.

In this context hG-CSF was produced as inclusion body. At first, IBs were isolated, IBs were solubilized and refolded. Finally, the hG-CSF was purified by Ni-NTA agarose affinity chromatography. Then recombinantly produced hG-CSF was tested on human umbilical vein endothelial cells (HUVECs) at different concentrations to understand the effect of G-CSF on endothelial cells. Additionally, the cell migration process which is the crucial step for angiogenesis was investigated by an *in vitro* scratch assay. This assay is an easy, inexpensive and well-developed technique for the investigation of cell migration *in vitro*.¹⁶

2. MATERIALS AND METHODS

2.1. Codon optimization and Construction of G-CSF expression plasmids

In this work, codon optimization was performed with the aim of the gene expression in desired level in *E. coli*. To improve the expression levels of the hG-CSF gene, the gene sequence was recoded on the basis of the codon preference characteristics of *E. coli* K12 organism, without differentiating the amino acid sequence of the corresponding proteins. Online optimization software [Java Codon Adaptation Tool (JCat)] was used for codon design. The nucleotide sequence of the hG-CSF protein optimized for the *E. coli* organism is given in Figure 1. Plasmid containing the optimized G-CSF coding nucleic acid sequence was purchased from BIOMATIK (Clone ID: S2543-2, Gene ID: L5165K). DNA sequence encoding for G-CSF was amplified using specific primers which are contained *SacI* and *KpnI* restriction sites (Table 2). The PCR amplification product was inserted into pTOLT expression vector (Figure 2), that added a N-terminal six-histidine tag, using *SacI* and *KpnI* restriction sites. *E. coli* DH5 α cells which is the host strain for cloning were transformed with the pTOLT-G-CSF plasmid. Transformation mix were spread on LB agar culture plates including ampicillin (0.1 g ml⁻¹) and they were incubated at 37°C overnight. After transformation, plasmids isolated from positive clones were screened by PCR and then analyzed by DNA sequencing.

Table 1. Recombinant hG-CSF expression systems

Expression host	Expression vector	Soluble/Insoluble Form	rhG-CSF concentration	Reference
<i>E. coli</i> BL21 (DE3)	pET23a	Inclusion body (insoluble)	-	17,18
<i>E. coli</i> BL21 (DE3)	pET22b	Inclusion body (insoluble)	60 µg ml ⁻¹	21
<i>E. coli</i> BL21 (DE3)	pET28a	-	-	22
<i>E. coli</i> M15	pQE3	Inclusion body (insoluble)	-	3
<i>P. pastoris</i> strain GS115	pPIC9	Soluble	3.1 mg l ⁻¹	23,24
<i>P. pastoris</i> strain SMD1168H	pPICZa	Soluble	50.66 µg ml ⁻¹	25
<i>Saccharomyces cerevisiae</i>	pIL20GC	Soluble	232.7 mg l ⁻¹	6
<i>Aspergillus niger</i>	pAN56-2M	Soluble	5 mg l ⁻¹	1
<i>Pseudomonas fluorescens</i> strain DC454		Soluble	350 mg l ⁻¹	26
<i>Tobacco Bright Yellow-2</i>	pMDC83	Soluble	4.19 mg l ⁻¹	27
(BY-2) cells	pMDC43	Soluble	17.89 mg l ⁻¹	27

Table 2. Oligonucleotides employed to obtain the DNA sequence of HG-CSF by PCR amplification

Primers	Sequence
GCSF <i>SacI</i> TolT sense	TTTTTGAGCTCATGGCAGGCCCTGCT
GCSF <i>KpnI</i> TolT antisense	TTTTTGGTACCTCAGGGTTGGGCCAA

Wild	ATGGCCGGCCCCGCCACCCAGAGCCCCATGAAGCTGATGGCCCTGCAGCTGCTGCTGTGG	60
Optimize	ATGGCTGGTCCGGCTACCCAGTCTCCGATGAAACTGATGGCTCTGCAGCTGCTGCTGTGG	60
Wild	CACAGCGCCCTGTGGACCGTGCAGGAGGCCACCCCCCTGGGCCCGCCAGCAGCTGCC	120
Optimize	CACTCTGCTCTGTGGACCGTTCAAGGAGCTACCCCGCTGGGTCCGGCTTCTTCTGCCG	120
Wild	CAGAGCTTCTGCTGAAGTGCCTGGC--AGGTGCGCAAGATCCAGGGCGACGGCGCCGCC	178
Optimize	CAGTCTTCTGCTGAAATGCCTGGAACAGGTTCTGAAAATCCAGGGTGACGGTGTCTGCT	180
Wild	CTGCAGGAGAAGCTGGTGAGCGAGTGCGCCACCTACAAGCTGTGCCACCCCCGAGGAGCTG	238
Optimize	CTGCAGGAAAAACTGGTTTCTGAATGCGCTACCTACAAACTGTGCCACCCGGAAGAACTG	240
Wild	GTGCTGCTGGGCCACAGCCTGGGCATCCCCCTGGGCCCCCCCTGAGCAGCTGCCCGAGCCAG	298
Optimize	GTTCTGCTGGGTCACTCTCTGGGTATCCCGTGGGCTCCGCTGTCTTCTTCCCGTCTCAG	300
Wild	GCCCTGCAGCTGGCCGGCTGCCTGAGCCAGCTGCACAGCGGCCTGTTCTGTACCAGGGC	358
Optimize	GCTCTGCAGCTGGCTGGTTGCCGTCTCAGCTGCACCTCTGGTCTGTTCTGTACCAGGGT	360
Wild	CTGCTGCAGGCCCTGGAGGGCATCAGCCCCGAGCTGGGCCCCACCCTGGACACCTGCAG	418
Optimize	CTGCTGCAGGCTCTGGAAGGTATCTCTCCGAACTGGGTCCGACCTGGACACCTGCAG	420
Wild	CTGGACGTGGCCGACTTCGCCACCACCATCTGGCAGCAGATGGAGGAGCTGGGCATGGCC	478
Optimize	CTGGACGTGCTGACTTCGCTACCACCATCTGGCAGCAGATGGAAGAAGCTGGGTATGGCT	480
Wild	CCCGCCCTGCAGCCACCCAGGGCGCCATGCCCGCCTTCGCCAGCGCCTTCCAGCGCCGC	538
Optimize	CCGGCTCTGCAGCCGACCCAGGGTGCATGCGCGCTTTCGCTTCTGCTTTCCAGCGCTG	540
Wild	GCCGGCGGCGTGTGGTGGCCAGCCACCTGCAGAGCTTCTGGAGGTGAGCTACCAGCGTG	598
Optimize	GCTGGTGGTGTCTGGTTGCTTCTCACCTGCAGTCTTTCCTGGAAGTTTCTTACCAGTGT	600
Wild	CTGCGCCACCTGGCCAGCCC	619
Optimize	CTGCGTACCTGGCTCAGCCG	621

Figure 1. The multiple alignment of optimized and wild-type DNA sequence of G-CSF by using ClustalW2 program.

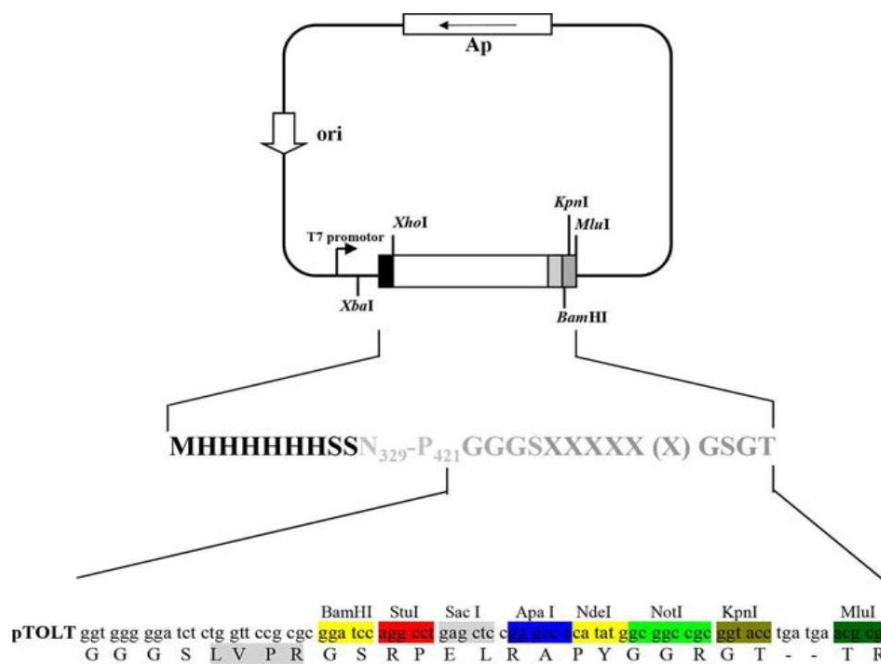


Figure 2. pTOLT cloning region.¹³

2.2. Protein expression

In this work, the host cell *E. coli* strain BL21 (DE3) pLysE (Novagen, Inc.) was used for rhG-CSF expression. This strain was transformed by recombinant plasmid pTOLT-G-CSF. Transformed cells were spread on several LB agar plates including both 0.1 mg ml⁻¹ ampicillin, chloramphenicol (34 µg m l⁻¹) and grown at 37°C overnight. One colony of BL21(DE3) pLysE recombinant was cultivated in 4ml of selective LB medium and was grown at 37°C, with shaking (240 rpm) for 16 h. This overnight culture was inoculated into 600 ml of selective LB and incubated at 37°C with shaking (240 rpm) until the OD₆₀₀ was 0.6. The expression of recombinant hG-CSF was induced by IPTG and then the cultures were grown for an additional 3 h. The culture was harvested by centrifugation and the cell pellets were resuspended in buffer A (100 mM Tris-HCl buffer (pH 7.0) containing 1 g l⁻¹ lysozyme, 1 mM PMSF and 1mM benzamidine. The bacterial cells were lysed using a sonicator (Sonics VCX 130), soluble and insoluble fraction were separated via centrifugation (Vision VS-30000i) at 30.000 rpm for 1 hour at 4°C.

2.3. Refolding and recombinant G-CSF purification

The IBs were resuspended in 10 ml (5 ml g⁻¹ wet weight pellet) of buffer A containing 5 mM EDTA, 5 mM DTT, 2 M urea, 2% (w/v) triton X-100 and sonicated four cycle for 5 minutes at 60-65% of the maximum power in a sonicator (Sonics VCX 130) followed by centrifugation (27.000 rpm for 20 min at 4°C). The inclusion body wash step was repeated three times. The washed pellet obtained in previous step was resuspended in 6 mL of buffer A containing 5 mM EDTA and 5 mM DTT. And then resuspension were shaken on an orbital shaker at 150 rpm at 25°C for 30 min. The washed inclusion bodies were dissolved by adding a freshly prepared buffer B (50 mM Tris-HCl pH 7.0, 5 mM EDTA, 8 M Guanidine-HCl, 5 mM DTT) dropwise with the aid of a pasteur pipette (4 ml g⁻¹ wet weight pellet). The solution was incubated at 25°C for 60 min with shaking (150 rpm) then solubilized inclusion bodies were refolded by refolding buffer (100 mM Tris-HCl pH 8.0, 10 mM DTT, 20% gliserol (w/v) and incubated 4 hours at 4°C. Refolded G-CSF was dialyzed against 25 mM, pH 7.8 Tris-HCl buffer containing 100 mM NaCl at 4°C for 16 hours. Qiagen Ni-NTA metal-affinity chromatographic procedure was used to purification of soluble recombinant protein carrying N-terminal 6x histidine. Purity of rhG-CSF was determined by 12% SDS-PAGE²⁸ and visualized by commasie blue. The UV absorbance at 280 nm was used to determine protein concentration.²⁹

2.4. Investigation of *in vitro* stimulating effect of rhG-CSF on HUVECs proliferation

HUVECs were cultured in DMEM with 15% FBS. These cells were cryopreserved in liquid nitrogen previously in our animal cell culture laboratory. *In vitro* stimulating effect of G-CSF on HUVECs proliferation was investigated using MTT (3-(4,5-dimethylthiazol-2-yl)-2,5-diphenyltetrazolium bromide) assay.³⁰

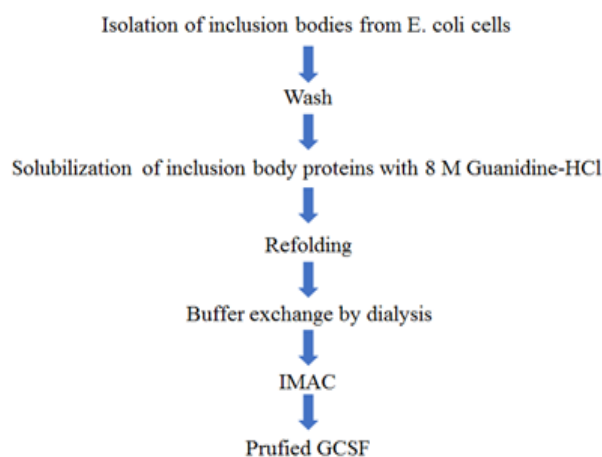


Figure 3. Steps of the refolding protocol and G-CSF purification.

This test was performed at different concentrations (100-1.62 mM) and cells were left in contact with rhG-CSF for 48 hours. In this experiment, the cells were plated in triplicates and treated for 3 hours with MTT solution (0.5 g l⁻¹). Following the MTT removal after this incubation period, purple formazan products were dissolved completely by DMSO. The absorbance of the colored solution was measured by microplate reader at 570 nm. The results are expressed as the concentration that stimulates growth of cell by 50% against control cells (control group received only media without any rhG-CSF) EC50 (half maximal effective concentration) and were calculated by a regression analysis using GraphPad Prism 6 software for HUVECs.³¹

2.5. Cell migration assay

In the present study, preliminary investigation was performed to consider the effect of rhG-CSF on HUVECs migration by *in vitro* scratch assay. This test is used widely to measure migration, as it provides a simple and economical installation for modelling angiogenesis. The first step created an artificial wound in a cell monolayer. In this study, for *in vitro* scratch assay, the HUVEC cell suspension was dispensed onto six well cell culture plate. When the cells reached to 90% confluency at this plate, the cell monolayer was scraped with p200 pipette tip to create a scratch. The debris was removed and smoothed the scratched edge by washing the cells with culture medium. Then cells were incubated with rhG-CSF containing media of different concentrations

(100-1.62 mM) which were tested by MTT assay also. During incubation period (48 hours), cell images were captured by a phase contrast inverted microscope and quantitatively analyzed by image analysis software provided by Olympus. Finally, percent wound healing was calculated and the results were plotted.^{32,33}

3. RESULTS AND DISCUSSION

3.1. Codon optimization and Construction of G-CSF expression plasmids

In this work, rare codon-free hG-CSF gene was cloned into pTOLT expression vector. Using the recombinant plasmid containing hG-CSF gene as the template, the DNA sequences of hG-CSF gene were amplified by PCR. After running a 2.0% agarose gel, the amplified fragments were 624 bp, which was consistent with the reported size of hG-CSF (Figure 4) Sanger sequencing analysis verified that the DNA sequences were corrected. Recombinant plasmid containing hG-CSF gene was used to express hG-CSF protein.

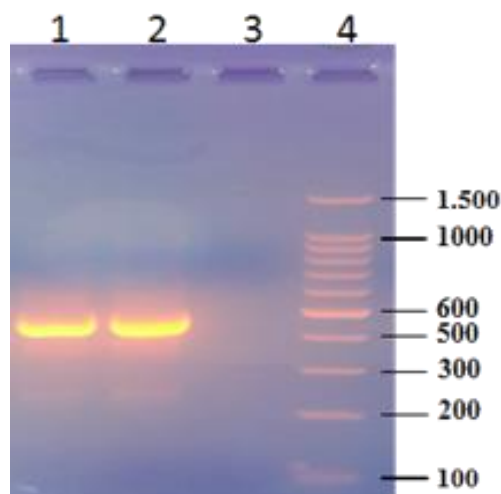


Figure 4. Agarose gel (2.0 %) electrophoresis result showing PCR verification of recombinant plasmid pTOLT-G-CSF after the cloning. Columns 1-2 positive 624 bp product indicates that G-CSF gene fragment correctly inserted into pTOLT system. Column 4 λ -EcoR I/Hind III DNA marker.

3.2. Protein expression, protein refolding and recombinant G-CSF purification

Recombinant hG-CSF was expressed and purified as described in materials and methods. The molar absorption coefficient and molecular weight of Tol-A-III-G-CSF fusion protein were calculated as $32430 \text{ M}^{-1} \text{ cm}^{-1}$ and 34551.89 Dalton using “ExpASy ProtParam tool”, respectively. Afterwards the purified Tol-A-III-G-CSF fusion protein concentration was determined as 1.78 mg ml^{-1} by absorbance at 280 nm using UV spectrophotometer (Varian Cary 50). The recombinant

TolAIII-G-CSF expression was confirmed by SDS PAGE. The SDS-PAGE analysis showed that the purified TolAIII-GCSF fusion protein around 34 kDa (Figure 5) (which corresponds with a theoretical molecular weight of 34551.89 kDa).

When the image of SDS-PAGE was examined, it was observed that the protein in the inclusion body form in the pellet obtained after high speed centrifugation was quite pure. Therefore, in this study, it is necessary to optimize these steps in order to minimize protein loss in refolding and purification stage.

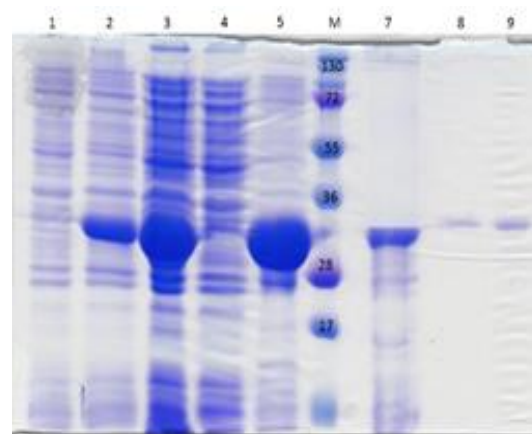


Figure 5. Coomassie-stained SDS-PAGE (12%) analysis 1. Bacterial cell lysates before IPTG addition, 2. Bacterial cell lysates after IPTG addition 3. total bacterial cell lysate of *E. coli* BL21 (DE3)pLysE [pTOLT-hG-CSF] after sonication, 4. Collected supernatant after centrifugation of the lysate, 5. Collected pellet after centrifugation of the lysate, 6. BioRad dual colour precision plus protein marker 7. Refolded Tol-III-A-hG-CSF fusion protein 8-9. purified Tol-III-A-hG-CSF fusion protein.

3.3. Investigation of *in vitro* stimulating effect of rhG-CSF on HUVECs proliferation

In the present study, HUVECs were cultured until they reached 70%-80% confluency (Figure 6).



Figure 6. Inverted microscope image taken from HUVECs (The scale bars indicated $100 \mu\text{m}$ for $\times 4$ magnification).

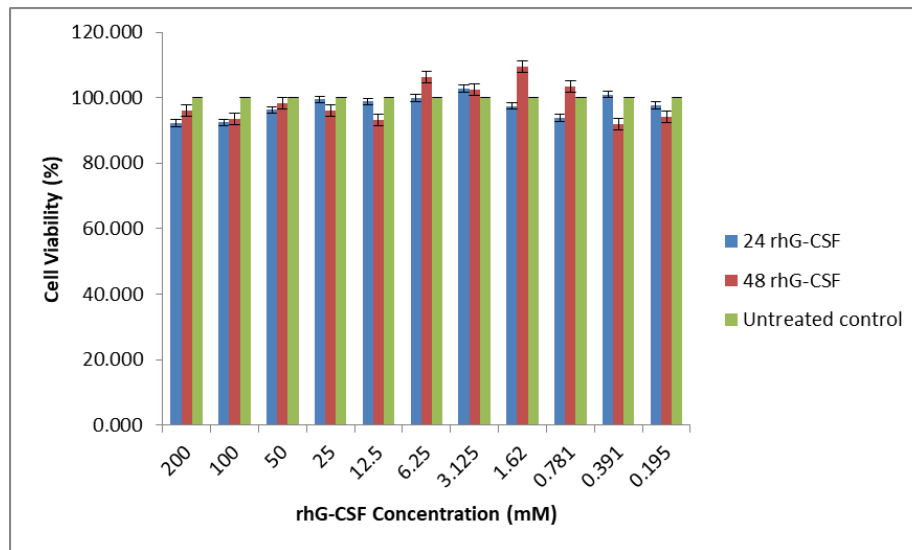


Figure 7. *In vitro* stimulating effect of rhG-CSF on HUVEC cell proliferation.

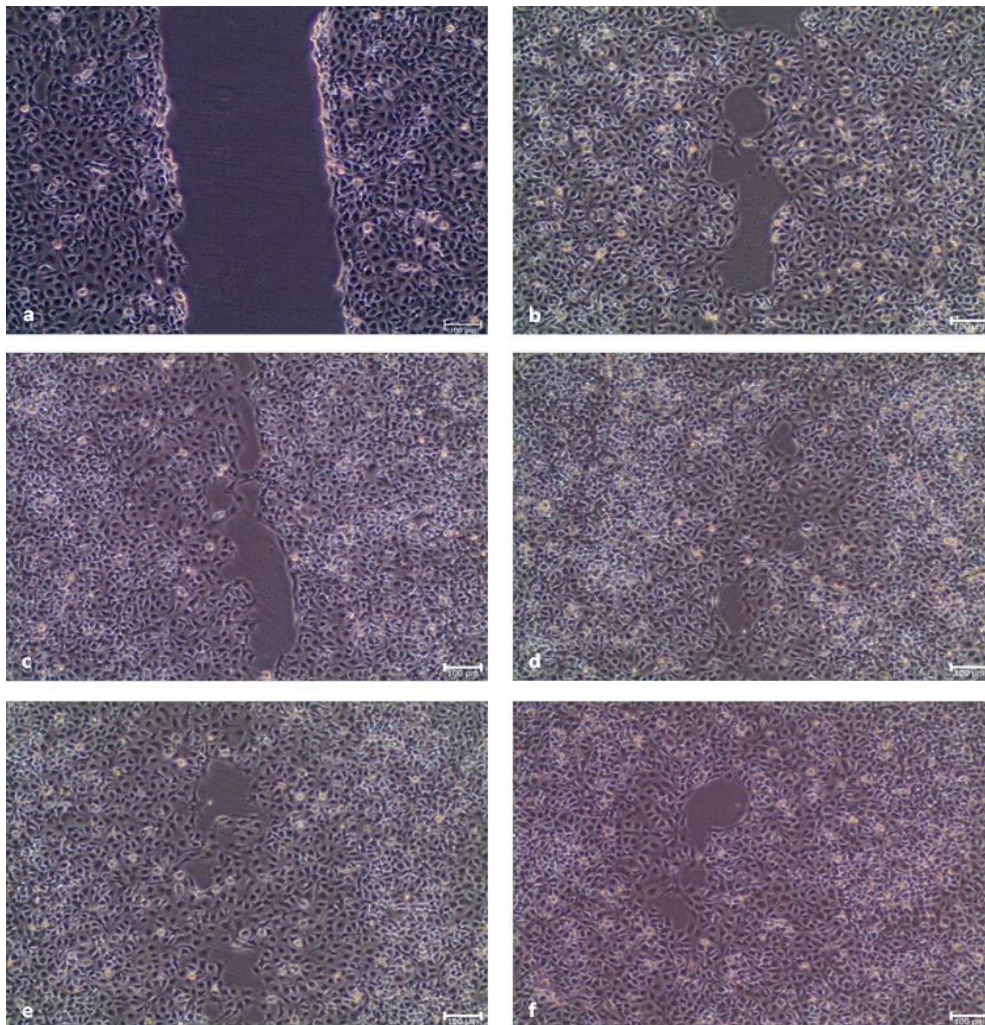


Figure 8. Inverted light microscope images of HUVECs after scratching (a: 0 hour, b-f: 24 hours). The scale bars indicated 100 μ m for x4 magnification (b: untreated control, c: HUVECs incubated with 100 mM G-CSF, d: HUVECs incubated with 25 mM G-CSF, e: HUVECs incubated with 6,25 mM G-CSF, f: HUVECs incubated with 1,62 mM G-CSF).

To investigate the *in vitro* biological activity of rhG-CSF, HUVECs cells were incubated with this therapeutic protein. For this purpose, MTT assay was performed and cell viabilities were calculated to determine effective concentration for cell proliferation. As a result, HUVECs which were incubated with rhG-CSF at 1.62 mM concentration for 48 hours, demonstrated the highest cell viability against negative control (Figure 7). Additionally, the EC50 value of the recombinantly produced rhG-CSF protein was calculated as 0.051 mM.

3.4. Cell migration assay

We examined the migration ability of HUVECs to determine the effect of rhG-CSF treatment on the angiogenesis potential of endothelial cells *in vitro*. For this purpose, *in vitro* scratch assay was carried out with HUVEC cells at four different rhG-CSF concentrations (100-1.62 mM) (Figure 8).

It was clearly observed that following 24 hours of incubation of the rhG-CSF with HUVEC cells, the percent wound healings was calculated as 73.9 %, 86.09 %, 82.07 %, 87.94 % respectively (Figure 4). When this data was compared with untreated control (77.2 %), it was concluded that the migration and wound closure ability of the HUVECs was promoted by rhG-CSF at 24 h in a concentration-dependent manner (25 mM, 6.25 mM, 1.62 mM) and peaked at 1.62 mM (Figure 9).

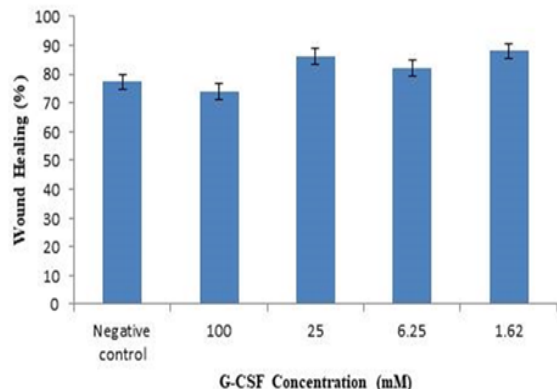


Figure 9. The percent wound healings for HUVECs.

4. CONCLUSIONS

In this study, we have constructed the pTOLT-G-CSF that permits the production of *E. coli* Tol-A-III domain of Tol-A protein and mature peptide of hG-CSF fusion under control of the T7 promoter system. The construct was prepared with the addition of 6xHis-tag which was used for the purification of this fusion protein by a single affinity chromatography step. Recombinant hG-CSF was overexpressed as inclusion body in *E. coli* B121pLysE expression host using this construct. Inclusion body formation should not always be considered a disadvantage. Sometimes it can provide a good alternative to successful purification, especially when

high purity protein cannot be obtained due to host contaminants. In this case, however, the solubilization and refolding steps should be revised to high recovery of bioactive recombinant protein from the inclusion bodies. Although rhG-CSF production in the present study was at the sufficient level as amount, refolded active form of protein was low. This problem can be solved optimizing refolding condition for better yield. Additionally, the hG-CSF can be separated from the Tol-A-III protein fusion and 6xHis-tag for higher activity, nevertheless this additional process increases the cost of protein production and causes a loss in the amount of protein. In the pharmaceutical industry, the production of bioproducts requires a simple and cost-effective process that includes easier steps with high throughput.

In the early 1990s, *in vitro* studies had demonstrated that rhG-CSF ($0.1 \mu\text{g ml}^{-1}$) had direct stimulating effects on HUVECs showing a positive effect on the cell viability and motility. Additionally, recent studies had further shown that by local administration of lower doses, rhG-CSF may provide a beneficial environmental conditions for angiogenesis. However, in another *in vitro* study, controversial results were reported. According to these findings, rhG-CSF induced apoptosis and inhibited cell proliferation when administrated systematically at a relatively higher doses.¹⁵ In the present study, it was observed that the rhG-CSF demonstrated positive effect on proliferation and migration of HUVECs in a concentration dependent manner.^{15,33} Therefore, the results we obtained in our study were consistent with the previous findings.

In conclusion, it was observed that when rhG-CSF administrated at true doses (25 mM, 6.25 mM, 1.62 mM) in HUVECs. rhG-CSF stimulated the cell migration through extracellular matrix, which was a crucial process during angiogenesis. Nevertheless, it should be clear that further analysis is needed to assess the angiogenesis mechanism on the basis of rhG-CSF.

ACKNOWLEDGEMENTS

This study was financially supported by the Tokat Gaziosmanpasa University Scientific Research Project (2016/61). Additionally, Yasemin BOZKURT was supported by TUBITAK-BİDEB 2210/C National Scholarship Program for MSc students.

Conflict of interests

Authors declare that there is no a conflict of interest with any person, institute, company, etc.

REFERENCES

1. Krasevec, N.; Milunovic, T.; Lasnik, M. A.; Lukancic, I.; Komel, R.; Gaberc Porekar, V. *Acta Chim. Slov.* **2014**, 61, 709-717.

2. Carlsson, G.; Åhlin, A.; Dahllöf, G.; Elinder, G.; Henter, J. I.; Palmblad, J. *Brit. J. Haematol.* **2004**, 126 (1), 127-132.
3. Jiang, Y.; Jiang, W.; Qiu, Y., Dai, W.; *J. Hematol. Oncol.* **2011**, 4, 1-8.
4. Hill, C. P.; Osslund, T. D.; Eisenberg, D. *Proc. Natl. Acad. Sci.* **1993**, 90 (11), 5167-5171.
5. Liu, X. L.; Hu, X.; Cai, W. X.; Lu, W. W.; Zheng, L. W., *Biomed. Res. Int.* **2016**, 2016, 1-8.
6. Bae, C. S.; Yang, D. S.; Chang, K. R.; Seong, B. L.; Lee, J. *Biotechnol. Bioeng.* **1998**, 57 (5), 600-609.
7. Hongbao, M.; Yan, Y.; Yiwu, S.; Ma, M. *Stem Cell.* **2011**, 2(1), 36-65.
8. Sivakumar, R. *Immunome Res.* **2014**, 01 (s2), 1-8.
9. Hüttmann, A.; Schirsafi, K.; Seeber, S.; Bojko, P. *J. Cancer Res. Clin. Oncol.* **2005**, 131(3), 152-156.
10. Kubota, N.; Orita, T.; Hattori, K.; Oh-Eda, M.; Ochi, N.; Yamazaki, T. *J. Biochem.* **1990**, 107 (3), 486-492.
11. Clogston, C. L.; Hu, S.; Boone, T. C.; Lu, H. S. *J. Chromatogr. A*, **1993**, 637 (1), 55-62.
12. Choi, J. H.; Keum, K. C.; Lee, S. Y. *Chem. Eng. Sci.* **2006**, 61 (3), 876-885.
13. Sivashanmugam, A.; Murray, V.; Cui, C.; Zhang, Y.; Wang, J.; Li, Q. *Protein Sci.* **2009**, 18 (5), 936-948.
14. Jana, S.; Deb, J. K. *Appl. Microbiol. Biotechnol.* **2005**, 67 (3), 289-298.
15. Vallejo, L. F.; Rinas, U. *Microb. Cell Fact.* **2004**, 3, 1-12.
16. Christopher, M. J.; Link, D. C. *J. Bone Miner. Res.* **2008**, 23 (11), 1765-1774.
17. Babaeipour, V.; Khanchezar, S.; Mofid, M. R.; Abbas, M. P. H. *Iran. Biomed. J.* **2015**, 19 (2), 102-110.
18. Babaeipour, V.; Abbas, M. P. H.; Sahebazar, Z.; Alizadeh, R. *Bioproc. Biosyst. Eng.* **2010**, 33 (5), 591-598.
19. Anderluh, G.; Gökçe, I.; Lakey, J. H. *Protein Expr. Purif.* **2003**, 28 (1), 173-181.
20. Gokce, I.; Anderluh, G.; Lakey, J.H. United States Patent et al. Patent No USOO7348408B2, 2008.
21. Peymanfar, P.; Roghanian, R.; Ghaedi, K.; Sayed, H.; Yari, R. *Int. J. Med. Biotechnol. Genet.* **2016**, 4 (2), 40-46.
22. Tian, H.; Liu, C.; Gao, X.D.; Yao, W.B. *World J. Microb. Biot.* **2013**, 29 (3), 505-13.
23. Saeedinia, A.; Shamsara M.; Bahrami, A.; Zeinoddini, M.; Naseeri-Khalili, M. A.; Mohammadi, R.; Sabet, N. M.; Sami, H. *Biotechnology (Faisalabad)*, **2008**, 7 (3), 569-573.
24. Apte-Deshpande, A.; Somani, S.; Mandal, G.; Soorapaneni, S.; Padmanabhan, S. *J. Biotechnol.*, **2009**, 143 (1), 44-50.
25. Adiredja, Y.; Fuad, A. M. *Indones. J. Pharm.* **2018**, 29 (2), 94.
26. Jin, H; Cantin, G.T.; Maki, S; Chew, L. C.; Resnick, S. M.; Ngai, J; Retallack, D. M. *Protein Expr. Purif.*, **2011**, 78(1), 69-77.
27. Nair, N. R.; Chidambareswaren, M.; Manjula, S. *Mol. Biotechnol.* **2014**, 56 (9), 849-862.
28. Weber, K.; Pringle, J.; Osborn, M. *Methods Enzymol.* **1972**, 26, 3-27.
29. Cabrita, L. D.; Chow, M. K. M.; Bottomley, S. P. *Biotechnol. Annu. Rev.*, **2004**, 10 (1), 1-15.
30. İnan, A.; İköz, M.; Erden Tayhan, S.; Bilgin, S.; Genç, N.; Sayın, K.; Ceyhan, G.; Köse, M.; Dağ, A.; İspir, E. *New J. Chem.* **2018**, 42 (4), 2952-2963.
31. İnan, A.; Sünbül, A. B.; İköz, M.; Erden Tayhan, S.; Bilgin, S.; Elmastaş, M.; Sayın, K.; Ceyhan, G.; Köse, M.; İspir, E. *J. Organomet. Chem.*, **2018**, 870,76-89.
32. Liang, C. C.; Park, A. Y.; Guan, J. L. *Nat. Protoc.* **2007**, 2(2), 329-333.
33. Oh, J.; Hlatky, L.; Jeong, Y. S.; Kim, D. *Toxins (Basel)*. **2016**, 8 (7), 199.



-  <https://orcid.org/0000-0002-3456-3261> (Y. Bozkurt)
-  <https://orcid.org/0000-0001-5921-5434> (S. Bilgin)
-  <https://orcid.org/0000-0001-8473-5896> (S. Erden Tayhan)
-  <https://orcid.org/0000-0002-2391-1582> (İ. F. Turan)
-  <https://orcid.org/0000-0002-5023-9947> (İ. Gökçe)



Variation of Coster-Kronig enhancement factors at different excitation energies of the elements in the atomic number range $41 \leq Z \leq 49$

Rafet YILMAZ^{1,*}, Turgay ÖZMEN², Tahir ÇAKIR³

on the last page

¹Department of Physics, Faculty of Science, Yuzuncu Yil University 65080, Van, Turkey,

²Institute of Sciences, Yuzuncu Yil University, 65080, Van, Turkey..

³Department of Biophysics, Faculty of Medical, Yuzuncu Yil University, 65080, Van, Turkey

Received: 17 October 2019; Revised: 11 November 2019; Accepted: 13 November 2019

*Corresponding author e-mail: ryilmaz@yyu.edu.tr

Citation: Yılmaz, R.; Özmen, T.; Çakır, T. *Int. J. Chem. Technol.* 2019, 3 (2), 101-112.

ABSTRACT

In this study, L X-ray fluorescence (XRF) cross-sections of elements with atomic number $41 \leq Z \leq 49$ were theoretically calculated according to different excitation energies. Also, the Coster-Kronig (CK) enhancement factors observed as a result of the effect of non-irradiated Coster-Kronig transitions on L X-ray fluorescence cross-sections were theoretically calculated at different excitation energies. The change of both L XRF fluorescence cross-sections and the Coster-Kronig enhancement factors against energy were examined. The results obtained were compared with the values in the literature.

Keywords: X-ray fluorescence cross-sections, Coster-Kronig enhancement factors, cross-sections.

Atom numarası $41 \leq Z \leq 49$ arasındaki elementlerin farklı uyarma enerjilerinde Coster-Kronig şiddetlendirme faktörlerinin değişimi

ÖZ

Bu çalışmada, atom numarası $41 \leq Z \leq 49$ arasındaki elementlerin L X-ışını floresans tesir kesitleri, farklı uyarma enerjilerine göre teorik olarak hesaplanmıştır. Ayrıca, ışımsız Coster-Kronig geçişlerinin L X ışını floresans tesir kesitleri üzerindeki etkisinin sonucu olarak gözlenen Coster-Kronig şiddetlendirme faktörleri, farklı uyarma enerjilerinde teorik olarak hesaplandı. Hem L X- ışını floresans kesitlerinin hem de Coster-Kronig şiddetlendirme faktörlerinin enerjiye karşı değişimi incelendi. Elde edilen sonuçlar literatürdeki değerler ile mukayese edildi.

Anahtar Kelimeler: X-ışını floresans tesir kesitleri, Coster-Kronig şiddetlendirme faktörleri, tesir kesitleri.

1. INTRODUCTION

X-ray fluorescence (XRF) cross-sections are of great importance with the extensive use in the fields of molecular, atomic, and radiation physics. Besides, in photon-matter mutual effects of some materials, XRF cross-sections have wide research fields. Especially, the usage of some substances in the field of medicine increases the importance of this work.

XRF cross-sections are identified as the result of photoelectric cross-sections and fluorescence yields at appropriate excitation energy. However, in the case of the

L shell, particularly the L_3 subshell X-ray lines, the estimation of XRF cross-sections is not so straight forward because of the possibility of Coster-Kronig (CK) transitions. These transitions are non-radiative transitions. These transitions from L_1 and L_2 to L_3 lead to an additional gap in the L_3 subshell. The number of X-rays is generated as a result of this increases.¹ Rani and co-workers have reported the effect of CK enhancement factor on the XRF cross-sections.² There are many researchers who have examined XRF cross-sections, CK transitions; fluorescence yields for some elements.³⁻¹³

In recent years, Kumar and co-workers have investigated the Sm element at different energies of 6.8, 7.4 and 8 keV.¹⁴ Öz and co-workers did the same work for some elements in between $Z = 66$ and $Z = 90$.^{15,16} Previously, we have also done experimental and theoretical studies on this topic for Yb, Lu, Os and Pt.¹⁷

This study presents originality because of the investigation of the change of XRF cross sections and CK enhancement factors at different excitation energies of same elements in the atomic number range $41 \leq Z \leq 49$. Herein, firstly, L-XRF cross-sections have been calculated. Secondly, theoretical enhancement factors have been calculated from the obtained values. Excitation energies have been chosen according to the binding energies of electrons.

2. THEORETICAL CALCULATIONS

In this study, the L XRF cross-sections are calculated from the following equations.¹⁵

$$\sigma_{L\ell} = [\sigma_1(f_{13} + f_{12}f_{23}) + \sigma_2f_{23} + \sigma_3]\omega_3F_{3\ell} \quad (1)$$

$$\sigma_{L\alpha} = [\sigma_1(f_{13} + f_{12}f_{23}) + \sigma_2f_{23} + \sigma_3]\omega_3F_{3\alpha} \quad (2)$$

$$\sigma_{L\beta} = \sigma_1\omega_1F_{1\beta} + (\sigma_1f_{12} + \sigma_2)\omega_2F_{2\beta} + [\sigma_3 + \sigma_2f_{23} + \sigma_1(f_{13} + f_{12}f_{23})]\omega_3F_{3\beta} \quad (3)$$

Where, σ_1, σ_2 and σ_3 are photo ionization cross-sections determined from the work of Scofield¹⁹ at proper energies. ω_1, ω_2 and ω_3 are fluorescence yields of subshell. f_{12}, f_{13} and f_{23} are the CK transition probabilities. Fluorescence yield and CK transition probabilities were obtained from the work of Krause.²¹ F_{ij} ($F_{3\alpha}, F_{3\ell}, F_{3\beta}, F_{2\beta}, F_{1\beta}$) are the fractions of the radiation width of the subshell L_i ($i = 1, 2$ and 3). The F_{ij} values are given in Table 1.

$$F_{ij} = \frac{\Gamma_{ij}}{\Gamma} \quad \text{e.g.} \quad F_{3\ell} = \frac{\Gamma_{3\ell}}{\Gamma} \quad (4)$$

Where, Γ is theoretically the total radiative transition rate of the L_3 . $\Gamma_{3\alpha}$ is the sum of the radiative transition rates associated with filling the gaps in the L_3 shell. That is;

$$\Gamma_{3\ell} = \Gamma_3(M_1 - L_3) \quad (5)$$

$$\Gamma_{3\alpha} = \Gamma_3(M_4 - L_3) + \Gamma_3(M_5 - L_3) \quad (6)$$

$$\Gamma_{3\beta} = \Gamma_3(N_1 - L_3) + \Gamma_3(N_4 - L_3) + \Gamma_4(N_5 - L_3) + \Gamma_3(O_1 - L_3) + \Gamma_3(O_4, O_5 - L_3) \quad (7)$$

$$\Gamma_{2\beta} = \Gamma_2(M_4 - L_2) + \Gamma_2(M_3 - L_2) \quad (8)$$

$$\Gamma_{1\beta} = \Gamma_1(M_2, M_3 - L_1) + \Gamma_1(M_4, M_5 - L_1) \quad (9)$$

Scofield calculated the radiative transition rates - Slater theory for most elements.^{18,20} In the absence of the CK transitions, the cross sections can be calculated from the following equations.¹⁵

$$\sigma_{L\ell} = \sigma_3\omega_3F_{3\ell} \quad (10)$$

$$\sigma_{L\alpha} = \sigma_3\omega_3F_{3\alpha} \quad (11)$$

$$\sigma_{L\beta} = \sigma_1\omega_1F_{1\beta} + \sigma_2\omega_2F_{2\beta} + \sigma_3\omega_3F_{3\beta} \quad (12)$$

Because the CK transitions exist, L XRF were evaluated according to Equations 1-3. The CK enhancement factors κ_{ij} ($i = \ell, \alpha; j = 1, 2$) can be calculated from the following equations.^{15,16}

$$\kappa_{(i,j)} = \frac{\sigma_1(f_{13} + f_{12}f_{23}) + \sigma_2f_{23} + \sigma_3}{\sigma_3} \quad (13)$$

$$\kappa_{\beta} = \frac{\sigma_1\omega_1F_{1\beta} + (\sigma_1f_{12} + \sigma_2)\omega_2F_{2\beta}}{\sigma_1\omega_1F_{1\beta} + \sigma_2\omega_2F_{2\beta} + \sigma_3\omega_3F_{3\beta}} \quad (14)$$

$$+ \frac{[\sigma_3 + \sigma_2f_{23} + \sigma_1(f_{13} + f_{12}f_{23})]\omega_3F_{3\beta}}{\sigma_1\omega_1F_{1\beta} + \sigma_2\omega_2F_{2\beta} + \sigma_3\omega_3F_{3\beta}}$$

In this study, the theoretical values of L XRF cross-sections (Table 2-5), and enhancement factors (Tables 9 and 10) were calculated for close excitation energy to absorption edge energy of the studied elements. Also, the theoretical values of L XRF cross-sections (Table 6-8), and enhancement factors (Tables 11 and 12) were calculated for the greater excitation energy from the absorption edge energy of the same elements.

3. RESULTS AND DISCUSSION

The L subshell X-ray fluorescence cross-sections have been calculated from Equations (1-3) for close excitation energy to absorption edge energy and the greater from the absorption edge energy of studied elements (Table 2-8). The enhancement factors have been calculated theoretically from Equations (13) and (14), and listed in Tables 9-12.

Table 1. Theoretically calculated fractions of the radiation width

Element	Fraction of radiative widths				
	$F_{3\ell}$	$F_{3\alpha}$	$F_{1\beta}$	$F_{2\beta}$	$F_{3\beta}$
⁴¹ Nb	0.035	0.934	0.862	0.941	0.028
⁴² Mo	0.035	0.926	0.857	0.877	0.029
⁴³ Tc	0.034	0.918	0.853	0.924	0.044
⁴⁴ Ru	0.034	0.918	0.850	0.914	0.056
⁴⁵ Rh	0.033	0.899	0.847	0.905	0.066
⁴⁶ Pd	0.033	0.888	0.845	0.893	0.078
⁴⁷ Ag	0.032	0.880	0.841	0.885	0.087
⁴⁸ Cd	0.032	0.871	0.837	0.877	0.094
⁴⁹ In	0.032	0.865	0.832	0.839	0.101

Table 2. L_3 XRF cross-sections (barns/atom) for $41 \leq Z \leq 49$

Element	E (keV)	$\sigma_{L\alpha}$	$\sigma_{L\beta}$	$\sigma_{L\ell}$
⁴¹ Nb	2.386	7625.568	228.603	285.754
⁴² Mo	2.539	7631.860	239.010	288.461
⁴³ Tc	2.696	7594.797	364.020	281.288
⁴⁴ Ru	2.858	7592.429	463.154	281.201
⁴⁵ Rh	3.025	7406.914	543.777	271.888
⁴⁶ Pd	3.193	7179.044	630.591	266.788
⁴⁷ Ag	3.373	7143.136	706.196	252.413
⁴⁸ Cd	3.560	7152.512	769.280	269.992
⁴⁹ In	3.754	6961.347	812.827	257.528

Table 3. L_3 XRF cross-sections (barns/atom) according to the excitation energies of L_2 and L_1 for $41 \leq Z \leq 49$ (for close excitation energy to absorption edge energy)

Element	E(keV)	$\sigma_{L\alpha}$	$\sigma_{L\beta}$	σ_{L1}
^{41}Nb	2.674	5697.343	2839.378	213.497
	3.000	4188.616	2456.635	157.044
^{42}Mo	2.648	6744.817	3342.646	254.933
	3.000	5020.601	2827.232	187.736
^{43}Tc	2.818	6700.373	3683.536	248.159
	4.000	2640.682	1716.435	097.803
^{44}Ru	2.993	6690.843	3747.400	247.911
	4.000	3113.195	2058.982	115.303
^{45}Rh	3.174	6526.900	3714.000	239.585
	4.000	3570.090	2428.620	131.048
^{46}Pd	3.356	6429.333	3843.551	238.830
	4.000	4100.701	2888.952	152.389
^{47}Ag	3.553	6292.457	3954.592	222.353
	4.000	4683.993	3396.644	165.516
^{48}Cd	3.757	6966.109	4052.371	236.747
	4.022	5295.610	3918.681	200.637
^{49}In	3.970	6194.265	3941.396	229.152
	4.244	5265.774	3925.979	194.688

Table 4. L_2 XRF cross-sections (barns/atom) for $41 \leq Z \leq 49$ (for close excitation energy to absorption edge energy)

Element	E(keV)	$\sigma_{L\alpha}$	$\sigma_{L\beta}$	σ_{L1}
^{41}Nb	2.674	6108.629	2851.708	228.886
^{42}Mo	2.648	7257.042	3388.869	274.294
^{43}Tc	2.818	7220.373	3708.668	267.266
^{44}Ru	2.993	7224.441	3779.950	267.495
^{45}Rh	3.174	7053.793	3822.853	258.752
^{46}Pd	3.356	6942.178	3885.831	257.212
^{47}Ag	3.553	6809.397	4005.698	281.943
^{48}Cd	3.757	6768.870	4108.506	256.397
^{49}In	3.970	6706.630	4241.221	248.106

Table 5. L_I XRF cross-sections (barns/atom) for $41 \leq Z \leq 49$ (for close excitation energy to absorption edge energy)

Element	E(keV)	$\sigma_{L\alpha}$	$\sigma_{L\beta}$	σ_{L_I}
⁴¹ Nb	3.000	5316.673	2607.498	199.289
⁴² Mo	3.000	6244.808	3021.255	233.355
⁴³ Tc	4.000	6223.393	3708.668	128.708
⁴⁴ Ru	4.000	4070.968	2222.024	150.701
⁴⁵ Rh	4.000	4620.362	2621.057	169.577
⁴⁶ Pd	4.000	5260.494	3117.180	195.211
⁴⁷ Ag	4.000	5940.055	3662.148	179.088
⁴⁸ Cd	4.022	6659.311	4060.067	252.200
⁴⁹ In	4.244	6653.893	4001.221	246.155

Table 6. L_3 XRF cross-sections (barns/atom) according to the excitation energies of L_2 and L_I for $41 \leq Z \leq 49$ (for the greater excitation energy from the absorption edge energy)

Element	E(keV)	$\sigma_{L\alpha}$	$\sigma_{L\beta}$	σ_{L_I}
⁴¹ Nb	2.695	5583.339	2787.361	209.225
	4.000	1894.626	1164.554	070.997
⁴² Mo	2.844	5706.678	2796.619	215.695
	4.000	2252.623	1273.443	085.142
⁴³ Tc	3.000	5782.665	3126.733	214.172
	5.000	1408.542	0965.655	052.168
⁴⁴ Ru	3.201	5708.729	3156.636	211.434
	5.000	1663.671	1152.588	061.617
⁴⁵ Rh	3.388	5586.511	3211.117	205.066
	5.000	1913.325	1359.586	070.233
⁴⁶ Pd	3.605	5408.541	3392.380	201.222
	5.000	2200.314	1613.727	081.768
⁴⁷ Ag	3.780	5422.560	3407.000	197.184
	5.000	2511.400	1921.502	091.270
⁴⁸ Cd	4.000	5370.237	3493.566	203.464
	5.000	2919.386	2264.099	110.600
⁴⁹ In	4.000	6082.060	3991.672	225.004
	6.000	2019.948	1639.340	074.726

Table 7. L_2 XRF cross-sections (barns/atom) for $41 \leq Z \leq 49$ (for the greater excitation energy from the absorption edge energy)

Element	E(keV)	$\sigma_{L\alpha}$	$\sigma_{L\beta}$	σ_{Ll}
⁴¹ Nb	2.695	5887.238	2799.469	224.289
⁴² Mo	2.844	6130.816	2809.902	232.519
⁴³ Tc	3.000	6223.393	3147.858	230.449
⁴⁴ Ru	3.201	6157.500	3184.012	228.137
⁴⁵ Rh	3.388	6032.992	3243.895	221.266
⁴⁶ Pd	3.605	5846.604	3430.553	217.010
⁴⁷ Ag	3.780	5867.911	3451.123	213.353
⁴⁸ Cd	4.000	5818.940	3542.788	220.351
⁴⁹ In	4.000	6598.061	4040.626	244.262

Table 8. L_l XRF cross-sections (barns/atom) for $41 \leq Z \leq 49$ (for the greater excitation energy from the absorption edge energy)

Element	E(keV)	$\sigma_{L\alpha}$	$\sigma_{L\beta}$	σ_{Ll}
⁴¹ Nb	4.000	2533.348	1268.200	094.924
⁴² Mo	4.000	2985.482	1384.233	112.813
⁴³ Tc	5.000	1942.690	1054.580	071.940
⁴⁴ Ru	5.000	2273.575	1259.831	084.169
⁴⁵ Rh	5.000	2579.149	1485.808	094.604
⁴⁶ Pd	5.000	2940.096	1766.050	104.826
⁴⁷ Ag	5.000	3325.721	2098.281	120.842
⁴⁸ Cd	5.000	3838.101	2453.548	145.329
⁴⁹ In	6.000	2726.847	1813.878	100.877

Table 9. $\kappa_{l1} - \kappa_{\alpha 1}$; $\kappa_{l2} - \kappa_{\alpha 2}$ CK enhancement factors for $41 \leq Z \leq 49$ (for close excitation energy to absorption edge energy)

Element	E(keV) (for L ₂)	$\kappa_{\alpha 1} - \kappa_{l1}$	E(keV) (for L ₁)	$\kappa_{\alpha 2} - \kappa_{l2}$
⁴¹ Nb	2.674	1.072	3.000	1.269
⁴² Mo	2.648	1.075	3.000	1.243
⁴³ Tc	2.818	1.077	4.000	1.316
⁴⁴ Ru	2.993	1.079	4.000	1.307
⁴⁵ Rh	3.174	1.080	4.000	1.294
⁴⁶ Pd	3.356	1.079	4.000	1.282
⁴⁷ Ag	3.553	1.082	4.000	1.268
⁴⁸ Cd	3.757	1.083	4.022	1.257
⁴⁹ In	3.970	1.082	4.244	1.263

Table 10. $\kappa_{\beta 1}$, $\kappa_{\beta 2}$ CK enhancement factors for $41 \leq Z \leq 49$ (for close excitation energy to absorption edge energy)

Element	E(keV) (for L ₂)	$\kappa_{\beta 1}$	E(keV) (for L ₁)	$\kappa_{\beta 2}$
⁴¹ Nb	2.674	1.004	3.000	1.061
⁴² Mo	2.648	1.013	3.000	1.068
⁴³ Tc	2.818	1.007	4.000	1.080
⁴⁴ Ru	2.993	1.008	4.000	1.081
⁴⁵ Rh	3.174	1.020	4.000	1.079
⁴⁶ Pd	3.356	1.011	4.000	1.079
⁴⁷ Ag	3.553	1.012	4.000	1.078
⁴⁸ Cd	3.757	1.013	4.022	1.076
⁴⁹ In	3.970	1.019	4.244	1.076

Table 11. $\mathcal{K}_{l1} - \mathcal{K}_{\alpha 1}$; $\mathcal{K}_{l2} - \mathcal{K}_{\alpha 2}$ CK enhancement factors for $41 \leq Z \leq 49$ (for the greater excitation energy from the absorption edge energy)

Element	E(keV) (for L ₂)	$\mathcal{K}_{\alpha 1} - \mathcal{K}_{l1}$	E(keV) (for L ₁)	$\mathcal{K}_{\alpha 2} - \mathcal{K}_{l2}$
⁴¹ Nb	2.695	1.072	4.000	1.337
⁴² Mo	2.844	1.078	4.000	1.325
⁴³ Tc	3.000	1.076	5.000	1.379
⁴⁴ Ru	3.201	1.079	5.000	1.366
⁴⁵ Rh	3.388	1.079	5.000	1.347
⁴⁶ Pd	3.605	1.080	5.000	1.336
⁴⁷ Ag	3.780	1.082	5.000	1.324
⁴⁸ Cd	4.000	1.083	5.000	1.314
⁴⁹ In	4.000	1.085	6.000	1.349

Table 12. $\mathcal{K}_{\beta 1}$, $\mathcal{K}_{\beta 2}$ CK enhancement factors for $41 \leq Z \leq 49$ (for the greater excitation energy from the absorption edge energy)

Element	E(keV) (for L ₂)	$\mathcal{K}_{\beta 1}$	E(keV) (for L ₁)	$\mathcal{K}_{\beta 2}$
⁴¹ Nb	2.695	1.004	4.000	1.132
⁴² Mo	2.844	1.005	4.000	1.087
⁴³ Tc	3.000	1.006	5.000	1.091
⁴⁴ Ru	3.201	1.008	5.000	1.093
⁴⁵ Rh	3.388	1.010	5.000	1.092
⁴⁶ Pd	3.605	1.011	5.000	1.094
⁴⁷ Ag	3.780	1.012	5.000	1.092
⁴⁸ Cd	4.000	1.014	5.000	1.084
⁴⁹ In	4.000	1.012	6.000	1.106

The graphs of enhancing factors versus atomic number are shown in Figures 1-4. In this study, the results were theoretically until 8.3% for $\mathcal{K}_{\alpha 1}$, until 31.6% for $\mathcal{K}_{\alpha 2}$,

until 8.3% for \mathcal{K}_{l1} , until 31.6% for \mathcal{K}_{l2} , until 1.9% for $\mathcal{K}_{\beta 1}$, until 8% for $\mathcal{K}_{\beta 2}$, for close excitation energy to absorption edge energy.

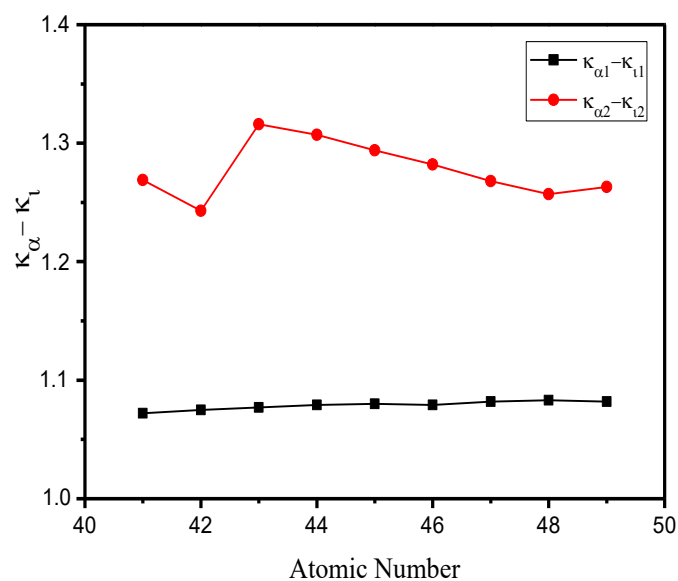


Figure 1. $K_{\alpha 1}$, $K_{\alpha 2}$, K_{l1} , K_{l2} versus atomic number (for close excitation energy to absorption edge energy).

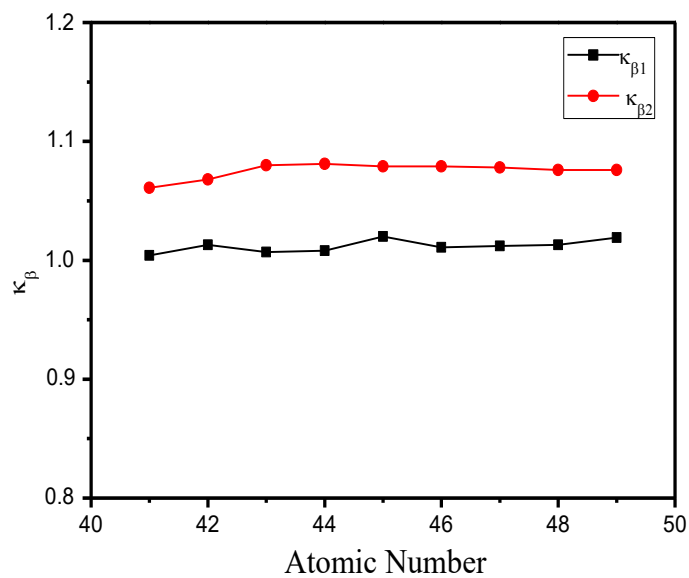


Figure 2. $K_{\beta 1}$, $K_{\beta 2}$ versus atomic number (for close excitation energy to absorption edge energy)

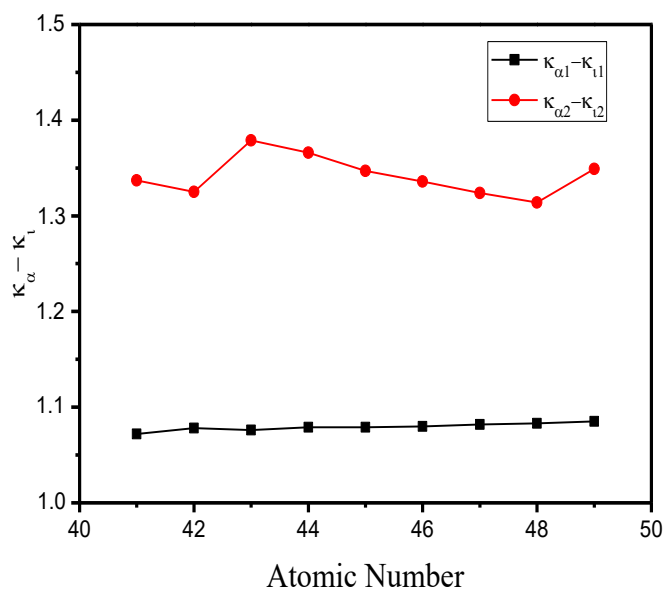


Figure 3. $K_{\alpha 1}$, $K_{\alpha 2}$, K_{l1} , K_{l2} versus atomic number (for the greater excitation energy from the absorption edge energy).

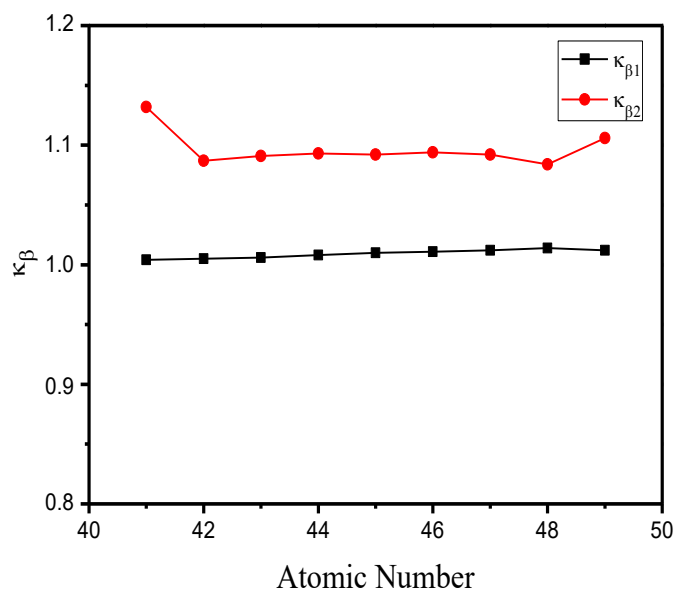


Figure 4. $K_{\beta 1}$, $K_{\beta 2}$ versus atomic number (for the greater excitation energy from the absorption edge energy).

Also, for the greater excitation energy from the absorption edge energy, in the present work, the results were theoretically until 8.5% for $\kappa_{\alpha 1}$, 37.9% for $\kappa_{\alpha 2}$ up to 8.5% for of $\kappa_{\ell 1}$ and up to 37.9% for $\kappa_{\ell 2}$, until 1.4% for $\kappa_{\beta 1}$, until 10.6% for $\kappa_{\beta 2}$.

As seen above, both *L* XRF cross-sections and CK enhancement factor values have been found to vary according to different excitation energies. *L* XRF cross-section values decrease, for the greater excitation energy from the absorption edge energy. However, CK enhancement factors increase. This means that it has increased due to gaps caused by CK transitions. In general, *L* X-ray cross-section values were found to be more efficient in close excitation energy the absorption side.

Rani and co-workers² reported that the effect of on X-ray cross-sections and the CK transitions is up to 65%, experimentally up to 24% for Sb element, theoretically up to 21%. Öz and co-workers reported theoretically up to 30%, experimentally up to 24% for some elements in the atomic number range 66-90.^{15,16}

As can be seen from this study, due to CK transitions, there is an enhancement up to 2-38%. Also, it appears that the X-ray fluorescence cross-sections decrease despite increasing CK enhancement factors for the greater excitation energy from the absorption edge energy. Therefore, the compatibility of the excitation energy and the binding energy is important for efficiency. Thus, it must be taken into account in quantitative X-ray fluorescence cross-sections.

4. CONCLUSIONS

In the present study, the CK enhancement factors due to the effect of CK transitions on *L* XRF cross sections are studied theoretically at different excitation energies. The results of the study can be summarized as follows.

- When the excitation energy is greater than the bonding energy of the electron, XRF cross-sections values decrease, but CK enhancement factors increase.
- When the excitation energy is close to bonding energy of the electron, CK enhancement factors increase but, XRF cross-sections values decrease.

Conflict of interest

Author declares that there is no a conflict of interest with any person, institute, company, etc.

REFERENCES

1. Labar, J. L. *X-ray Spectrom.* **1991**, 20, 111-117.
2. Rani, A.; Nath, N.; Chaturvedi, S. N. *X-ray Spectrom.* **1989**, 18, 77-80.
3. Ertuğrul, M. *J. Elect. Spectrosc. Relat. Phenom.* **2002a**, 125, 69-73.
4. Ertuğrul, M. *Appl. Radiat. Isot.* **2002b**, 57, 63-66.
5. Ertuğrul, M. *J. Quant. Spectrosc. Radiat. Transfer.* **2002c**, 72, 567-574.
6. Tıraşoğlu, E.; Çevik, U.; Ertuğrul, B.; Atalay, Y.; Kopya, A.İ. *Rad. Phys. and Chem.* **2001**, 60 (1-2), 11-16.
7. Han, I; Demir, L.; Ağbaba, M. *Radiat. Phys. And Chem.* **2007**, 76, 1551-1559.
8. Kaya, A.; Ertuğrul, M.; Doğan, O.; Söğüt, Ö.; Turgut, Ü.; Şimşek, Ö. *Anal. Chemica Acta*, **2001**, 441, 317-323.
9. Öz, E.; Özdemir, Y.; Ekinçi, N.; Ertuğrul, M.; Şahin, Y.; Erdoğan, H. *Spec. Acta B*, **2000**, 55, 1869-1877.
10. Öz, E.; Ekinçi, N.; Özdemir, Y.; Ertuğrul, M.; Şahin, Y.; Erdoğan, H. *J. Phys. B: At. Mol. Opt. Phys.* **2001**, 34, 631-638.
11. Puri, S.; Singh, N. *Radiat. Phys. Chem.* **2006**, 75, 2232-2238.
12. Söğüt, Ö.; Büyükkasap, E.; Ertuğrul, M.; Küçükönder, A. *J. Quant. Spectros. Radiat. Trans.* **2002**, 74, 395-400.
13. Hallak, A. B. *Radiat. Phys. Chem.* **2001**, 60, 17-21.
14. Kumar, R.; Rani A.; Singh, R. M.; Tivari M. K.; Singh, A. K., *J. Elect. Spectrosc. Rel. Phen.* **2016**, 209, 34-39.
15. Öz, E.; Ekinçi, N.; Ertuğrul, M.; Şahin, Y. *X-ray Spectrom.* **2003**, 32, 153-157.
16. Öz, E.; Şahin, Y; Ertuğrul, M.; *Radiat. Phys. Chem.* **2004**, 69, 17-21.
17. Yılmaz, R; Öz, E.; Tan, M.; Durak, R.; Demirel, A. İ.; Şahin, Y. *Radiat. Phys. Chem.* **2009**, 78, 318-322.

DOI: <http://dx.doi.org/10.32571/ijct.634210>

E-ISSN:2602-277X

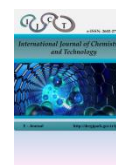
18. Scofield, J. H. *Phys. Rev. A*, **1969**, 179, 9-16.
19. Scofield, J.H. *Report UCRL Report 51326. Lawrence Livermore Laboratory Report, California*, 1973.
20. Scofield, J. H. *Atom. Data Nucl. Data Tables*. **1974**, 14, 121-137.
21. Krause, M. O. *J. Phys. Chem. Ref. Data*. **1979**, 8, 307-327.

ORCID

 <https://orcid.org/0000-0003-2734-8763> (R. Yılmaz)

 <https://orcid.org/0000-0002-4302-6898> (T. Özmen)

 <https://orcid.org/0000-0003-0080-6605> (T. Çakır)



Cytotoxic activity of zinc oxide/titanium dioxide nanoparticles on prostate cancer cells

Ayca TAS^{1,*}, Nese KEKLIKCIOGLU CAKMAK², Tugba AGBEKTAS³, Yavuz SILIG³

on the last page

¹Department of Nutrition and Dietetics, Faculty of Health Sciences, Sivas Cumhuriyet University, Turkey

²Department of Chemical Engineering, Faculty of Engineering, Sivas Cumhuriyet University, Turkey

³Department of Biochemistry Faculty of Medicine, Sivas Cumhuriyet University, Turkey

Received: 31 August 2019; Revised: 12 October 2019; Accepted: 15 October 2019

*Corresponding author e-mail: aycatas@cumhuriyet.edu.tr

Citation: Tas, A.; Keklikcioglu Cakmak, N.; Agbektas, T.; Silig, Y. *Int. J. Chem. Technol.* 2019, 3 (2), 113-120.

ABSTRACT

Prostate cancer is caused by uncontrolled growth of cells in the prostate gland. The aim of this study was to determine the cytotoxic activity of titanium dioxide (TiO₂) and zinc oxide (ZnO) nanoparticles (NPs) and TiO₂ + ZnO nanocomposite (NC) in human prostate cancer cell line (DU-145) and healthy mouse fibroblast cell line (L-929). In the study, TiO₂ and ZnO NPs and TiO₂ + ZnO NC were synthesized. Cytotoxic activities of NC and NPs was then analyzed in human prostate cancer cell line (DU-145) and healthy mouse fibroblast cell lines (L-929) using the MTT method. TiO₂, ZnO and TiO₂ + ZnO IC₅₀ values were determined in DU-145 and L-929 cell cells (n = 6). TiO₂ + ZnO NC in the Du-145 cell line was found as the most active, having statistically significant (**p < 0.0001, **p < 0.001 and **p < 0.01).

Keywords: Prostate cancer, Du-145, L-929, TiO₂/ZnO.

Çinko oksit/titanyum dioksit nanopartiküllerinin prostat kanser hücreleri üzerinde sitotoksik aktivitesi

ÖZ

Prostat kanseri, prostat bezindeki hücrelerin kontrolsüz büyümesinden kaynaklanır. Bu çalışmanın amacı, insan prostat kanseri hücre hattında (DU-145) ve sağlıklı fare fibroblast hücre hattında (L-929) titanyum dioksit (TiO₂) ve çinko oksit (ZnO) nanopartikülleri (NPs) ve TiO₂ + ZnO nanokompozit (NK) 'in sitotoksik aktivitesini belirlemektir. Çalışmada TiO₂ ve ZnO NPs ve TiO₂+ZnO NK sentezlenmiştir. NK ve NPs'lerin sitotoksik aktiviteleri, daha sonra MTT metodu kullanılarak insan prostat kanser hücre hattı (DU-145) ve sağlıklı mouse fibroblast hücre hatlarında (L-929) analiz edilmiştir. DU-145 ve L-929 hücrelerinde TiO₂, ZnO ve TiO₂+ZnO IC₅₀ değerleri belirlenmiştir (n = 6). Du-145 hücre hattında TiO₂ + ZnO NK, istatistiksel öneme sahip olarak en aktif olarak bulunmuştur (**p < 0.0001, **p < 0.001 ve **p < 0.01).

Anahtar Kelimeler: Prostat kanseri, Du-145, L-929, TiO₂/ZnO.

1. INTRODUCTION

Cancer is a serious health problem and it is one causes of deaths in the world.¹ Prostate cancer is the second most common type of cancer in men after lung cancer and is the fifth most common type of cancer worldwide.² The onset of prostate cancer is characterized by a relatively slow growth, low rate of progression, high incidence rate, presence of tumor markers, and detectable

preneoplastic lesions.³ Surgery is often successful for organ-limited prostate cancer. However, most prostate cancer patients after few years of treatment developed tumor regeneration and shorten their survival when tumor recurrence.⁴ One of methods that use in treatment of prostate cancer is chemotherapeutic drugs. Etoposide, paclitaxel, vinblastine, mitoxantrone and estramustine some drugs like; can use in chemotherapy. However, these chemotherapeutic drugs have many side effects

DOI: <http://dx.doi.org/10.32571/ijct.613536>

E-ISSN:2602-277X

such as toxic, deaths, paralysis, blood clotting, leukocyte decline, difficulty breathing and fatigue. Therefore, in the prolonged treatment of prostate cancer, the discovery of new anti-cancer compounds is important to improve quality of life and to eliminate these side effects. The aim of anticancer drug development studies is to discover artificial and natural compounds that can be used in cancer treatment, as well as to reduce toxicity and maximize efficacy. In recent years, scientists have focused on the field of nanotechnology, which has made significant progress in developing pharmaceuticals for cancer treatment. Nanoparticles (NPs) are used as drug carriers that target the drug directly to the tumor area and in the same time maintaining healthy tissue. Compared to conventional chemotherapeutic drugs, nano-carriers have many advantages and offer various advantages as drug carriers.^{5,6} Various inorganic NPs such as iron oxide, porous silica, graphene oxide and TiO₂ NPs have been used for successful drug delivery and treatment in cancer treatment.⁷ TiO₂ and ZnO have many important properties. Some of these properties are biocompatibility, low toxicity, high chemical stability and specific photocatalytic and sonocatalytic. Therefore, even in the field of potential multimodal treatment agents, photodynamic and sonodynamic therapy methods used in the treatment of cancer have received great interest.⁸ TiO₂ can produce highly reactive radical oxygen species under ultraviolet (UV) light irradiation and cause cancer cell death.⁹ Based on its unique properties, TiO₂ NPs also play an important role in the drug delivery field of drugs used in the chemotherapeutic treatment.¹⁰ ZnO is a semiconductor material which has gained considerable scientific interest due to its wide range of applications such as biomedical, optical, electronic and optoelectronics.¹¹ ZnO NPs offer biocompatibility advantages for use in biomedical applications where nanomaterials prepared using high colloidal dispersion in water and toxic chemicals are unsuitable.¹² In this study, we prepared a complex of TiO₂ + ZnO, and evaluated the cytotoxicity activity properties of this complex in human Du-145 and mouse L-929 cell lines.

2. MATERIALS AND METHODS

2.1. Synthesis of TiO₂, ZnO NPs and TiO₂ + ZnO nanocomposite (NC)

TiO₂, ZnO NPs and TiO₂ + ZnO NC were prepared as in our previous study.¹³ In a typical synthesis step to prepare zinc oxide NPs, zinc nitrate hexahydrate and ascorbic acid were dissolved in distilled water at 1:0.3 molar ratios and heated on a hot plate at 300°C until a brown precipitate formed. The precipitate was crushed finely and calcined at 400°C.¹⁴ The resulting powder was

white and consisted of ZnO NPs. TiO₂ NPs were prepared using a similar process using titanium isopropoxide and glycine as the precursors.¹⁵ To prepare NC, a suspension with water was prepared in a 1:1 weight ratio from the previously prepared ZnO and TiO₂ particles. The solution was sonicated for 1 h with a probe sonicator to prepare a high stability suspension. Afterwards, solution was heated at 100°C to obtain a dry powder, which is the composite of the samples. All samples were ultrasonicated 60 minutes to break any possible aggregation of NPs in a Probe Sonicator (Sonics & materials INC, USA). Stability of the samples was determined by measuring their zeta potential values (Malvern Zetasizer Nano Z).

2.2 Cell Culture

Du-145 and L-929 cell lines were maintained in DMEM medium containing, 10% fetal bovine serum (FBS), penicillin and streptomycin (1%). Cells were incubated at 37°C, 5% CO₂ and 95 % air in a humidified incubator. For each cell line, 70-80% confluent cell culture flask was trypsinized and cells were seeded in 96 well plates.

2.3. Cytotoxic effect of TiO₂ + ZnO NC on Du-145 and L-929 cell lines

The cytotoxicity activity of TiO₂ and ZnO NPs and TiO₂ + ZnO NC in the Du-145 and L-929 cell lines was performed by MTT 3-(4,5-dimethylthiazol-2-yl)-2,5-diphenyltetrazolium bromide assay according to Skehan's method.¹⁶ The cells were then trypsinized and seeded in 96-well plates (Corning, USA) in 0.1 mL of complete culture medium at a density of 1 x 10⁵ cells per well and allowed to bind for 24 h. 1 µl of test substance at concentrations ranging between 1-100 µM were added into each well containing the cells. The plates were incubated at 37°C with an internal atmosphere of 5% CO₂. After 24, 48 and 72 h incubation, 10 µl/well MTT (5 mg ml⁻¹ dissolved in PBS) was added to the cells in the plates and incubated at 37°C for 2 h. The supernatant was carefully withdrawn from each well and 100 µl of DMSO was added to each well to dissolve formazan crystals. After mixing with a mechanical plate mixer for 15 min, the absorbance of plates were recorded at 570 nm on a microplate reader (Bio-Tek, USA). All these drug doses were tested in parallel in three replicates. Control samples were run with 1% sterilized water.

2.4. Statistical analysis

SPSS (Statistical Package for Social Sciences, ver: 25.0) program was used to evaluate the data in the study.

DOI: <http://dx.doi.org/10.32571/ijct.613536>

E-ISSN:2602-277X

All experiments were run in triplicate and the results expressed as mean \pm SEM. The data were analyzed using one-way ANOVA and differences were considered significant (* $p < 0.05$, ** $p < 0.01$ and *** $p < 0.0001$).

3. RESULTS AND DISCUSSION

3.1. Characterization of TiO₂, ZnO NPs and TiO₂ + ZnO NC

It has been assumed that, under pure electrostatic interaction, a suspension that exhibits a zeta potential within ± 15 mv is considered unstable and tends to aggregate, from ± 15 mv to ± 30 mv it would be predominantly stable, and above ± 40 mv it would be well stabilized.¹⁷ The zeta potential of synthesized NPs are given in Table 1 and are within the acceptable range for stability.

Table 1. Zeta potential of TiO₂, ZnO NPs and TiO₂ + ZnO NC

Nanoparticle	Zeta potential, mV
TiO ₂	33
ZnO	29
TiO ₂ + ZnO	24

3.2. Cytotoxicity activities of TiO₂ + ZnO on DU-145 and L-929 cell lines

Nanotechnology is a new technology that provides new uses for a wide range of biological and biomedical applications. Scientists are directed to this area because the size of the so-called nanoparticle is less than 100 nm.¹⁸ Due to their superior targeting capabilities and efficacy, NPs are becoming increasingly important in modern cancer therapy. It has also begun to outperform traditional cancer treatments such as chemotherapy, radiation and surgery.¹⁹ TiO₂ and ZnO NPs are widely used metal oxide NPs because of their superior biomedical and biological properties.²⁰ ZnO NPs show high biocompatibility. Bulkier forms are generally considered safe by the FDA. Zinc is an important co-factor in many cellular mechanisms. Therefore, it plays an important role in maintaining cellular homeostasis; therefore, ZnO shows biocompatibility.¹² ZnO NPs exhibit selective cytotoxicity to cancer cells in vitro compared to many other NPs.²¹ TiO₂ NPs are environmentally friendly, relatively stable, exhibiting excellent biocompatibility because they are smaller than cellular organelles.²² These properties make TiO₂ NPs an

excellent candidate for biomedical applications such as cancer treatment.²³ In this study, we evaluated the cytotoxic activity of TiO₂ and ZnO and TiO₂+ZnO NC in DU-145 and L-929 cells. The aim of this process is to utilize the synergistic effects of these NPs used in biomedical applications. In our study, Figure 1-3 show changes in cell inhibition for 24, 48 and 72 h versus increasing concentrations of DU-145 cell lines. Compared to the control group (DU-145 cell without test substance), TiO₂ + ZnO treated DU-145 prostate cancer cells showed significantly decreased tumor survival rate after 24 h, 48 h and 72 h of incubation (*** $p < 0.0001$, ** $p < 0.001$ and ** $p < 0.01$). Cell survival rate in group after 24h, 48h and 72 h of incubation were significantly decreased than those in the control group. The survival rate of tumor cells was significantly reduced with TiO₂ + ZnO NC treatment time. TiO₂ + ZnO NC on DU-145 cells were the most active for 72 h of incubation. In addition, TiO₂ + ZnO and IC₅₀ values for 24 h, 48 h and 72 h were 3.78 ± 2.08 μ M, 3.12 ± 0.65 μ M and 1.38 ± 0.79 μ M respectively (Table 2). We also tried to determine the cytotoxic activity of these molecules in the L-929 cells for health control purposes. We have found that these NPs are more active in the L-929 cell line than in the control group (L-929 cell without test substance). IC₅₀ values of TiO₂ + ZnO after 24 h, 48 h and 72 h incubation were 24.44 ± 1.09 μ M, 20.63 ± 1.44 μ M and 19.36 ± 3.04 μ M in L-929 cells, respectively (Table 2).

Table 2. Comparison of IC₅₀ values between TiO₂+ZnO NC, ZnO and TiO₂ NPs on Du-145 and L-929 cells after 24 h, 48 h and 72 h of incubation

	Du-145 cell line IC ₅₀ (μ M \pm SD*)		
	24 h	48 h	72 h
TiO ₂ + ZnO	3.78 \pm 2.08	3.12 \pm 0.65	1.38 \pm 0.79
ZnO	70.14 \pm 3.41	62.19 \pm 2.26	22.43 \pm 5.02
TiO ₂	11.68 \pm 0.69	4.99 \pm 1.08	1.12 \pm 0.16
	L-929 Cell Line IC ₅₀ (μ M \pm SD*)		
	24 h	48 h	72 h
TiO ₂ + ZnO	24.44 \pm 1.09	20.63 \pm 1.44	19.36 \pm 3.04
ZnO	67.27 \pm 2.78	63.56 \pm 3.09	53.63 \pm 1.08
TiO ₂	19.14 \pm 0.87	15.00 \pm 1.13	13.45 \pm 0.25

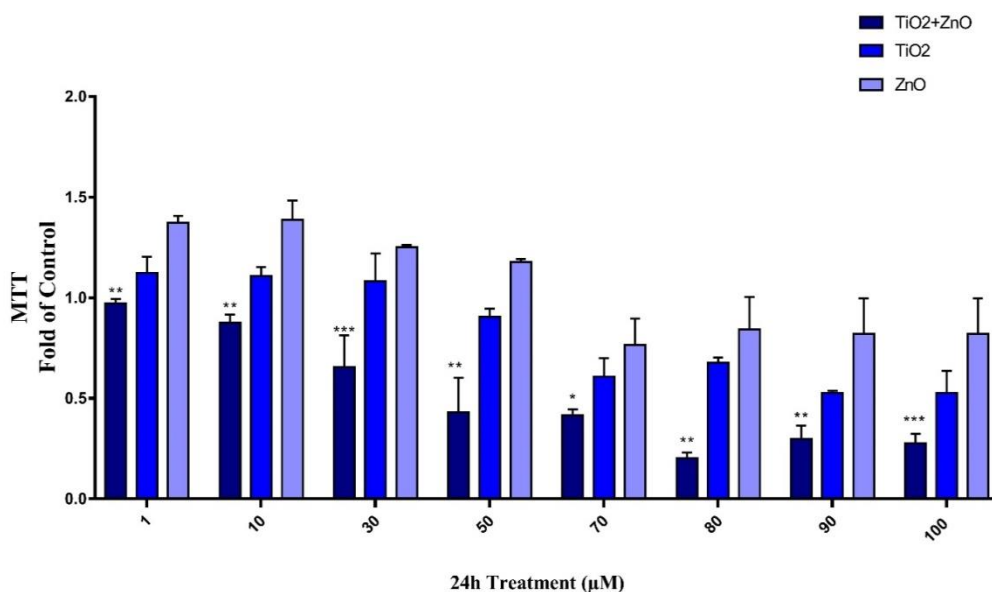


Figure 1. Cytotoxicity activity study of TiO₂ + ZnO, TiO₂ and ZnO in Du-145 cells. Du-145 cells were treated with these molecules for 24 h in a concentration range of 1 to 100. These molecules were compared with control. Represents the mean ± SEM of three separate experiments (***p < 0.0001, **p < 0.001 and *p < 0.01).

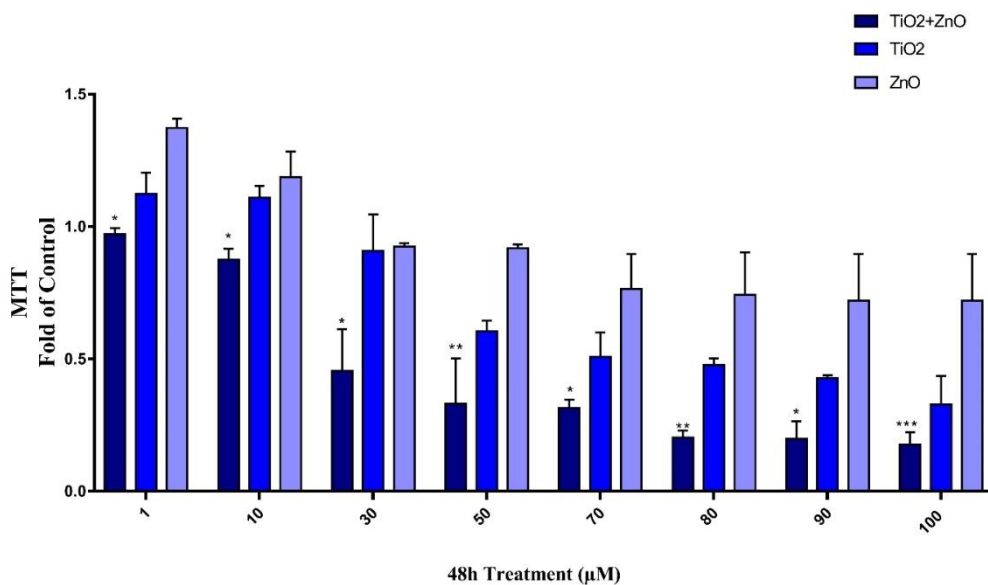


Figure 2. Cytotoxicity activity study of TiO₂ + ZnO, TiO₂ and ZnO in Du-145 cells. Du-145 cells were treated with these molecules for 48 h in a concentration range of 1 to 100. These molecules were compared with control. Represents the mean ± SEM of three separate experiments (***p < 0.0001, **p < 0.001 and *p < 0.01).

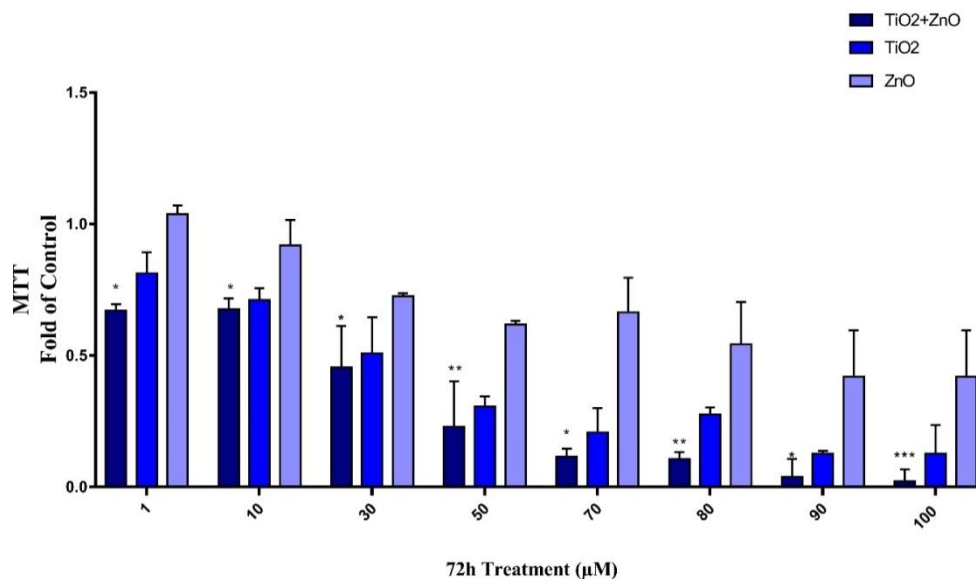


Figure 3. Cytotoxicity activity study of TiO₂ + ZnO, TiO₂ and ZnO in Du-145 cells. Du-145 cells were treated with these molecules for 72 h in a concentration range of 1 to 100. These molecules were compared with control. Represents the mean ± SEM of three separate experiments. (***p < 0.0001, **p < 0.001 and *p < 0.01).

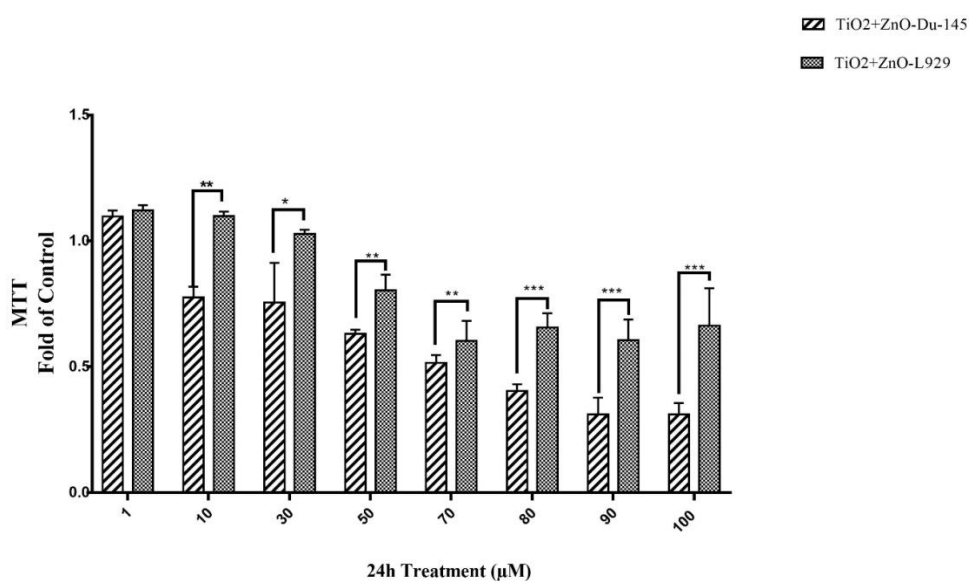


Figure 4. Cytotoxicity study of TiO₂ + ZnO on Du-145 and L-929 cells. Du-145 and L-929 cells were treated with these drugs for 24 h in a concentration range of 1 to 100 TiO₂ + ZnO. TiO₂ + ZnO, which is more active than TiO₂ and ZnO, were compared with Du-145 cells and L-929 cells. Represents the mean ± SEM of three separate experiments (***p < 0.0001, **p < 0.001 and *p < 0.01).

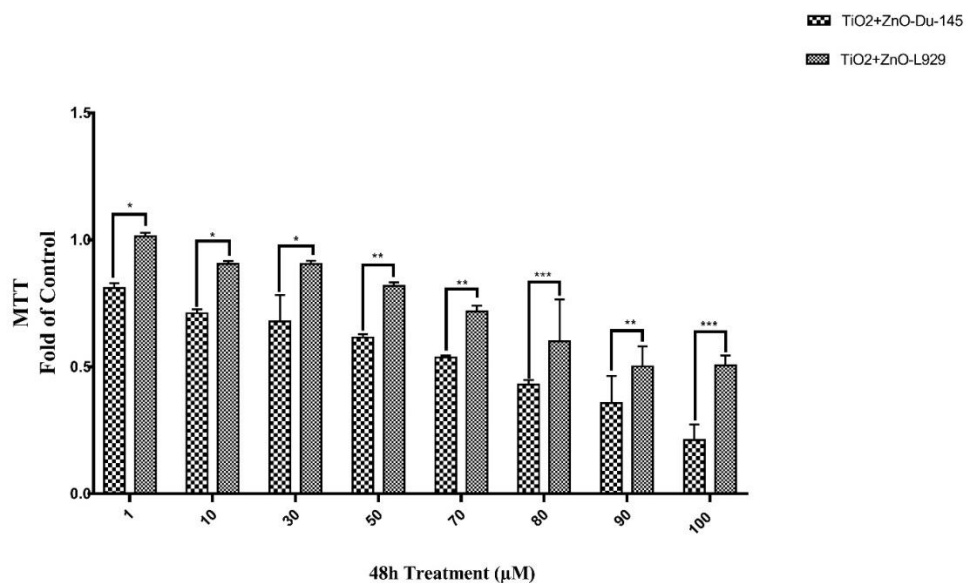


Figure 5. Cytotoxicity study of TiO₂ + ZnO on Du-145 and L929 cells. Du-145 and L-929 cells were treated with these drugs for 48 hours in a concentration range of 1 to 100 TiO₂ + ZnO. TiO₂ + ZnO, which is more active than TiO₂ and ZnO, were compared with Du-145 cells and L-929 cells. Represents the mean ± SEM of three separate experiments (***p < 0.0001 , **p < 0.001 and *p < 0.01).

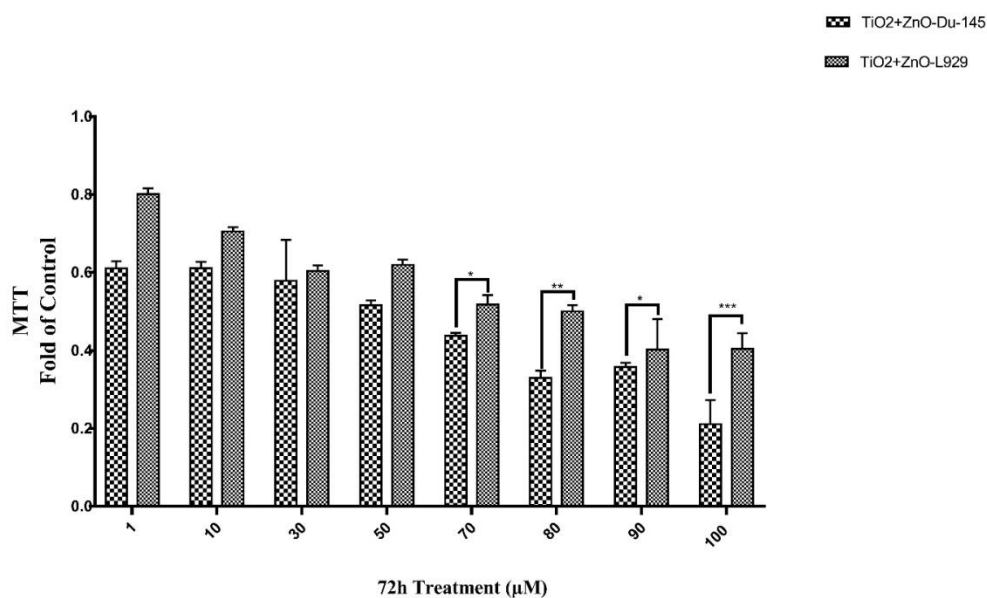


Figure 6. Cytotoxicity study of TiO₂ + ZnO on Du-145 and L-929 cells. Du-145 and L-929 cells were treated with these drugs for 72 h in a concentration range of 1 to 100 TiO₂ + ZnO. TiO₂ + ZnO, which is more active than TiO₂ and ZnO, were compared with Du-145 cells and L-929 cells. Represents the mean ± SEM of three separate experiments (***p < 0.0001 , **p < 0.001 and *p < 0.01).

DOI: <http://dx.doi.org/10.32571/ijct.613536>

E-ISSN:2602-277X

Cytotoxic activity of TiO₂ + ZnO was high after 72 h in the L-929 cell line. However, we found that TiO₂ + ZnO cytotoxic activity was more active in DU-145 cells compared to L-929 cells after 24 h, 48 h, and 72 h incubation (Figures 4-6). We found this difference statistically significant. (**p < 0.0001, *p < 0.001 and **p < 0.01). As a result, we noted that the synergistic effect of NPs showed more cytotoxic activity in cancer cells. In our previous study in human cervical cancer (HeLa) cells, we found similar results.¹³ Fadoju and co-workers support the results of our study.²⁴

4. CONCLUSIONS

In summary, TiO₂ + ZnO NC was synthesized successfully. The synthesized NPS and NC maintained their stability and are within the acceptable range for stability. This study demonstrates the possibility of using TiO₂ + ZnO to inhibit the growth of DU-145 cancer cells with therapeutic treatments. Healthy L-929 cells were used as the control of DU-145 cells. The cytotoxic activity of TiO₂ + ZnO molecule was highest in DU-145 cancer cells after 72 h incubation. Therefore, we found that the synergistic effect of TiO₂ and ZnO NPs was higher in the cancer cell. By utilizing this synergistic effect, TiO₂ + ZnO NC based drugs can be developed.

ACKNOWLEDGEMENTS

This study was carried out at Cumhuriyet University's Advanced Technology Application and Research Center (CUTAM).

Conflict of interests

Authors declare that there is no a conflict of interest with any person, institute, company, etc.

REFERENCES

- Hui-Ping, L.; Ching-Yu, L.; Chun-Chieh, L.; Liang-Cheng, Su Chieh, H.; Ying-Yu, K.; Jen-Chih, T.; Jong-Ming, H.; Chi-Kuan, C.; Chih-Pin, C. *Int. J. Mol. Sci.* **2013**, 14, 5264-5283.
- Szliszka, E.; Krol, W. *Oncol. Rep.* **2011**, 26, 533-541.
- Cimino, S.; Sortino, G.; Favilla, V.; Castelli, T.; Madonia, M.; Sansalone, S.; Russo, GI.; Morgia, G. *Oxid Med Cell Longev.* **2012**, ID 632959, 8 pages.
- Skandalis, S. S.; Gialeli, C.; Theocharis, A. D.; Karamanos, N. K. *Adv. Cancer Res.* **2014**, 123, 277-317.
- Jabir, N. R.; Tabrez, S.; Ashraf, G. M.; Shakil, S.; Damanhour, G. A.; Kamal, M. A. *Int. J. Nanomedicine* **2012**, 7, 4391-4408.
- J. Wu, Y.; Wang, X.; Yang, Y.; Liu, J.; Yang, R. *Nanotechnology* **2012**, 10, 23-35.
- Yang, D.; Wenzhi, R.; Yaqian, L.; Qian, Z.; Leyong, Z.; Chongwei, C.; Aiguo, W.; Jie, T. *Royal Soc. Chem.* **2015**, 16, 38-59.
- Rozhkova, EA.; Ulasov, I.; Lai, B.; Dimitrijevic, NM.; Lesniak, MS.; Rajh, T. *Nano Lett.* **2009**, 9, 3337-3342.
- S. Shen, X.; Guo, L.; Wu, M.; Wang, X.; Wang, F.; Kong, H.; Shen, M.; Xie, Y. *J. Mater. Chem.* **2014**, 2, 5775-5784.
- Zhao, C.; Zhang, X.; Zheng, Y. *J. Photochem. Photobiol. B: Biology* **2018**, 183, 142-146.
- Carp, O.; Huisman, C. L.; Reller, A. *Prog. Solid State Chem.* **2004**, 32, 33-177.
- Zhou, J.; Xu, N. S.; Wang, Z. L. *Adv. Mater.* **2006**, 18 (18), 2432-2435.
- Tas, A.; Cakmak, N. K.; Silig, Y. *Inter. J. Modern Res. Eng. Technol.* **2018**, 3.
- Rrajendar, V.; Raghu, Y.; Rajitha, B.; Chakra, C. S.; Rao, K. V.; Park, S. H. *J. Ovonic Res.* **2017**, 13.
- Bolukbasi Sahin, S.; Keklikcioglu Cakmak, N.; Tas, A.; Ozmen, E.; Cevik, E.; Gumus, E.; Silig, Y. *Int. J. Sci. Technol. Res.* **2018**, 4 (8), 78-84.
- Skehan, P.; Storeng, R.; Scudiero, D.; Monks, A.; McMahon, J.; Vistica, D.; Warren, J. T.; Bokesch, H.; Kenney, S.; Boyd, M. R. *J. Natl. Cancer Inst.* **1990**, 82, 1107-1112.
- Von der Kammer, F.; Ottofuelling, S.; Hofmann, T. *Environ. Pollut.* **2010**, 158, 3472-3481.
- McNeil, S. E. *J. Leukoc. Biol.* **2005**, 78, 585-594.
- Bisht, G.; Rayamajhi, S. *Nanobiomedicine* **2016**, 3, 3-9.
- Cho, W. S.; Kang, B. C.; Lee, J. K.; Jeong, J.; Che, J. H.; Seok, S. H. *Part Fibre Toxicol.* **2013**, 10, 9.
- Hanley, C.; Layne, J.; Punnoose, A.; Reddy, K. M.; Coombs, I.; Coombs, I.; Coombs, A.; Feris, K.; Wingett, D. *Nanotechnology* **2008**, 19 (29), 295103.

DOI: <http://dx.doi.org/10.32571/ijct.613536>

E-ISSN:2602-277X

22. Kansara, K.; Patel, P.; Shah, D.; Shukla, R. K.; Singh, S.; Kumar, A.; Dhawan, A. *Environ. Mol. Mutagen.* **2015**, 56 (2), 204-217.

23. Tomasina, J.; Poulain, L.; Abeilard, E.; Giffard, F.; Brotin, E.; Carduner, L. Malzert-Fréon, A. *Int. J. Pharm.* **2013**, 458 (1), 197-207.

24. Fadoju, O.; Ogunsuyi, O.; Akanni, O.; Alabi, O.; Alimba, C.; Adaramoye, O. Bakare, A. *Environ. Toxicol. Pharm.* **2019**, 103204.

ORCID

 <https://orcid.org/0000-0002-7132-1325> (A. Tas)

 <https://orcid.org/0000-0002-8634-9232> (N. Keklikcioğlu Cakmak)

 <https://orcid.org/0000-0003-3433-8870> (T. Agbektas)

 <https://orcid.org/0000-0002-0562-7457> (Y. Silig)



Quantitative modeling for prediction of boiling points of phenolic compounds

Soumaya KHEROUF¹, Nabil BOUARRA^{1,2}, Djelloul MESSADI^{1,*}

on the last page

¹Laboratory of Environmental and Food Safety, Department of Chemistry, Badji Mokhtar- Annaba University, PB12, 23000, Annaba. Algeria

²Centre de Recherche Scientifique et Technique en Analyses Physico-Chimiques, BP 384, Siège ex-Pasna Zone Industrielle, Bou-Ismaïl CP 42004, Tipaza, Algeria

Received: 23 October 2019; Revised: 25 November 2019; Accepted: 27 November 2019

*Corresponding author e-mail: djelloul.messadi@univ-annaba.org

Citation: Kherouf, S.; Bouarra, N.; Messadi, D. <i>Int. J. Chem. Technol.</i> 2019, 3 (2), 121-128.
--

ABSTRACT

This work aims to reveal the correlation of the boiling point values of phenolic compounds with their molecular structures using a quantitative structure-property relationship (QSPR) approach. A large number of molecular descriptors have been calculated from molecular structures by the DRAGON software. In this study, all 56 phenolic compounds were divided into two subsets: one for the model formation and the other for external validation, by using the Kennard and Stone algorithm. A four-descriptor model was constructed by applying a multiple linear regression based on the ordinary least squares regression method and genetic algorithm/variables subsets selection. The good of fit and predictive power of the proposed model were evaluated by different approaches, including single or multiple output cross-validations, the Y-scrambling test, and external validation through prediction set. Also, the applicability domain of the developed model was examined using Williams plot. The model shows $R^2 = 0.876$, $Q^2_{LOO} = 0.841$, $Q^2_{LMO} = 0.831$ and $Q^2_{EXT} = 0.848$. The results obtained demonstrate that the model is reliable with good predictive accuracy.

Keywords: Phenolic compounds, boiling point, QSPR, MLR, prediction set.

Fenolik bileşiklerin kaynama noktalarının belirlenmesi için kantitatif modelleme

ÖZ

Bu çalışma, kantitatif yapı-özellik ilişkisi (QSPR) yaklaşımı kullanarak fenolik bileşiklerin kaynama noktası değerlerinin moleküler yapıları ile korelasyonunu ortaya koymayı amaçlamaktadır. DRAGON yazılımı ile moleküler yapılarından çok sayıda moleküler tanımlayıcı hesaplanmıştır. Bu çalışmada, 56 fenolik bileşik Kennard ve Stone algoritması kullanılarak biri model oluşumu için diğeri dış doğrulama için iki alt gruba ayrılmıştır. Sıradan en küçük kareler regresyon yöntemi ve genetik algoritma / değişken altkümeleri seçimine dayanan çoklu bir doğrusal regresyon uygulanarak dört tanımlayıcı model oluşturulmuştur. Önerilen modelin iyi uyum ve tahmin gücü, tahmin seti aracılığıyla tekli ya da çoklu çıkış çapraz validasyonları, Y-kombinasyon testi ve dış doğrulamayı içeren farklı yaklaşımlarla değerlendirilmiştir. Ayrıca, geliştirilen modelin uygulanabilirlik alanı Williams plot kullanılarak incelenmiştir. Model $R^2 = 0.876$, $Q^2_{LOO} = 0.841$, $Q^2_{LMO} = 0.831$ ve $Q^2_{EXT} = 0.848$ 'i göstermektedir. Elde edilen sonuçlar, modelin iyi bir tahmin doğruluğu ile güvenilir olduğunu göstermektedir.

Anahtar Kelimeler: Fenolik bileşikler, kaynama noktası, QSPR, MLR, tahmin seti.

1. INTRODUCTION

Lipidic phenolic compounds are aryl alcohols in which the hydroxyl group (-OH) is attached carbon atom that is part of an aromatic ring, in which phenol is the simplest of these compounds. Anthropogenic produced phenols exist in the environment due to the activity of the chemical, petrol or industrial processes. The entry of

phenolic compounds into ecosystems results from the industrial sewage drainage or the municipal and agricultural activities to surface water.¹ The transport and fate of phenols in the environment depends, in part, on their physicochemical properties, and their relative distributions between different environmental compartments.

As is known, the boiling point is an important physical property that has practical value in chemistry, environmental studies and the pharmaceutical industry,² defined as the temperature at which the vapor pressure of a pure saturated liquid is 1.013×10^5 Pa.³ It is also an indicator of the physical state of organic chemicals (e.g., liquid or gaseous). Furthermore, critical temperatures,⁴ flash points,⁵ and enthalpies of vaporization⁶ can be predicted or estimated by using boiling point. The boiling point of a molecule depends on two main factors. The first factor includes intermolecular forces, such as Coulomb interactions and dipole dipoles. The second explains the size and structure of the molecule as a whole, that is, how the energy supplied by the heater is distributed in rotation and vibration modes.⁷ However, the boiling point data is often not available in the literature and therefore needs to be estimated theoretically. Bp estimation methods have been widely explored⁴⁻¹³ using the topology of the molecule and/or quantum chemistry parameters calculated for the optimized structure of the molecule.

There has been a remarkable increase in the use of quantitative structure property relationships (QSPR) methodology, which used to predict the physical and chemical properties of organic chemicals.¹⁴ In consequence, the QSPR method attempts to correlate the properties of chemicals with relevant properties and molecular structure descriptors by establishing a simple mathematical relationship.¹⁵

The purpose of this study is to find a model for the prediction of the boiling point of various phenolic compounds. Many statistical techniques have been used to develop the model to draw attention to the structural requirements for an exact boiling point value. The three objectives of the present paper have been: first, to explore the structure-property relationships of the boiling point; second, to select the best predictive model from among all developed models for the property, and third, verification of the performance and stability of the obtained model. The model obtained shows which descriptors play a significant role in boiling point variation of phenolic compounds.

2. MATERIAL AND METHODS

2.1. Data set

In the present study, the experimental Bp data listed in Table 1 and 2 were received from the Handbook of Physical-Chemical Properties and Environmental Fate for Organic Chemicals.¹⁶ The reported Bp values ranged from 174.9 to 305°C. The database was divided into two molecular subsets by using Kennard and Stone algorithm,¹⁷ the training set consists of 39 compounds and 17 compounds for the prediction set.

2.2. Modeling and molecular descriptor calculation

All numerical calculations were done by a computer with [®] Core™ processor and 4Gb RAM. The molecular structure of each compound was sketched using the Hyperchem software¹⁸ and pre-optimized using MM+ molecular mechanics method (Polak-Ribiere algorithm). The minimal energy conformations of molecules were then fully optimized and calculated with the semi-empirical PM3 method at the restricted Hartree-Fock level with no configuration interaction,¹⁹ applying a gradient norm limit of $0.001 \text{ kcal } \text{Å}^{-1} \text{ mol}^{-1}$ as a stopping criterion. Lastly, the final geometries with the minimal energy were used as input for the generation of 1664 descriptors using the Dragon software (Version 5.4).²⁰ Type and information of molecular descriptor calculated are available in Dragon software user's guide.²⁰

2.2. Model development and validation

For the model development, by applying multiple linear regression based ordinary least square (OLS), and genetic algorithm-variable subset selection²¹ (GA/VSS) implemented in Mobydigs software²² using the Ordinary Least Squares (OLS) method and GA-VSS (Genetic Algorithm-Variable Subset Selection). This 'variable selection' procedure generates a 'population' of models, ranked according to decreasing Q^2 values. The best models were chosen by using Q^2 leave-one-out (Q^2_{Loo}) as the optimization value and taking into account the parsimony principle regarding the complexity of the models, which should be as small as possible. Furthermore, the correlation between the modeling descriptors and the modeled response was checked by the QUIK rule (Q Under Influence of K), to exclude models with high predictor collinearity and exclude chance correlation.²³

The goodness of the model was reached by verifying the model fitting and the model robustness, using the squared correlation coefficient R^2 (Eq. (1)) and the cross-validation by the leave-one-out technique (Q^2_{Loo}) (Eq. (2)).

$$R^2 = 1 - \frac{\sum_{i=1}^n (y_i - \hat{y}_i)^2}{\sum_{i=1}^n (y_i - \bar{y})^2} \quad (1)$$

$$Q^2_{Loo} = 1 - \frac{\sum_{i=1}^n (\hat{y}_{i/i} - y_i)^2}{\sum_{i=1}^n (y_i - \bar{y})^2} \quad (2)$$

Where y_i is the observed dependent variable (the experimental response), \hat{y}_i is the calculated value by the model, \bar{y} is the mean value of the studied property, n is the number of compounds in the training set, and $\hat{y}_{i/i}$ is the value predicted by the model built without the compound i .

DOI: <http://dx.doi.org/10.32571/ijct.636581>

E-ISSN:2602-277X

Table 1. Molecular descriptors and Bp values for phenols in training set

No	Name	Exp.BP/°C	PW5	Hy	X5A	R6m	Pred. Bp/°C
1	2-Methylphenol	191.04	0.057	-0.16	0.102	0.001	184.104
2	4-Methylphenol	201.98	0.08	-0.16	0.109	0.016	211.419
3	2,6-Dimethylphenol	201.07	0.054	-0.21	0.089	0.005	203.393
4	3,4-Dimethylphenol	227	0.071	-0.21	0.095	0.015	221.586
5	2,4,6-Trimethylphenol	220	0.065	-0.26	0.082	0.018	236.418
6	2-Propylphenol	220	0.082	-0.26	0.104	0.048	226.094
7	4-Propylphenol	232.6	0.085	-0.26	0.1	0.051	240.189
8	2-Isopropylphenol	213.5	0.062	-0.26	0.096	0.022	203.141
9	4-Isopropylphenol	230	0.072	-0.26	0.091	0.073	242.831
10	4-Butylphenol	248	0.088	-0.29	0.1	0.068	246.757
11	2-sec-Butylphenol	228	0.073	-0.29	0.096	0.068	230.179
12	2-tert-Butylphenol	223	0.059	-0.29	0.091	0.029	207.716
13	3-tert-Butylphenol	240	0.076	-0.29	0.093	0.058	238.970
14	4-sec-Butylphenol	241	0.074	-0.29	0.09	0.092	250.322
15	4-tert-Butylphenol	237	0.066	-0.29	0.084	0.095	250.308
16	4-tert-Octylphenol	279	0.076	-0.4	0.085	0.161	274.000
17	1-Naphthol	288	0.094	-0.29	0.084	0.013	276.601
18	2-Naphthol	285	0.101	-0.29	0.084	0.036	293.926
19	2-Phenylphenol	286	0.095	-0.35	0.087	0.099	289.135
20	4-Phenylphenol	305	0.095	-0.35	0.087	0.093	287.652
21	2-Allylphenol	220	0.082	-0.26	0.104	0.037	223.375
22	4-Chlorophenol	220	0.08	-0.04	0.109	0.01	218.370
23	2,3-Dichlorophenol	206	0.054	-0	0.089	0	217.182
24	3,4,5-Trichlorophenol	275	0.065	0.031	0.082	0.01	254.852
25	4-Nitrophenol	279	0.072	0.031	0.091	0.103	270.657
26	1,2-Dihydroxybenzene	245	0.057	0.846	0.102	0.001	255.259
27	1,3-Dihydroxybenzene	276.5	0.06	0.846	0.097	0.001	270.704
28	Hydroquinone	285	0.08	0.846	0.109	0.007	280.349
29	2-Methoxyphenol	205	0.063	-0.11	0.101	0.015	203.248
30	3-Methoxyphenol	244	0.074	-0.11	0.102	0.028	222.661
31	2,6-Dimethoxyphenol	261	0.075	-0.12	0.09	0.051	254.253
32	3-Methylphenol	202.27	0.06	-0.16	0.097	0.002	199.797
33	3,5-Dimethylphenol	221.74	0.058	-0.21	0.082	0.007	225.178
34	2,3,5-Trimethylphenol	233	0.065	-0.26	0.082	0.016	235.924
35	3,4,5-Trimethylphenol	248.5	0.065	-0.26	0.082	0.016	235.924
36	2-Ethylphenol	204.5	0.063	-0.21	0.101	0.013	195.241
37	4-Ethylphenol	217.9	0.078	-0.21	0.098	0.04	233.131
38	2,5-Dichlorophenol	211	0.071	-0	0.095	0	232.903
39	2,4,6-Trichlorophenol	246	0.065	0.031	0.082	0.01	254.852

Table 2. Molecular descriptors and Bp values for phenols in prediction set

No	Name	Exp.BP/°C	PW5	Hy	X5A	R6m	Pred. Bp/°C
1	3-Ethylphenol	218.4	0.074	-0.213	0.102	0.023	213.913
2	Phenol	181.87	0.062	-0.088	0.113	0	174.129
3	2-Chlorophenol	174.9	0.057	-0.039	0.102	0	192.291
4	3,4-Dichlorophenol	253	0.071	-0.001	0.095	0.01	235.375
5	4-Chloro-3-methylphenol	235	0.071	-0.107	0.095	0.011	228.110
6	2-Nitrophenol	216	0.062	0.031	0.096	0.008	220.091
7	4-Methoxyphenol	243	0.078	-0.107	0.098	0.036	239.655
8	4-Hydroxy-3-methoxybenzaldehyde	285	0.086	-0.119	0.09	0.088	281.690
9	2,3-Dimethylphenol	216.9	0.054	-0.213	0.089	0.003	202.899
10	2,4-Dimethylphenol	210.98	0.071	-0.213	0.095	0.016	221.833
11	2,5-Dimethylphenol	211.1	0.071	-0.213	0.095	0.014	221.339
12	2,4,5-Trimethylphenol	232	0.076	-0.257	0.088	0.025	243.892
13	3-Chlorophenol	214	0.06	-0.039	0.097	0	207.736
14	2,4-Dichlorophenol	210	0.071	-0.001	0.095	0.01	235.375
15	2,6-Dichlorophenol	220	0.054	-0.001	0.089	0	217.182
16	3,5-Dichlorophenol	233	0.058	-0.001	0.082	0	238.472
17	2,4,5-Trichlorophenol	247	0.076	0.031	0.088	0.01	260.596

Besides, the Root Mean Squared of Error (RMSE) that resume the overall error of the model, which used to measure and compare prediction accuracy in the training (RMSE_{tr}) and the prediction (RMSE_p) sets defined in Eq. (3).

$$RMSE_{tr(p)} = \sqrt{\frac{1}{n_{tr(ext)}} \sum_{i=1}^{n_{tr(ext)}} (y_i - \hat{y}_i)^2} \quad (3)$$

A stronger internal validation is performed by using the LMO (leave-many-out) procedure. By design, model validation by LMO employs smaller training sets than the LOO procedure and can be repeated many more times due to the possibility of larger combinations in leaving many compounds out from the training set, it is common to choose 5-40% of the entire number molecules in the training set to be left. The premise is that if a QSPR model has a high average in Q²_{LMO} validation, we can reasonably conclude that the obtained model is robust.²⁴

Obtaining a robust model does not give real information about its prediction power. This is evaluated by predicting the compounds included in the test set. The external for the test set is determined by using Eq. (4):

$$Q_{ext}^2 = 1 - \frac{\sum_{i=1}^{n_{ext}} (\hat{y}_{i/i} - y_i)^2 / n_{ext}}{\sum_{i=1}^{n_{tr}} (y_i - \bar{y})^2 / n_{tr}} \quad (4)$$

Here n_{ext} and n_{tr} are the number of objects in the external set and the number of training set objects, respectively.

In order to exclude the possibility of a chance correlation between the selected descriptors and the studied response, Y-scrambling as an internal validation method was used. In this method, the dependent-variable vector, Y-vector, are randomly permuted and a new QSPR model is developed using the selected descriptor in the model.²⁵

A successful QSPR model should be validated with the test set and satisfies criteria in Equations (5-9).^{24, 25}

$$Q_{LOO}^2 > 0.5 \quad (5)$$

$$Q_{ext}^2 > 0.5 \quad (6)$$

$$R^2 > 0.6 \quad (7)$$

$$(R^2 - R_0^2) / R^2 < 0.1 \text{ or } (R^2 - R'^2_0) / R^2 < 0.1 \quad (8)$$

$$0.85 \leq k \leq 1.15 \quad \text{or} \quad 0.85 \leq k' \leq 1.15 \quad (9)$$

Where R_0^2 (predicted versus observed values) and R'^2_0 (observed versus predicted values) are coefficients of determination, k and k' are slopes of regression lines through the origin of predicted versus observed and observed versus predicted respectively. Mathematical definitions of parameters (R_0^2 , R'^2_0 , k , and k') can be found in the literature.^{24,26}

2.3. Applicability Domain (AD)

Williams plot, the plot of standardized residuals versus the leverage (h_{ii})^{27,28} is always used to verify the applicability domain (AD) of the developed QSPR model. The structural AD is quantified by applying the leverage approach, this approach is based on the calculation of the Hat matrix for the structural domain. Leverage indicates a compounds distance from the centroid of X. The leverage of a compound in the original variable space is defined as in Eq. (10):²⁷

$$h_{ii} = x_i^T (X^T X)^{-1} x_i \quad (10)$$

Where x_i is the descriptor vector of the considered compound and X is the descriptor matrix derived from the training set descriptor values. The warning leverage h^* was calculated according to Eq. (11)²⁹

$$h^* = 3(p + 1) / n \quad (11)$$

Where p is the number of independent variables used and n is the number of compounds in the training set.

The leverages approach was used to estimate the degree of extrapolation for the predictions obtained in the training and prediction sets and for compounds without experimental data. The chemicals with a leverage $h_{ii} > h^*$ are outside the structural domain of the training set. therefore, their predictions are extrapolations and could be less reliable.

3. RESULTS AND DISCUSSION

The hybrid method genetic algorithm/Multiple linear Regression (GA/MLR) included in MOBYDIGS software was used to select the best descriptors able to explicating property variation in the training set. Finally, a 4-variables model was chosen as the best model. The regression equation of the developed model defined as follows:

$$BP = 314 + 1663 PW5 + 70.9 Hy - 2091 X5A + 247 R6m \quad (12)$$

$N_{tr} = 39$, $N_{pr} = 17$, $S = 11.111^\circ\text{C}$, $RMSE_{tr} = 10.375$,

$RMSE_{pr} = 11.4928$. $F = 60.4552$

$R^2 = 0.876$, $Q^2_{LOO} = 0.841$, $Q^2_{LMO} = 0.848$, $Q^2_{ext} =$

0.848.

The statistical parameters that evaluate the model are listed in Table 3, from this table we can conclude that the statistical parameters of the developed model have very good predictive performance and that the descriptors in which it is involved describe well the boiling point. The

developed model satisfies the above accept conditions (Equations (5-9)).

Statistical parameters and the meanings of descriptors are grouped in Table 4. The probability (P) that the descriptor is there by chance, should usually be less than 0.05 (i.e., 5%) to be considered statistically significant; otherwise this descriptor should be thrown out, the P-values suggests that all the descriptors in each model are significant. The high absolute t-values means that the regression coefficients of the descriptors introduced in the model are significantly larger than the standard deviation, values of VIF less than 5 indicate that the descriptors are not strongly correlated with each other.³⁰

Another proof of the model quality is the strong correlation between observed and predicted Bp values for both training and prediction sets. Figure 1 illustrates the predicted values of the boiling point versus the experimental values, the correlation coefficient ($R^2 = 0.876$) of this plot indicates the good agreement between these values, which prove the reliability of the model.

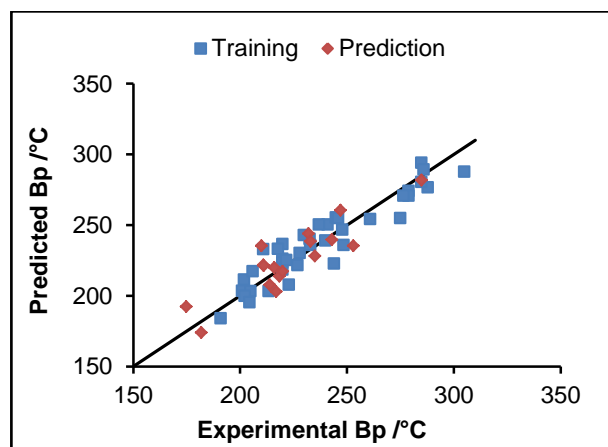


Figure 1. Scatter plot of experimental and predicted boiling point.

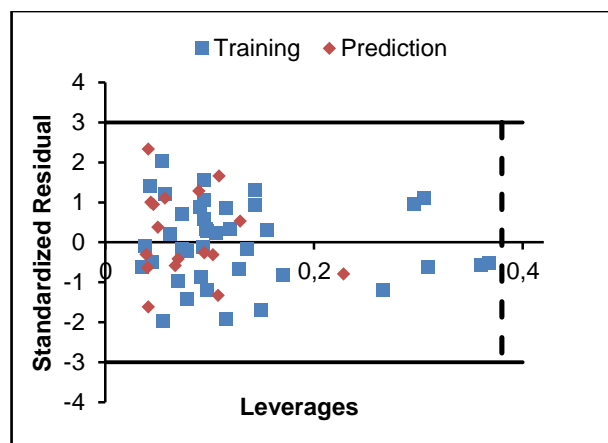


Figure 2. The respective Williams plot of standardized residual versus leverages for the model.

Table 3. Evaluation results of the developed model

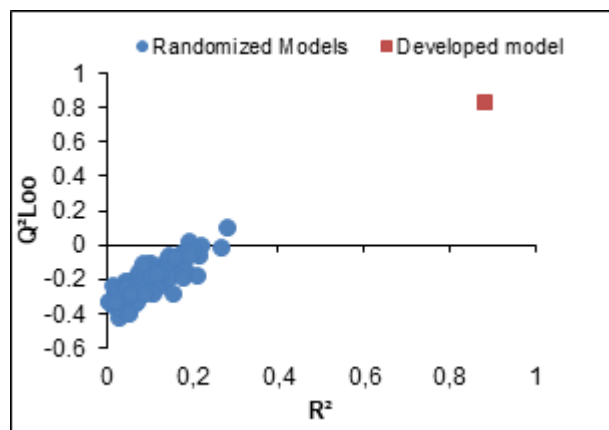
Training set			Prediction set				
R^2	Q^2_{LOO}	Q^2_{LMO}	Q^2_{ext}	$(R^2 - R^2_0) / R^2$	$(R^2 - R^2_0) / R^2$	k	k'
0.8767	0.841	0.831	0.848	0.0059	0.0244	0.9907	1.0068

Table 4. Characteristics of the selected descriptors in the model

Predictor	Descriptors	signification	Coefficient	SE Coef	T	P	VIF
Constant			313.58	22.68	13.83	0.000	
PW5	Path/walk 5 - Randic shape index		1662.9	173.3	9.59	0.000	1.358
Hy	Hydrophilic factor		70.871	6.910	10.26	0.000	1.364
X5A	Average connectivity index of order 5		-2091.3	235.5	-8.88	0.000	1.222
R6m	R autocorrelation of lag 6 / weighted by mass		247.16	57.83	4.27	0.000	1.471

Figure 2 shows the Williams plot. As can be seen in this figure, all residuals were situated on the range of ± 3 standard deviations (horizontal lines) and also there is no structural influential compound both for training and prediction sets (here, the leverage value h_i of all data sets are lower than the warning value $h^* = 0.38$), which means that the model has a good predictive ability. So, the developed model could be used to predict the boiling point of phenolic compounds just from their molecular structure.

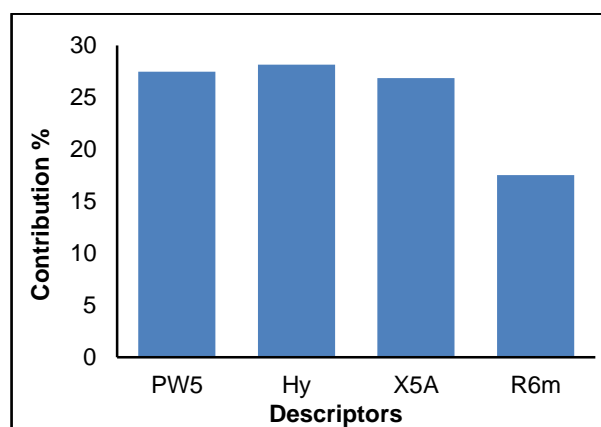
The Y-scrambling tests between the original and permuted response data indicate the robustness of the model. The significant low values of R^2_{Yscr} and Q^2_{Yscr} (black circle) obtained for 100 iterations confirm the robustness of the developed model (asterisk). Figure 3 shows that in the case of all randomized models, the values of R^2_{Yscr} and Q^2_{Yscr} were < 0.5 this insure that the good results of the original model have a real basis, not due to chance correlation.

**Figure 3.** Randomization test: R^2 and Q^2 of Y-scrambled models compared with the original model.

3.1. Descriptor contribution and interpretation

In order to verify the relative contributions of the four descriptors in the developed model, they are illustrated in Figure 4. The importance of the descriptors included in the model decreases in the following order: *Hy* (28.155%) > *PW5* (27.476%) > *X5A* (26.844%) > *R6m* (17.524%).

The most significant descriptor is a hydrophilic factor (*Hy*), which gives a correlation with Bp of 0.196 and explains 28.155% of the contributions. The hydrophilic factor is a simple empirical index related to the hydrophilicity of compounds based on count descriptors.³¹ It is a measure of the number of hydrophilic functional groups (-OH,-SH,-NH).³² The Molecular property descriptor here digitizes the hydrophilic properties of the molecules caused by the group "OH".³¹

**Figure 4.** Relative contributions of the descriptors in the developed model.

DOI: <http://dx.doi.org/10.32571/ijct.636581>

E-ISSN:2602-277X

The second significant descriptor is *PW5*, which gives a correlation with Bp of 0.566 and explains 27.47% of the contributions. *PW5* is a topological index that considers the shape of molecules as molecular properties in the variations of compounds.³³ The shape of molecules with a specific kind of branching was also selected as a significant descriptor in the QSAR model developed by Mitra and co-workers.³⁴ The variation in branching structural features has also been considered by Ray and co-workers³⁵ to develop the specific QSAR model. *PW5* refers to the proportions of path/walk-in length 5 from the molecular Randic shape index. Randic³⁶ characterizes shape index for a molecular graph by considering both paths and walks of different lengths within a graph and then making the proportions of the number of path and the number of walks the same length. The third descriptor is *X5A*, this descriptor belongs to Connectivity indices descriptors; *X5A* is the fifth-order average connectivity index appearing in the MLR model mainly shows the topological characteristics. Topological indices are numerical quantifiers of molecular topology and an H-depleted molecular graph. They involve one or more structural features of the molecule such as the size, shape, symmetry, and branching and can also codify chemical information about atom type and bond multiplicity.³⁷ The last descriptor is *R6m* belongs to GETAWAY descriptor, and provides information on the molecular leverage autocorrelation of lag 6 weighted by atomic mass. *R6m* is a geometrical descriptor encoding information on the real position of substituent and fragments in the molecular space.^{38,39}

4. CONCLUSIONS

In this work, quantitative relationships between the boiling point and some phenolic compounds, and their molecular descriptors were investigated by using multiple linear regression techniques. Genetic algorithm is a powerful method used to reduce the number of descriptors in the development of the models. The selected descriptor in this study gives a good estimate for boiling point, indicated by several calculated metrics, R^2 for the goodness of fit, Q^2_{LOO} and Q^2_{LMO} for robustness, and Q^2_{ext} for the predictive power of the model. Also, the applicability domain of the MLR model is verified by the leverage approach. In conclusion, the model proposed in this work provides a feasible, effective and practical tool to predict the boiling point of phenolic compounds.

Conflict of interests

Authors declare that there is no a conflict of interest with any person, institute, company, etc.

REFERENCES

1. Michałowicz, J.; Duda, R.O.W. *Water. Air. Soil. Pollut.* **2005**, 16, 205-222.
2. Todeschini, R.; Gramatica, P.; Provenazi, R.; Marengo, E.; *Chemom. Intell. Lab. Syst.* **1995**, 27, 221-229.
3. Gharagheizi, F.; Mirkhani, S. A.; Ilani-Kashkouli, P.; Mohammadi, A. H.; Ramjugernath, D. Richon, D.; *Fluid Phase Equilib.* **2013**, 354, 250-258.
4. Katritzky, A. R.; Mu, L.; Lobanov, V. S. *J. Phys. Chem.* **1996**, 100, 10400-10407.
5. Yi-min, D.; Zhi-ping, Z.; Zhong, C.; Yue-fei, Z.; Julian, Z.; Xun L. *J. Mol. Graphics. Modell.* **2013**, 44, 113-119.
6. White, C.M. *J. Chem. Eng. Data.* **1986**, 31, 198-203.
7. Smeeks, F.C.; Jurs, P.C. *Anal. Chim. Acta.* **1990**, 233, 111-119.
8. Admire, B.; Lian, B.; Yalkowsky, S. H. *Chemosphere.* **2015**, 119, 1436-1440.
9. Shuai, D.; Wen, S.; Li, Zhao. *Int. J. Refrig.* **2016**, 63, 63-71.
10. Liangjie, J.; Peng B. *Chemom. Intell. Lab. Syst.* **2016**, 157, 127-132.
11. Ramane, H. S.; Yalnaik, A. S. *J. Appl. Math. Comput.* **2017**, 55, 1-2, 609-627.
12. Varamesh, A.; Hemmati-Sarapardeh, A.; Dabir, B.; Mohammadi, A.H. *J. Mol. Liq.* **2017**, 242, 59-69.
13. Arjmand, F.; Shafiei, F. *J. Struc. Chem.* **2018**, 59, 3, 748-754.
14. Katritzky, A. R.; Maran, U.; Lobanov, V. S.; Karelson, M. *J. Chem. Inf. Comput. Sci.* **2000**, 40, 1-18.
15. Katritzky, A. R.; Lobanov, V. S.; Karelson, M. *Chem. Soc. Rev.* **1995**, 24, 279-287.
16. Mackay, D.; Shiu, W.Y.; Ma, K.C.; Lee, S.C. *Handbook of Physical-Chemical Properties and Environmental Fate for Organic Chemicals*, CRC Press Taylor & Francis Group 6000 Broken Sound Parkway NW, Suite 300 Boca Raton, FL 33487-2742. Vol III, 2006.

DOI: <http://dx.doi.org/10.32571/ijct.636581>

E-ISSN:2602-277X

17. Kennard, R.; Stone, L.A. *Technometrics*. **1969**, 11, 137-148.
18. HyperChem 6.03 Package. Hypercube, Inc., Gainesville, Florida, USA, 1999, software available at: <http://www.hyper.com>.
19. Gaber, M.M. *Scientific Data Mining and Knowledge Discovery: Principles and Foundations*; Springer Heidelberg Dordrecht London, Berlin, 2009.
20. Talete Srl. *Dragon for Windows (Software for Molecular Descriptor Calculation)* Version 5.5 Milano, Italy, 2007, software available at: <http://www.talete.mi.it>.
21. Leardi, R.; Boggia, R.; Terrile, M. *J. Chemom.* **1992**, 6, 267-281.
22. Todeschini, R.; Ballabio, D.; Consonni, V.; Mauri, A.; Pavan, M. 2009. Mobydigs – version 1.1 – Copyright TALETE Srl.
23. Todeschini R.; Maiocchi A.; Consonni, V. *Chemom. Int. Lab. Syst.* **1999**, 46, 13-29.
24. Tropsha, A.; Gramatica, P.; Gombar, V. K. *QSAR Comb. Sci.* **2003**, 22, 70-77.
25. Golbraikh, A.; Tropsha, A. *J. Mol. Graph. Model.* **2002**, 20, 269-276.
26. Yu, X. L.; Yi, B.; Yu, W. H.; Wang, X. Y. *Chem. Pap.* **2008**, 62, 623-229.
27. Netzeva, T.I.; Worth, A.P.; Aldenberg, T.; Benigni, R.; Cronin, M.T.D.; Gramatica, P.; Jaworska, J.S.; Kahn, S.; Klopman, G.; Marchant, C.A.; Myatt, G.; Nikolova-Jeliazkova, N.; Patlewicz, G.Y.; Perkins, R.; Roberts, D.W.; Schultz, T.W.; Stanton, D.T.; vande Sandt, J.J.M.; Tong, W.; Veith, G.; Yang, C. *Altern. Lab. Anim.* **2005**, 33, 155–173.
28. Gramatica, P.; Cassani, S. Roy, P. P. Kovarich, S.; Yap, C. W. Papa, E. *Mol. Inform.* **2012**, 31, 817-835.
29. Eriksson, L.; Jaworska, J.; Worth, A.P.; Cronin, M.T.D.; McDowell, R.M.; Gramatica, P. *Environ. Health. Perspect.* **2003**, 111, 1361-1375.
30. Jaiswal, M.; Khadikar, P.V.; Scozzafava, A.; Supuran, C.T. *Bioorg. Med. Chem. Lett.* **2004**, 14, 3283-3290.
31. Todeschini, R.; Consonni, V. *Molecular Descriptors for Chemoinformatics*; Wiley-VCH: Weinheim, Germany, 2009.
32. Gramatica, P.; Navas, N.; Todeschini, R. *Trends Anal. Chem.* **1999b**, 18, 461-471.
33. Randic, M.; Razinger, M. *J. Chem. Inf. Model.* **1995**, 35, 140-147.
34. Mitra I.; Saha A.; Roy K. *Mol. Simul.* **2010**, 36, 1067-1079.
35. Ray, S.; Sengupta, C.; Roy K. *Cent. Eur. J. Chem.* **2007**, 5, 1094-1113.
36. Randic, M. *J. Chem. Inf. Model.* **2001**, 41, 607-613.
37. Abbasi, M.; Sadeghi-Aliabadi, H.; Amanlou, M. *J. Pharm. Sci.* **2017**, 25, 1-17.
38. Consonni, V.; Todeschini, R.; Pavan, M. *J. Chem. Inf. Comput. Sci.* **2002**, 42, 682-692.
39. Consonni, V.; Todeschini, R.; Pavan, M.; Gramatica, P. *J. Chem. Inf. Comput. Sci.* **2002**, 42, 693-705.


ORCID

ID <https://orcid.org/0000-0001-9797-3746> (S. Kherouf)ID <https://orcid.org/0000-0001-5438-8678> (N. Bouarra)ID <https://orcid.org/0000-0003-3257-9590> (D. Messadi)



Effect of measurement frequency on admittance characteristics in Al/p-Si structures with interfacial native oxide layer

Muhammed Can OZDEMİR¹, Omer SEVGİLİ², Ikram ORAK², Abdulmecit TURUT³

 on the last page

¹Department of Nanoscience and Nanoengineering, Institute of Graduate Education, Istanbul Medeniyet University 34700, Istanbul, Turkey

²Vocational School of Health Services, Bingöl University, 12000, Bingöl, Turkey

³Department of Engineering Physics, Faculty of Engineering and Natural Sciences, Istanbul Medeniyet University, 34700, Istanbul Turkey

Received: 05 November 2019; Revised: 30 November 2019; Accepted: 01 December 2019

*Corresponding author e-mail: amecit2002@yahoo.com

Citation: Ozdemir, M. C.; Sevgili, O.; Orak, I.; Turut, A. *Int. J. Chem. Technol.* 2019, 3 (2), 129-135.

ABSTRACT

Al/p-Si/Al diodes with interfacial native oxide layer were formed. Their frequency induced admittance-voltage measurements were made. The frequency-dependent density distribution of interface states has been determined from the corrected characteristics by considering the series resistance effect which masks the interface trap loss. The majority carrier density corresponding to the depletion and inversion parts of the C^2-V curve, was determined 1.82×10^{14} and $4.48 \times 10^{14} \text{ cm}^{-3}$ at 1000 kHz, respectively. The fact that the carrier density obtained from the inversion part of the plot is higher than that obtained from the depletion part can be related to the increase in the density of negative space charge in the depletion region. The value of Φ_{CV} was determined as 0.95 eV from the same plot. Interface state density decreased from $4.31 \times 10^{12} \text{ eV}^{-1}\text{cm}^{-2}$ at 100 kHz to $7.30 \times 10^{11} \text{ eV}^{-1} \text{cm}^{-2}$ at 1000 kHz, because the interface charges do not follow the *ac* signal and do not contribute to capacitance values in high frequencies.

Keywords: Metal-semiconductor contacts, MIS diodes, interface states, capacitance characteristics, conductance characteristics.

Doğal oksit arayüzey tabakalı Al/p-Si yapılarında admittans karakteristikleri üzerine ölçüm frekansının etkisi

ÖZ

Arayüzey doğal oksit tabakalı Al/p-Si/Al diyotlar imal edildi. Onların frekans bağımlı admittans voltaj ölçümleri de yapılmıştır. Arayüz durumlarının frekans bağımlı yoğunluk dağılımı, ara yüzey tuzak kaybını maskeleyen seri direnç etkisi dikkate alınarak düzeltilmiş admittans datarlarından belirlenmiştir. C^2-V eğrisinin tükenim ve tersinim kısımlarına karşılık gelen çoğunluk taşıyıcı yoğunluğu 1000 kHz'de sırasıyla 1.82×10^{14} and $4.48 \times 10^{14} \text{ cm}^{-3}$ olarak belirlenmiştir. Eğrinin tersinim kısmından elde edilen taşıyıcı yoğunluğunun, tükenim kısmından elde edilen kinden daha fazla olması, tükenim bölgesindeki negatif uzay yükü yoğunluğunun artmasıyla ilişkilendirilebilir. Φ_{CV} 'nin değeri aynı grafikten 0,95 eV olarak belirlenmiştir. Arayüzey hallerinin yoğunluğu 100 kHz'de $4.31 \times 10^{12} \text{ eV}^{-1}\text{cm}^{-2}$ 'den 1000 kHz'de $7.30 \times 10^{11} \text{ eV}^{-1} \text{cm}^{-2}$ 'ye düşmüştür, çünkü arayüzey yükleri *ac* sinyalini takip edememektedir ve yüksek frekanslarda kapasitans değerlerine katkıda bulunamamaktadır.

Anahtar Kelimeler: Metal-yarıiletken kontaklar, MIS diyotlar, arayüz halleri, kapasitans özellikleri, iletkenlik özellikleri.

1. INTRODUCTION

The quality and understanding of the metal/semiconductor (MS) devices such as bipolar transistors, photodiodes, rectifiers, MS field-effect transistors (MESFETs) and metal/oxide layer/semiconductor FETs (MOSFETs) depend on the

electrical properties and the production of metal/semiconductor contacts. In general, in metal/insulating layer/semi-conductor (MIS) device fabrication, the rectifying contact metals may cause some damage onto the semiconductor substrate surface and thus an insulating or oxide layer deposition on the surface of substrate may prevent possible damage.¹⁻⁷

DOI: <http://dx.doi.org/10.32571/ijct.642886>

The available defects at the interfaces of metal-semiconductor (MS) or metal-insulating layer-semiconductor (MIS) or metal-oxide layer-semiconductor (MOS) structures are generally called the interface traps or states. The charges in the interface states can capture or emit electrons (holes), and thus interact with the conduction (valence) band of semiconductor. The interface state energy or density distribution can be estimated through the energy loss resulting from changes in their occupancy by small variations of gate voltage. Majority carriers are captured or emitted and subsequently changes in occupancy of interface trap and energy loss emerge. The energy lost during capture of the majority carriers is taken up by phonons, heating the lattice. This energy loss is measured as an equivalent parallel interface state conductance. In addition to an energy loss associated with capture and emission, interface traps also can hold a charge for some time after capture. That is, interface traps store charge. Therefore, there will be an interface state charge capacitance proportional to interface trap level density. The total energy loss depends on the interface trap density and its relaxation time.¹⁻¹¹

Herein, Al/SiO₂/p-Si/Al MIS diodes were fabricated. The SiO₂ native oxide has formed on the clean Si wafer surface exposed to clean room air. The capacitance-voltage (*C-V*) and conductance-voltage (*G-V*) characteristics of the MIS diode were measured at various frequencies. The interface state density depending on frequency was calculated from the corrected *C-V* and *G-V* characteristics taking into account the series resistance effect which masks the interface trap loss.¹⁻⁸ Intrinsic surface states existing at the semiconductor surface before rectifying metal contact have an important role in Schottky barrier formation. The dangling band of the Si surface can be saturated by the native SiO₂ thin layer. The termination with SiO₂ thin layer causes the variety of notable properties of the silicon surface after exposing to clean room air. Electronically, it is significantly inactive with a largely reduced density of surface states in Si energy band gap.⁴⁻¹⁰

2. PREPERATION OF SAMPLES AND MEASUREMENTS

Al/SiO₂/p-Si/Al MIS diodes were prepared using *p*-type Si(100) with resistivity of 1-10 Ω-cm and average free carrier concentration of 2.28 × 10¹⁵ cm⁻³. The low resistivity ohmic back contact to *p*-type Si(100) wafers was made using Al, followed at 570°C for 3 min under nitrogen gas. The native oxide layer on the clean front surface of the wafer with ohmic contact formed because the wafer was exposed to clean room air at room temperature before evaporating Al Schottky contacts. The front surface of pieces cut from the wafer with ohmic back contact was chemically cleaned using the RCA cleaning procedure and finally has been rinsed in

de-ionized water for 30 s. Prepare RCA bath; 5 parts water (H₂O), 1 part 27% ammonium hydroxide (NH₄OH), 1 part 30% hydrogen peroxide (H₂O₂). Soak wafer in RCA-1 bath at 70°C for 15 min. DI rinse and blow dry. Clean up, dispose wastes (Werner Kern developed the basic procedure in 1965 while working for RCA, the Radio Corporation of America; The RCA Corporation is a major American electronics company, which is founded as the Radio Corporation of America in 1919).¹¹ The Schottky contacts have been formed onto the front surface of slices by evaporation of Al dots with diameter of about 1.75 mm (diode area = 2.41 × 10⁻² cm²). All evaporation processes were performed in a turbo molecular fitted vacuum coating unit at about 10⁻⁶ mbar. The *G-V* and *C-V* characteristics were measured by a HP model 4192A *LF* impedance analyzer, respectively, at room temperature and in the dark.

3. RESULTS AND DISCUSSION

3.1. Impedance characteristics of the diodes

Figures 1a and 1b represent the forward and reverse bias capacitance against voltage curves at various frequencies and 300 K. For the forward branch case of the MIS diode, a negative voltage is applied to the Al/SiO₂ side that is, to the gate metal, with respect to the *p*-Si/Al side, a negative charge will exist on the top of Al Schottky contact metal, and an electric field is induced into the *p*-Si semiconductor substrate. Thus, the majority carrier holes would experience a force toward the native oxide/semiconductor interface and an accumulation layer of holes at the native oxide/semiconductor contact corresponds to the positive charge on the bottom Al Schottky contact metal of the MIS capacitor. We will return to the descriptions of the capacitance-voltage characteristics later, that is, depletion region and inversion layer in the reverse branch of the MIS diode.

Figures 1a and 2 represent the forward and reverse bias *C-V* and *G-V* curves at various frequencies and 300 K. The formed accumulation region corresponds to the saturation region in about 7.5-10 V range at forward branch at 1000 kHz in Figure 1a. The capacitance value of $C_{ox} = 422$ pF is the capacitance of the native oxide layer at 1000 kHz, and the thickness value of the oxide layer can be calculated using C_{ox} value. The capacitance of the interfacial layer of a MIS diode is given in Eq. (1).

$$C_{ox} = \frac{\epsilon_{ox}\epsilon_0 A}{d} \quad (1)$$

where $\epsilon_{ox} = 3.9$ is the permittivity of the interfacial SiO₂ native oxide layer¹² and d is its thickness, respectively, ϵ_0 is the permittivity of free space and A is the area of Al Schottky contact.

DOI: <http://dx.doi.org/10.32571/ijct.642886>

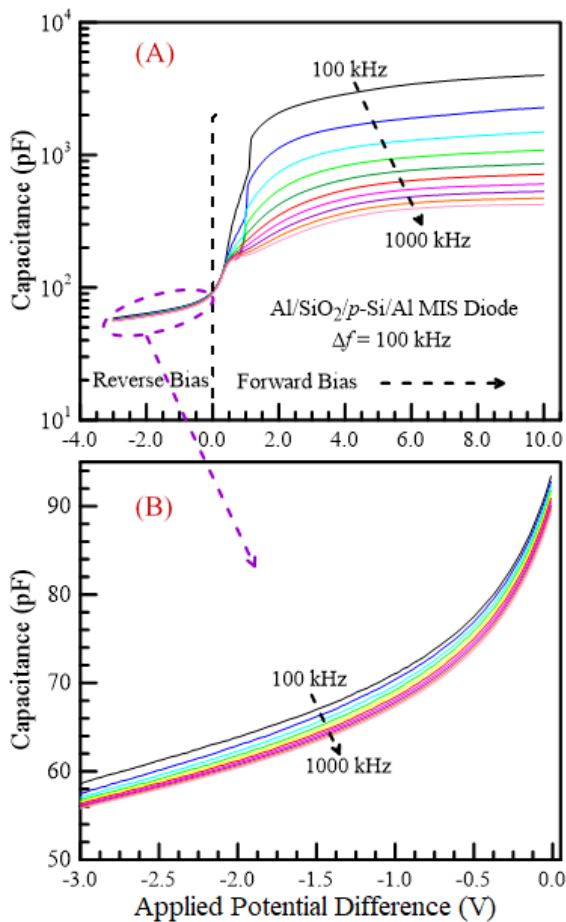


Figure 1. Frequency induced capacitance-voltage characteristics.

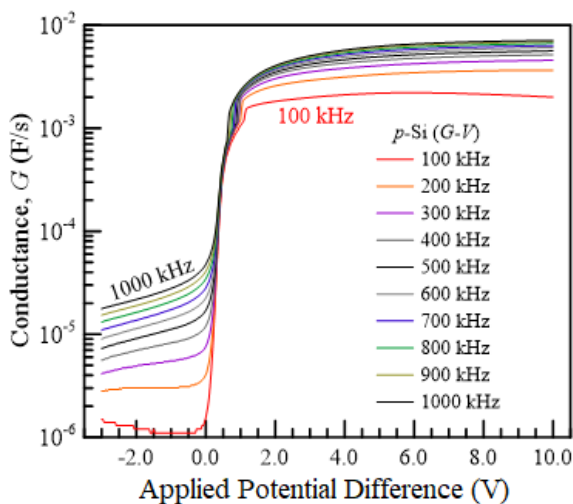


Figure 2. Frequency induced conductance-voltage characteristic.

A value of 65.80 nm for the thickness of the interfacial layer was found using C_{ox} value in Eq. (1).

However, due to the series resistance effect, we cannot obtain the actual value of the thickness. The series resistance can cause a serious error in the extraction of the interfacial properties. To avoid this error, a correction should be applied to the measured admittance before the desired information is extracted.^{4,12} The series resistance R_s and interfacial layer capacitance C_{ox2} for the MIS structure can be calculated from Equations (2-4):⁴

$$R_s = \left[\frac{G_{ma}}{(wC_{ma})^2 + G_{ma}^2} \right] \quad (2)$$

$$C_{ma} = \frac{C_{ox}}{1 + (wR_s C_{ox})^2} \quad (3)$$

$$C_{ox2} = C_{ma} \left[1 + \frac{C_{ma}^2}{(wC_{ma})^2} \right] \quad (4)$$

where $w = 2\pi f$ is the angular frequency of the *ac* signal and f is the frequency in Hz or s^{-1} . $C_{ma} = 422$ pF and $G_{ma} = 7.10 \times 10^{-3}$ F/s are the measured conductance and capacitance in the strong accumulation region in Figures 1a and 2. Eq. (4) was obtained from Equations (2) and (3). The C_{ox2} and R_s values were found as 3448 pF and 123 Ω from Equations (2) and (4) for the accumulation region, respectively. This corrected capacitance value of $C_{ox2} = 3448$ pF is eight times larger than the capacitance value of $C_{ox} = 422$ pF. A corrected value of 8.06 nm for the thickness of the interfacial layer SiO_2 was obtained using value of $C_{ox2} = 3448$ pF in Eq. (1). As can be seen from explained above, the series resistance completely masks interface trap loss, and especially the equivalent parallel conductance is much more sensitive to the series resistance than capacitance. Therefore, it can be said that the correction made considering the series resistance is particularly important in conductivity measurements.^{4,12,13-16}

The free carrier density was determined from the slopes of the C^{-2} - V curves obtained using Eq. (5) (Figure 3).

$$N_A = \frac{2}{q\epsilon_s\epsilon_0(dC^{-2}/dV)A^2} \quad (5)$$

Furthermore, the barrier height Φ_{CV} of the MIS diode from the C^{-2} - V curves can be determined using Eq. (6).

DOI: <http://dx.doi.org/10.32571/ijct.642886>

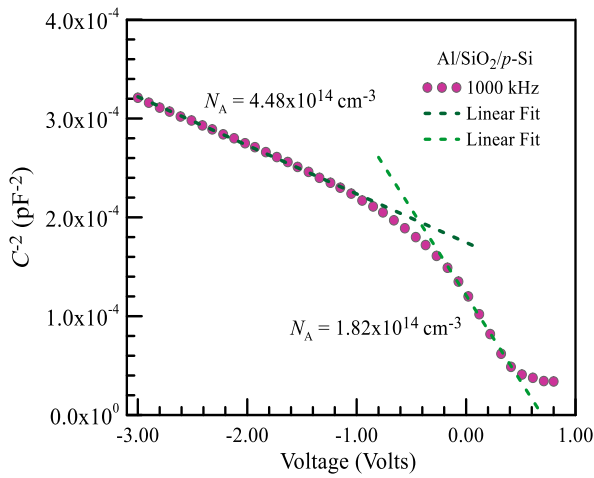


Figure 3. C^{-2} versus voltage curve at 1000 kHz and 300 K.

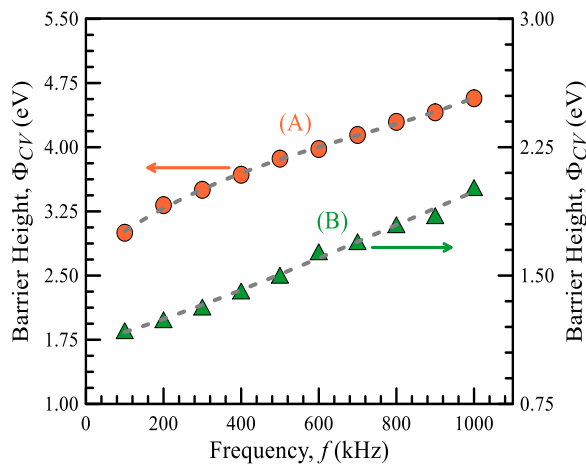


Figure 4. Barrier height versus frequency plot: a) The barrier height values from the C^{-2} - V curves corresponding to inversion region ranged from -1.0 V to -3.0 V of the C^{-2} - V curves at each frequency, b) The barrier height values calculated from the C^{-2} - V curves corresponding to the depletion region ranged from 0.0 V to -1.0 V at each frequency.

$$C^{-2} = \frac{2(V_{D0} + V_0)}{q\epsilon_s\epsilon_0 N_A A^2} \quad (6)$$

where q is the electronic charge, ϵ_s is dielectric constant of the semiconductor substrate, the diffusion potential is given by $V_{D0} = (\Phi_{CV} - V_p)$, V_p is the potential difference between Fermi level and the valance band maximum in the neutral region of p -type semiconductor in the energy band diagram of the metal/ p -type semiconductor rectifying contact, and it is stated by Eq. (7).

$$V_p = kT \ln \left(\frac{N_V}{N_A} \right) \quad (7)$$

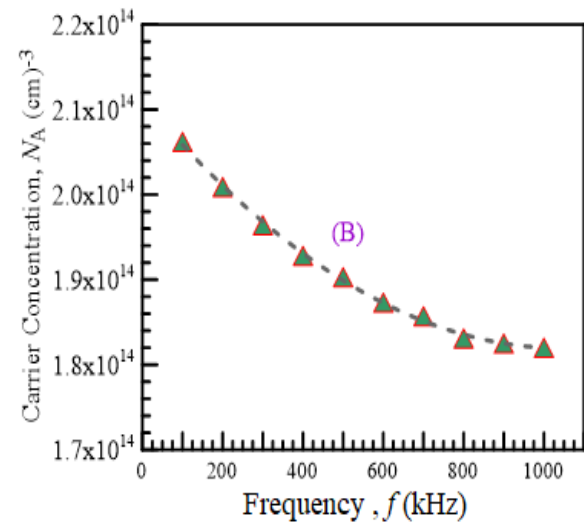
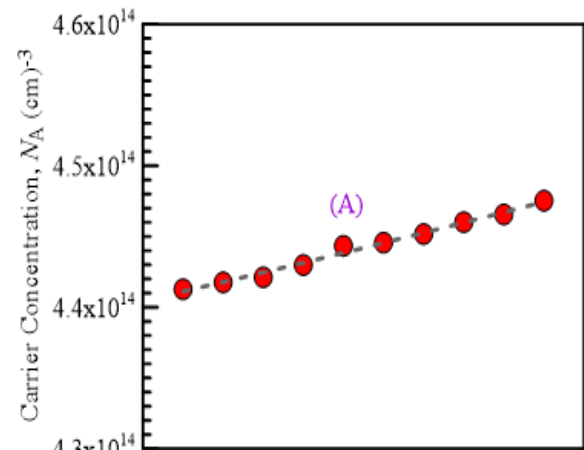


Figure 5. Carrier concentration versus frequency plots: a) from inversion region ranged from -1.0 V to -3.0 V of the C^{-2} - V curves at each frequency, b) from depletion region ranged from 0.0 V to -1.0 V of the C^{-2} - V curves at each frequency.

where $N_V = 1.04 \times 10^{19} \text{ cm}^{-3}$ is the state density in the valance band.¹²

Now let us consider the case when a still larger positive voltage is applied to the top metal gate of the MIS diode. A larger negative charge in the MIS diode indicates a larger induced space charge region. Thus, the surface of the p -type Si semiconductor is inverted from a p -type to an n -type semiconductor, and an inversion layer of electrons forms at the native oxide layer/semiconductor interface. This region corresponds to the part ranged from -1.0 V to -3.0 V of the C^{-2} - V curve in Figure 3. A majority carrier hole density of $4.48 \times 10^{14} \text{ cm}^{-3}$ was calculated from the inversion layer part of the C^{-2} - V curve using Eq. (5).

DOI: <http://dx.doi.org/10.32571/ijct.642886>

Again, let us deal with the C - V and G - V curves in Figures 1a and 2, the reverse branch case of the MIS diode, when a positive voltage is applied to the Al/SiO₂ side, that is, to the gate metal, with respect to the p -Si/Al side; a positive charge will exist on the top Al Schottky contact (gate metal) in this case, majority carrier holes will experience a force away from the native oxide layer/semiconductor interface. As the holes are pushed away from the Al/SiO₂ interface, a negative space charge induced depletion region is created because of the fixed ionized acceptor atoms. The depletion region ranges from 0.0 V to -0.6 V in Figure 4 which shows C^2 versus V curve at 1000 kHz and 300 K. The majority carrier holes density of the p -Si substrate can be from the part corresponding to the depletion region of the C^2 - V curve. A carrier concentration value of $1.82 \times 10^{14} \text{ cm}^{-3}$ was calculated from this part of the C^2 - V curve from Eq. (5).

A value of 0.25 V for V_p was obtained from the equation above. For example, the value of Φ_{CV} can be determined from the fit to the linear C^2 - V curve corresponding to depletion region in (0.0 V) – (-0.6 V) range in Figure 3. Thus, the intercept of the linear C^2 versus V plot with V axis was obtained as $V_0 = V_{D0} = 0.70 \text{ V}$, and $\Phi_{CV} = (V_p + V_{D0}) = 0.95 \text{ V}$. This calculation was repeated for the linear C^2 - V curve corresponding to depletion and inversion region at each frequency and thus, Figure 4 is plotted.

For the MOS devices, corrected capacitance and equivalent parallel conductance at a given frequency can be written as follows:⁴

$$C_c = \frac{[G_m^2 + (wC_m)^2]C_m}{(wC_m)^2 + a^2} \quad (8)$$

$$G_c = \frac{[G_m^2 + (wC_m)^2]C_m}{(wC_m)^2 + a^2} = \frac{(wC_cR_s)^2}{1 + (wC_cR_s)^2} \quad (9)$$

where $a = G_m - [G_m^2 + (wC_m)^2]R_s$ and C_m and G_m are the capacitance and the equivalent parallel conductance measured across the terminals of the MOS capacitor at each frequency, that is, C_m and G_m values come from the experimental C - V and G - V curves in Figures 6 and 8. Figures 7 and 9 illustrate the corrected and non-corrected experimental forward and reverse bias C - V and G - V characteristics at 500 kHz frequency and 300 K temperature, as an example, respectively.

The R_s value from the accumulation region using Eq. (2) at each frequency is used in these calculations. The absence of a peak in the non-corrected G - V curves means that the series resistance produced the dominant loss and completely masked the interface trap loss. The series resistance effect are clearly apparent in Figures 7 and 9, and the greatest error in the capacitance occurs in

accumulation and a portion of the depletion region.^{4,12,13-17} As can be seen, it is not possible to neglect series resistance in each case. Therefore, the series resistance must be measured and applied as a correction to the measured admittance.^{4,12,13-17}

The following Hill-Coleman equation¹³ was used to determine the density distribution of the interface states,

$$N_{ss} = \frac{2}{qA} \frac{(G/\omega)_m}{\{[(G/\omega)_m/C_{ox2}]^2 + (1 - C_m/C_{ox2})^2\}} \quad (10)$$

where C_m and G_m/ω are the measured or experimental capacitance and conductance peak values at given each frequency.

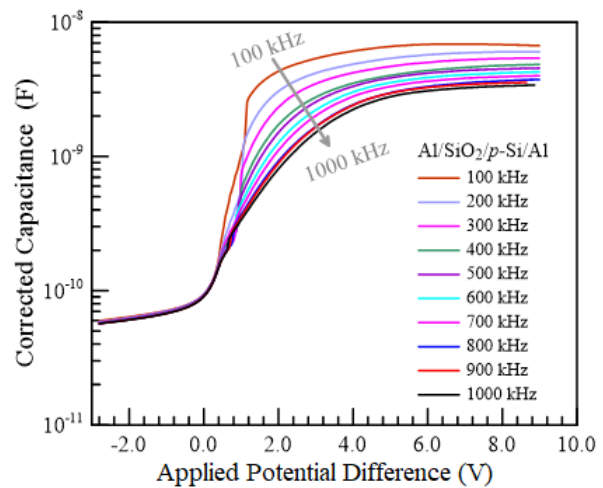


Figure 6. Corrected capacitance versus voltage curves at different frequencies and 300 K.

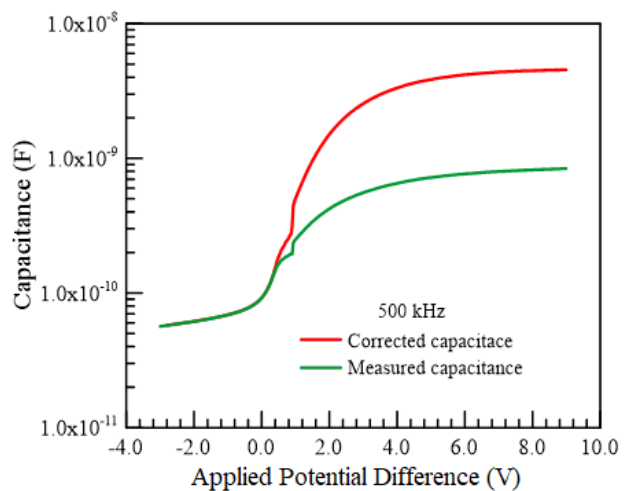


Figure 7. Corrected and uncorrected or measured capacitance versus voltage curves at 500 kHz and 300 K.

DOI: <http://dx.doi.org/10.32571/ijct.642886>

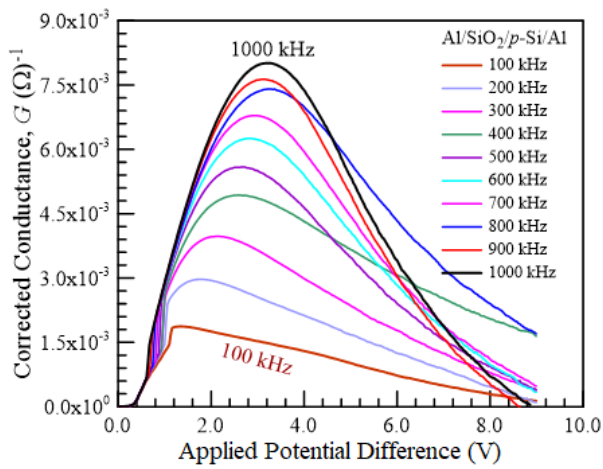


Figure 8. Corrected conductance versus voltage curves at different frequencies and 300 K.

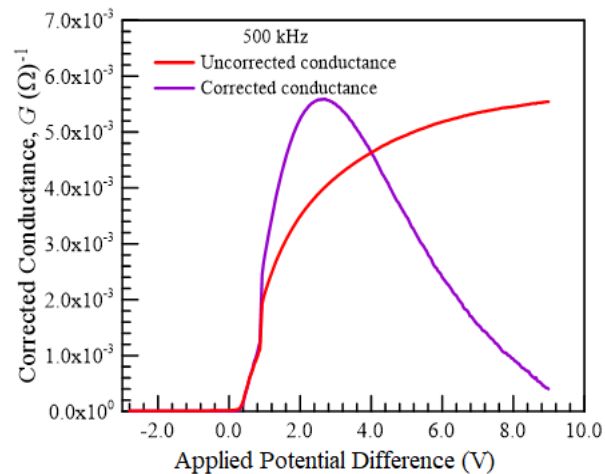


Figure 9. Corrected and uncorrected conductance versus voltage curves at 500 kHz and 300 K.

The oxide layer capacitance C_{ox2} is the value calculated from Eq. (4). Frequency dependent interface state density distribution, N_{ss} , plot is presented in Figure 10 and it can be seen that the N_{ss} depends strongly on the frequency. As can be seen from Figure 10, the N_{ss} increases with decreasing frequency because it can follow the ac signal and it contributes capacitance values in low frequencies. It can be clearly from Figure 3 that the capacitance has higher value in lower frequency than that in the higher frequencies. Hence, this confirms that the high capacitance in lower frequencies can be attributed to

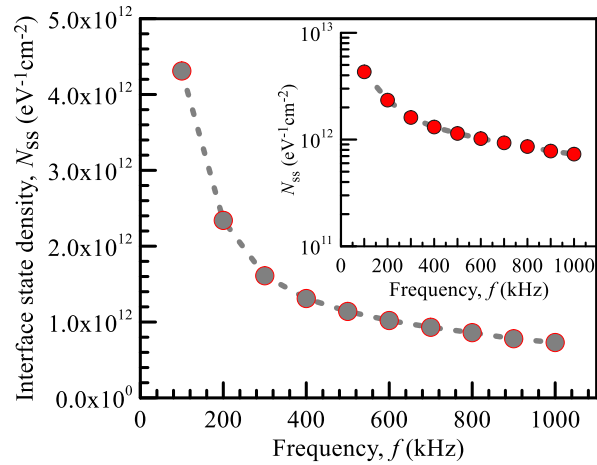


Figure 10. Interface state density versus frequency curves at 300 K, inset: The same plot is shown in semi-logarithmic scale.

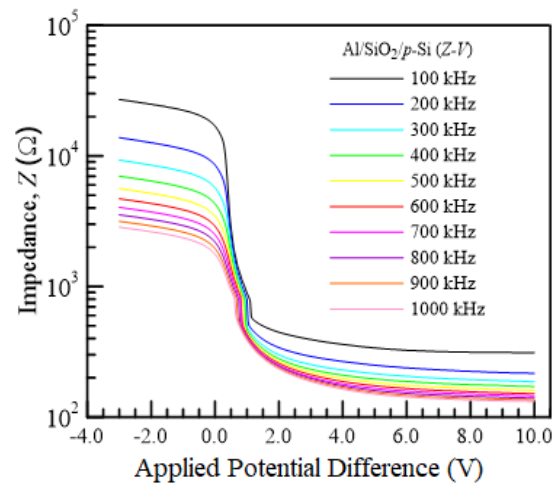


Figure 11. Frequency induced Impedance-Voltage characteristics of the diode.

excess capacitance resulting from the N_{ss} values.^{4,12,13-17} Thereby, interface state density decreased from $4.31 \times 10^{12} \text{ eV}^{-1} \text{ cm}^{-2}$ at 100 kHz to $7.30 \times 10^{11} \text{ eV}^{-1} \text{ cm}^{-2}$ at 1000 kHz. Figure 11 illustrates frequency induced impedance (Z) versus voltage characteristics of the Al/SiO₂/p-Si/Al MIS diode. The impedance of a circuit is described as the ratio of the phasor voltage and the phasor current measured in ohms. We note that the impedance modulus is so high under reverse-bias. The impedance of the device increased with decreasing frequency at a given voltage.

DOI: <http://dx.doi.org/10.32571/ijct.642886>

4. CONCLUSIONS

The majority carrier density corresponding to the depletion and inversion parts of the C^2 - V curve, at 1000 kHz, for the Al/SiO₂/p-Si/Al MIS diode has been determined 1.82×10^{14} and $4.48 \times 10^{14} \text{ cm}^{-3}$, respectively. The fact that the carrier density from the inversion part becomes more than that from the depletion part may be attributed to increase of the negative space charge density in the depletion region due to the charges in the inversion region that the surface of the p -type Si semiconductor is inverted from a p -type to an n -type semiconductor. The value of Φ_{CV} can be determined a value of 0.95 V. With an increase in frequency, interface state density decreased from $4.31 \times 10^{12} \text{ eV}^{-1} \text{ cm}^{-2}$ at 100 kHz to $7.30 \times 10^{11} \text{ eV}^{-1} \text{ cm}^{-2}$ at 1000 kHz, since the interface charges cannot obey the ac signal and cannot contribute to capacitance values in high frequencies.

Conflict of interests

Authors declare that there is no a conflict of interest with any person, institute, company, etc.

REFERENCES

1. Hlali, S.; Farji, A.; Hizem, N.; Militaru, L.; Kalboussi, A.; Souifi, A. *J. Alloys Compd.* **2017**, 713, 194-203.
2. Karabulut, A.; Orak, I.; Turut, A. *Int. J. Chem. Technol.* **2018**, 2 (2), 106-112.
3. Kumar, V.; Kaminski, N.; Maan, A.S.; Akhtar, J. *Phys. Status Solidi A.* **2016**, 213 (1) 193-202.
4. Nicollian, E. H.; Bews, J. R. *MOS (Metal Oxide Semiconductor) Physics and Technology*, A.Wiley-Interscience Publication, John Wiley & Sons, New York, 1982.
5. Karabulut, A. *Bull. Mater. Sci.* **2019**, 42:5.
6. Altindal, Ş.; Asar, Y. Ş.; Kaya, A.; Sonmez, Z. *J. Optoelectron. Adv. Mater.* **2012**, 14 (11-12), 998-1004.
7. Turut, A.; Yalcin, N.; Saglam, M. *Solid State Electron.* **1992**, 35 (6), 835-841.
8. Bati, B.; Nuhoglu, C.; Saglam, M.; Ayyildiz, E.; Turut, A. *Phys. Scripta.* **2000**, 61, 209-212.
9. Cetinkaya, A. O.; Kaya, S.; Aktag, A.; Budak, E.; Yilmaz, E. *Thin Solid Films* **2015**, 590, 7-12.
10. Cetinkara, H. A., Turut, A., Zengin, D. M.; Erel, S. *Appl. Surf. Sci.* **2003**, 207190-207199.
11. https://en.wikipedia.org/wiki/RCA_clean
12. Sze, S. M. *Physics of Semiconductor Devices*, 2nd Ed., John Wiley & Sons, Inc. New York, 1981.
13. Hill, W.; Coleman, C. *Solid-State Electron.* **1980**, 23 (9), 1987-1993.
14. Neamen, D. A. *Semiconductor Physics and Devices*, Irwin, Boston, 1992.
15. Manthrammel, M. A.; Yahia, I. S.; Shkira, M.; AlFaify, S.; Zahran, H. Y.; Ganesh, V.; Yakuphanoglu, F. *Solid State Sci.* 2019, 93, 7-12.
16. Turut, A.; Karabulut, A.; Ejderha, K.; Bıyıklı, N. *Mater. Sci. Semicond. Process.* **2015**, 39, 400-407.
17. Kim, C. H.; Yaghmazadeh, O.; Tondelier, D.; Jeong, Y. B.; Bonnassieux, Y.; Horowitz, G. *J. Appl. Phys.* **2011**, 109, 083710.

ORCID

 <https://orcid.org/0000-0002-4002-7967> (M. C. Ozdemir)

 <https://orcid.org/0000-0003-1740-1444> (O. Sevgili)

 <https://orcid.org/0000-0003-2318-9718> (I. Orak)

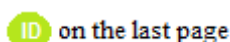
 <https://orcid.org/0000-0002-4664-4528> (A. Turut)



Adsorption of basic red 2 dye by activated biomass charcoal in batch and column systems

Bilal ACEMİOĞLU^{1,*}, Neslihan KARATAŞ¹, Melike Hilal GÜLER¹, Murat ERTAŞ²,

Mehmet Hakkı ALMA³



¹Department of Chemistry, Faculty of Science and Arts, Kilis 7 Aralık University, 79000, Turkey

²Department of Forest Industry Engineering, Faculty of Forestry, Bursa Technical University, 16310, Turkey

³Department of Forest Industry Engineering, Faculty of Forest, Kahramanmaraş Sutcu Imam University, 46060/Rectorate of Iğdır University, Iğdır, 76000, Turkey

Received: 24 November 2019; Revised: 09 December 2019; Accepted: 10 December 2019

*Corresponding author e-mail: acemioğlu@kilis.edu.tr

Citation: Acemioğlu, B.; Karataş, N.; Güler, M. H.; Ertaş, M.; Alma, M. H. *Int. J. Chem. Technol.* 2019, 3 (2), 136-145.

ABSTRACT

Activated biomass charcoal produced from peanut shells was utilized as an adsorbent for the removal of basic red 2 (BR2) dye from aqueous solution in batch and column systems. In batch system, the effects of shaking time, initial BR2 concentration, solution pH and temperature on the adsorption were studied. While the adsorption was increasing with increasing contact time, initial BR2 concentration and temperature, it decreased with increasing solution pH. In column system, the effects of solution flow rate and initial BR2 concentration were investigated. The adsorption of BR2 was determined between 82.40 and 99.91% under all conditions such as concentration, temperature and pH for batch system. The column adsorption was found as 99.50%. Adsorption obeyed the Freundlich isotherm and the pseudo-second order kinetic model. SEM and FT-IR studies indicated that a surface adsorption might probably be occurred on the heterogeneous surface of activated biomass charcoal.

Keywords: Peanut shell charcoal, basic red 2, adsorption, column.

Bazık kırmızı 2 boyasının kesikli ve kolon sistemlerinde aktifleştirilmiş biyokütle kömürü tarafından adsorpsiyonu

ÖZ

Yerfıstığı kabuklarından üretilen aktifleştirilmiş biyokütle kömürü, kesikli ve kolon sisteminde bazık kırmızı 2 (BR2) boyasının sulu çözeltiden uzaklaştırılması için bir adsorbent olarak kullanıldı. Kesikli sistemde adsorpsiyon üzerine çalkalama süresi, başlangıç BR2 konsantrasyonu, çözelti pH'sı ve sıcaklığın etkileri incelendi. Adsorpsiyon temas süresi, başlangıç BR2 konsantrasyonu ve sıcaklık ile artarken artan çözelti pH'sı ile azaldı. Kolon sisteminde çözelti akış hızı ve başlangıç BR2 konsantrasyonunun etkileri incelendi. Kesikli sistem için, konsantrasyon, sıcaklık ve pH gibi tüm şartlar altında BR2 adsorpsiyonu %82.40 ve %99.91 arasında belirlendi. Kolon adsorpsiyonu ise %99.50 olarak bulundu. Adsorpsiyon Freundlich izotermi ve sözde ikinci dereceden kinetik modele uyum gösterdi. SEM ve FT-IR incelemeleri, aktifleştirilmiş biyokütle kömürün heterojen yüzeyinde bir yüzey adsorpsiyonunun meydana gelmiş olabileceğine işaret etti.

Anahtar Kelimeler: Yerfıstığı kabuğu kömürü, bazık kırmızı 2, adsorpsiyon, kolon.

1. INTRODUCTION

Matrix structural molecules comprising lignin, cellulose and hemicellulose are known as lignocellulosic materials. Such substances generally constitute the class of forest origin and agricultural wastes. For example, tree

barks,¹⁻⁴ tree leaves/leaves,⁵⁻⁷ wood sawdust,⁸⁻¹² fruit peels/shell,¹³⁻¹⁶ pirina or olive oil wastes/olive pomace/olive stone,¹⁷⁻²¹ shells of hard-shelled fruits such as walnut, almond, hazelnut,²²⁻²⁴ husks and straws of cereals such as wheat, barley,²⁵ peanut shell,²⁶⁻²⁹

vineyard pruning wastes,³⁰ are agricultural lignocellulosic waste materials. As alternative to activated carbon, these materials have commonly been used as adsorbents in removing the metals and dyes from aqueous medium. Of these low cost waste materials, with use of peanut shell, some works have been reported for metal and dye adsorption in the literature. For instance, peanut shell pretreated with HCl has been utilized as an adsorbent for remazol brilliant blue R removal.³¹

For instance, basic red 2 (BR2) adsorption by peanut shell has been worked by Sakalar and co-workers.²⁷ In another study, peanut shell has been utilized as an adsorbent for remazol orange RGB removal from aqueous solution.²⁸ On the other hand, some alternative materials produced from peanut shell have also been used as adsorbents for dye adsorption. For example, polyurethane-type foam fabricated from peanut shell has been utilized for the sorption of remazol brilliant blue R³² and safranin-O dyes³³ Moreover, sodium hydroxide-activated biochar produced from peanut shell has been used as an adsorbent for remazol orange RGB removal.³⁴ Herein, activated biomass charcoal produced from peanut shell has been utilized as an adsorbent to remove BR2, a cationic dye, from aqueous medium by adsorption. Such a study has not been done before, and therefore this work is original. The effects of shaking time (ie. the contact time of adsorbent with dye solution), initial dye concentration, pH and temperature on the adsorption process have been studied. Moreover, column adsorption study, SEM and FT-IR analyses has also been performed. All results obtained have been interpreted in detail.

2. MATERIALS AND METHODS

2.1. Materials

2.1.1. Adsorbent charcoal

Peanut shell wastes as raw material for the production of adsorbent charcoal were taken from Osmaniye province of Turkey. Firstly it was washed and dried in an oven. Then, the dried peanut shells were powdered by a crusher and sieved throughout a 100-mesh molecular sieve for charcoal production.

2.1.2. Adsorbate BR2

Basic red 2 (BR2), color index 50240, was provided from Carlo Erba, and it was used as taken in the adsorption experiments. BR2 is a positively charged cationic dye and it has a molecular mass of 350.85 g/mol. The synonym name of this dye is safranin-O³⁵ or safranin T.³⁶ Its UPAC name is 3,7-diamino-2,8-dimethyl-5-phenylphenazinium chloride.³⁶ The spectral analysis of BR2 was recorded on a UV-Vis spectrophotometer, and

its absorption spectra recorded for various concentrations are presented (Figure 1). As seen from this figure, the maximum absorbance wavelength of BR2 is 517-520 nm. The molecular structure of BR2 is presented in Figure 2. Some physical properties of BR2 are given elsewhere.^{27,33}

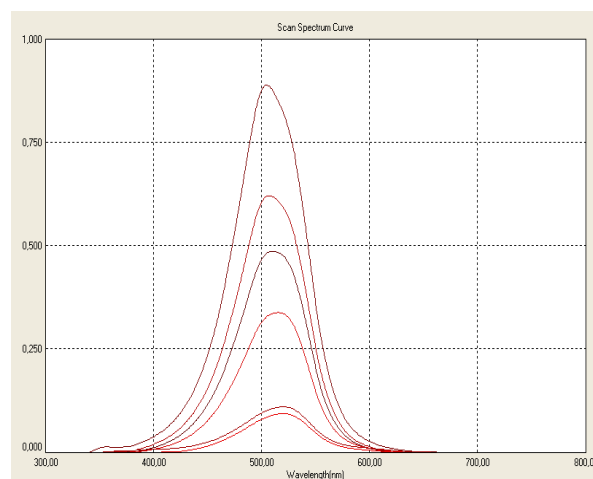


Figure 1. UV-Vis spectra of BR2 (top to bottom concentrations: 150 mg l⁻¹, 100 mg l⁻¹, 75 mg l⁻¹, 50 mg l⁻¹, 20 mg l⁻¹, and 10 mg l⁻¹).

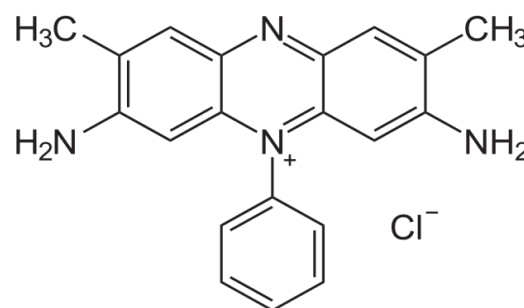


Figure 2. The molecular structure of BR2.

2.1.2.1 Preparation of BR2 solutions

500 mg l⁻¹ stock solution of BR2 was prepared using distilled water. The desired concentrations of BR2 were prepared from the stock. Solution pHs were adapted with diluted HCl and NaOH solutions by a pH meter.

2.2. Methods

2.2.1. Production of the activated biomass charcoal

In this section, firstly charcoal was produced and then the charcoal was activated chemically. The biomass charcoal was produced from peanut shell wastes using pyrolysis system.

This system designed for coal production was manufactured in the industry and shown schematically in Figure 3. The biomass charcoal are produced as stated in our another study.³⁴ Then biomass charcoal obtained was activated chemically as described in the following.

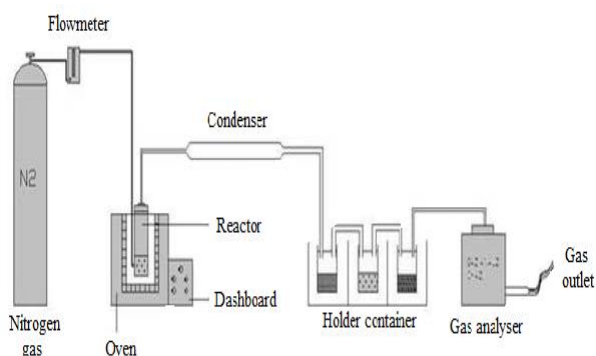


Figure 3. Schematic representation of the pyrolysis system designed for charcoal production.

2.2.1.1. Activation of the biomass charcoal

The biomass charcoal obtained was activated chemically because it did not well adsorb BR2 dye. For this purpose, the biomass charcoal was activated using 1 N NaOH solution as described elsewhere.³⁴ The obtained activated biomass charcoal stored for adsorption experiments.

2.2.3. Characterization of the activated biomass charcoal

Characterization of the activated biomass charcoal was conducted by scanning electron microscopy (SEM), Fourier Transformed Infrared (FT-IR), elemental analyzer, and specific surface area and porosity analyzer. The composition content of the biomass charcoal was performed by an elemental analyzer (LECO CHNS-932 analyzer). Functional groups of the biomass charcoal were determined using a FT-IR spectrophotometer (FTIR RX-1 Perkin Elmer ATR spectrophotometer). Surface morphology of the charcoal was recorded by a SEM (LEO 435 VP SEM). Specific surface area and porosity were measured by a N₂ gas adsorption device (Micromeritics Instrument Corporation).

2.3. Adsorption Experiments

The experiments were conducted by adding 0.25 g of the activated biomass charcoal to 50 ml of BR2 solution in 250-ml erlenmeyers in a temperature-controlled

shaking water bath for different initial BR2 concentrations, temperatures and pHs and at various shaking times at 130 rpm. Following the estimated shaking times, the samples were taken from shaking water bath and centrifuged. After centrifugation, the supernatants were analyzed at 517 nm (maximum wavelength) on T80UV-Vis spectrophotometer.

The percent adsorption (PA) of BR2 from aqueous solution was determined using Eq. (1).

$$PA = \frac{(C_0 - C_t)}{C_0} \times 100 \quad (1)$$

The amount of BR2 removed by the activated biomass charcoal was estimated from Eq. (2).

$$q_t = \frac{(C_0 - C_t) V}{m} \quad (2)$$

where, q_t refers the adsorbed BR2 amount per unit adsorbent mass at any time (in mg g⁻¹). C_0 and C_t show the initial dye concentration and the adsorbed BR2 concentration on the adsorbent at any time (in mg l⁻¹), respectively. V shows the working volume of BR2 solution (in liter), and m indicates mass of the activated biomass charcoal (in gram). At the equilibrium time, $C_t = C_e$ and $q_t = q_e$. C_e is the unadsorbed BR2 concentration in solution at equilibrium time (in mg l⁻¹). q_e indicates the adsorbed BR2 amount per unit of adsorbent mass at the equilibrium time (mg dye per g adsorbent).

2.4. Experimental parameters on the adsorption

2.4.1. Shaking time effect

Shaking times on the adsorption of BR2 by the activated biomass charcoal were selected as 1, 2, 3, 4, 5, 10, 20, 30, 45, 60, 75, 100 min under all experimental parameters in terms of initial dye concentrations, pHs and the temperatures.

2.4.2. Initial dye concentration effect

The initial concentrations on BR2 adsorption by the activated biomass charcoal were selected as 10, 20, 50, 75, 100 and 150 mg l⁻¹ at, 40°C, pH 3 and 130 rpm.

2.4.3. pH effect

The values of solution pH on BR2 adsorption by the activated biomass charcoal were adapted between 3 and 9 for 150 mg l⁻¹ initial concentration at 40°C and 130 rpm. pHs of BR2 solutions were adjusted with dilute sodium hydroxide and hydrochloric acid solutions by a pH meter.

2.4.4. Temperature effect

The temperatures on BR2 adsorption by the activated biomass charcoal were worked between 20 and 60°C for 150 mg l⁻¹ initial concentrations at pH 3 and 130 rpm.

2.5. Column adsorption

Column adsorption works was carried out for the initial concentrations between 10 and 150 mg l⁻¹ at pH 3 and 23°C (at room temperature). The flow rate of BR2 solution was 21 ml h⁻¹.

3. RESULTS AND DISCUSSION

3.1. Characterization of the activated biomass charcoal

3.1.1. Elemental analysis, specific surface area and porosity

As given in our another study,³⁴ the elemental analysis results of the activated biomass charcoal indicate that the activated carbon include 50.34% C, 4.280% H, 2.911% N, and 0.524% S. Specific BET surface area was as found 1.599 m² g⁻¹, and porosity was 0.00195 cm³ g⁻¹.

3.1.2. SEM analysis

The SEM photographs before and after the adsorption are illustrated in Figure 4. As seen from Figure 4a, the surface of the activated carbon is rough, indented and protruding, namely the surface is heterogeneous. After the adsorption of the dye, any change in the heterogeneous structure of the activated biomass charcoal does not occur. Only the surface has become with more blurred image due to dye adsorption (see Figure 4b).

3.1.3. FTIR analysis

FT-IR spectra of the biomass charcoal, the activated biomass charcoal and dye-adsorbed activated biomass charcoal are shown in Figure 5.

The broad band at 3294.84 cm⁻¹ refers -OH groups of glucose and -NH groups of proteins.³⁸ The strong absorption band at 2926.42 indicates aliphatic C-H vibrations.³⁹ After the biomass charcoal was activated with NaOH, the broad band at 3294.84 cm⁻¹ significantly shifted to 3222.09 cm⁻¹ and its intensity remarkably rose. After activation, the peak intensity at 2926.42 cm⁻¹ declined. The peaks at 1434.98 and 1373.71 cm⁻¹ indicate the C = O stretching of carboxylic groups.⁴⁰ After the activation, the peak at 1434.98 diminished. The peak at 1373.71 cm⁻¹ very slightly shifted to 1373.61 cm⁻¹, but this peak broaden and its intensity remarkably ascended. The band at 1574.65 cm⁻¹ probably indicates aromatic C - C stretching.³⁴ After the activation and dye adsorption this peak did not change. After the adsorption

two strong new peaks at 2117.20 and 1216.97 cm⁻¹ occurred. The band at 2117.20 cm⁻¹ probably indicates C = C stretching due to the structure of the dye after the adsorption. Band at 1216.97 cm⁻¹ probably shows C-H stretching in the structure of the dye.³⁴ After the activation, a new band at 1065.16 cm⁻¹ appeared. This band probably refers to the out of-plane bending for carbonates in the activated biomass charcoal.⁴¹ After BR2 adsorption, this band greatly shifted to 1013 cm⁻¹. The peaks at < 1000 cm⁻¹ indicate fingerprint zone resulted from sulfur or phosphate,²⁷ and these peaks did not almost change after the carbonization and the dye adsorption. FT-IR results imply that a chemical interaction may have taken place between the functional groups on the surface of the activated biomass charcoal and positively charged BR2 molecules.

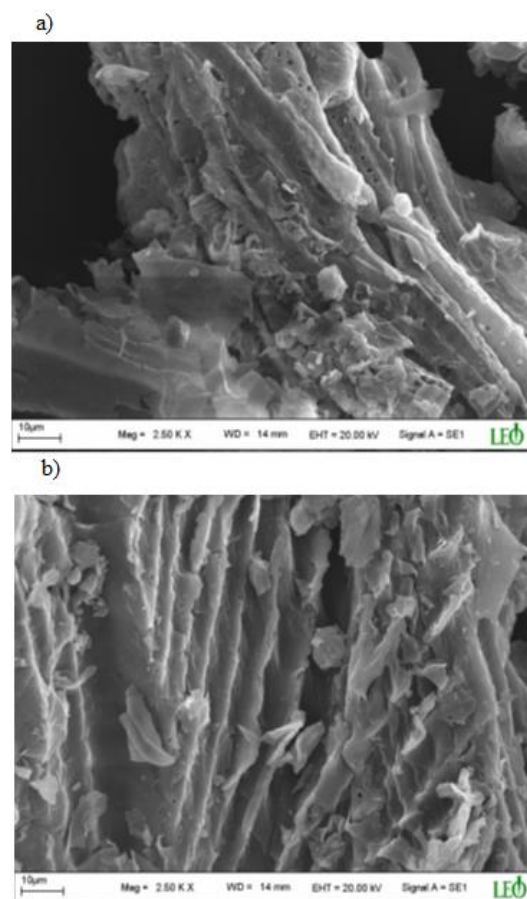


Figure 4. The SEM images, a) the activated biomass charcoal before adsorption, b) dye-adsorbed activated biomass charcoal after adsorption.

3.2. Shaking time effect and the adsorption equilibrium time

Effect of shaking time on BR2 adsorption was studied for different initial BR2 concentration, pH and temperature at different shaking times. The maximum adsorption was attained at 5 min under all the experimen-

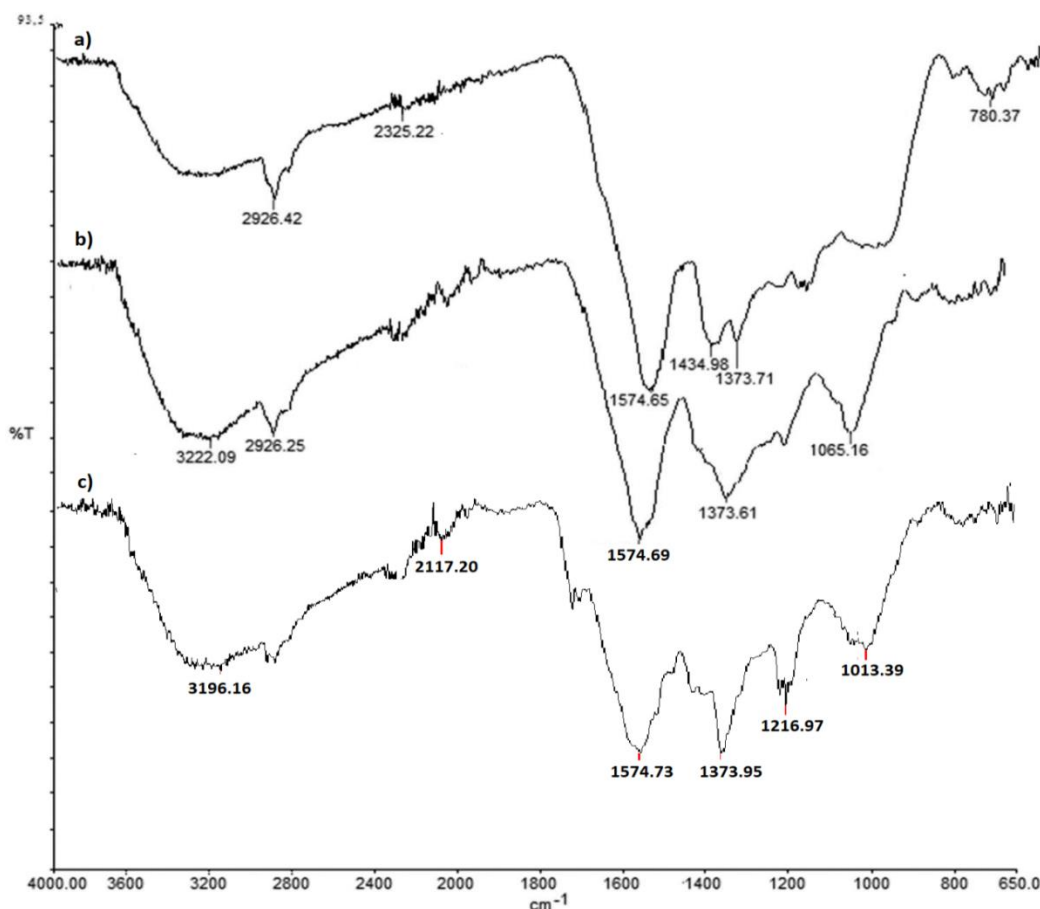


Figure 5. FT-IR spectra: a) the biomass charcoal, b) the activated biomass charcoal, c) dye-adsorbed activated biomass charcoal.

tal conditions. After 5 min, any increase in the adsorption did not observe. Therefore, the equilibrium time of the adsorption was determined as 5 min.

3.3. Initial dye concentration effect

Figure 6 demonstrates the effect of initial dye concentration on the adsorption. As seen from the figure, it was determined that BR2 was highly adsorbed by the activated biomass charcoal from the first minutes and reached the maximum level at 5 min. There was no change in the adsorption after 5 min. The maximum adsorption (ie. adsorbent capacity) at 5 min was found as 1.958 mg g⁻¹ (97.93%), 3.903 mg g⁻¹ (97.59%), 9.913 mg g⁻¹ (99.13%), 14.826 mg g⁻¹ (98.84%), 19.853 mg g⁻¹ (99.26%), and 29.868 mg g⁻¹ (99.56%) for all concentrations between 10 and 150 mg l⁻¹, respectively. This refers a very rapid interaction between the activated biomass charcoal and BR2 molecules. In addition, it was observed that the red color of BR2 completely disappeared and became clear from the first minute. This situation was also observed in pH and temperature

studies. A similar situation has been observed for BR2 adsorption onto peanut shell.²⁷

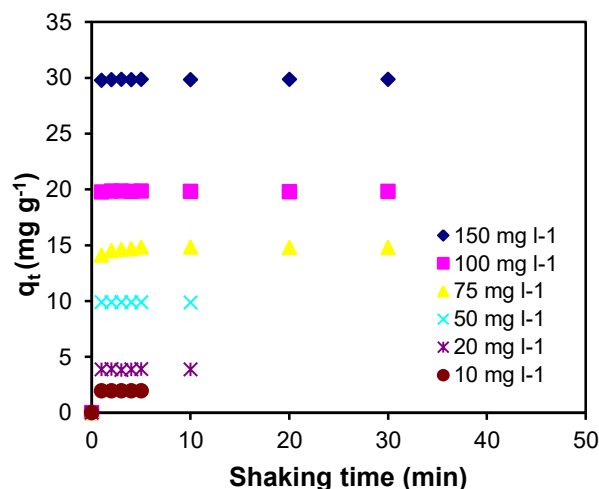


Figure 6. The effect of initial BR2 concentration on the adsorption (pH: 3, T: 40°C, w/v: 0.25g/50 ml).

3.4. pH effect

Figure 7 illustrates pH effect on BR2 adsorption by the activated biomass charcoal.

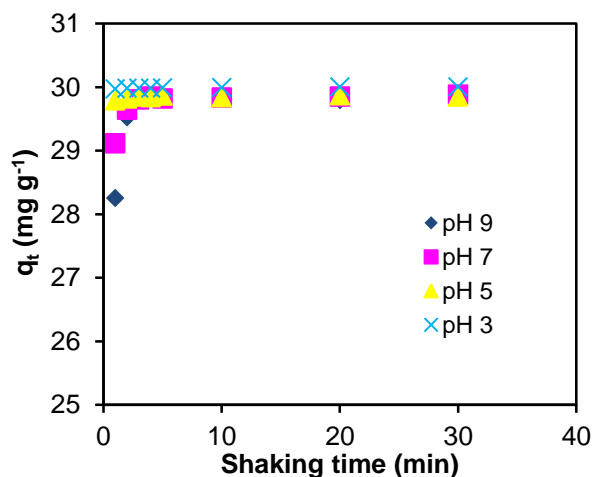


Figure 7. pH effect on BR2 adsorption (C_0 : 150 mg l⁻¹, T: 40°C, w/v: 0.25g/50 ml).

As seen from Figure 7, a very high adsorption was observed at all pH values from the first minutes and it was observed that it reached the maximum level at 5 min. The maximum adsorption (i.e. the adsorbent capacity) at pH 3, 5, 7 and 9 within 5 min was determined as 29.983 mg g⁻¹ (99.91%), 29.864 mg g⁻¹ (99.54%), 29.817 mg g⁻¹ (99.39%) and 29.874 mg g⁻¹ (99.58%), respectively. It was considered that it was suitable to study at any pH value, since the adsorbed amounts at each pH were very high and very close to each other. As seen from this figure, it was observed that pH had no effect on the maximum adsorption.

3.5. Temperature effect

Figure 8 demonstrates temperature effect on BR2 adsorption by the activated biomass charcoal. From this figure, it is seen that the maximum adsorption slightly rise with increasing the temperature. The most adsorption was observed to occur at 60°C. While the adsorption in the first min at 20 and 30°C was 12.42 mg g⁻¹ (82.84%) and 13.17 mg g⁻¹ (87.86%), the maximum adsorption (i.e. the adsorbent capacity) was found as 14.89 mg g⁻¹ (99.65%) and 14.89 mg g⁻¹ (99.28%) in 5 min, respectively. On the other hand, the adsorption within the first 5 min at 40, 50 and 60°C was very close to each other and the maximum adsorption was reached within 5 min. The maximum adsorption (i.e. the adsorbent capacity) at 40 and 60°C was estimated as 29.86 mg g⁻¹ (99.56%) and 29.94 mg g⁻¹ (99.80%), respectively. The maximum adsorption at 40°C

and 60°C are very close to each other, and the maximum adsorption are determined as 14.84 mg g⁻¹ (98.84%) and 14.94 mg g⁻¹ (99.60%), respectively.

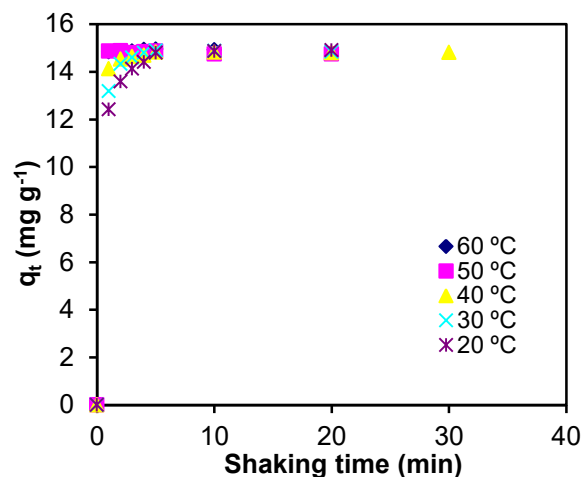


Figure 8. Temperature effect on BR2 adsorption (C_0 : 150 mg l⁻¹, pH: 3, w/v: 0.25g/50 ml).

3.6. Column adsorption study

The operating conditions for the column adsorption are summarized in Table 1. The system was operated at 23°C and pH 3. As can be seen from this table, a glass column with 1 cm diameter and 20 cm length was used for the continuous adsorption system. 2 g dry weight of activated biomass charcoal particles were packed between two layers of glass wool in the column. BR2 solution with the predetermined concentrations was fed through the top of the column. The flow rate of feed solutions was regulated as 0.35 ml min⁻¹ (21 ml h⁻¹). The dye samples passed through the column were collected from the bottom of the column at specific times. The samples from the outlet of the column were analyzed by UV-Vis spectrophotometer. The values of percent adsorption of BR2 by the column are shown in Figure 9.

Table 1. Column operating conditions

Column diameter, cm	1
Column length, cm	20
Height of bed, cm	10
Packing size, mesh	100
Flow rate, ml h ⁻¹	21
Concentration, mg l ⁻¹	10-150
Temperature, °C	23
Solution pH	3

Table 2. Kinetic parameters

		Intra-particle diffusion			Pseudo-first order kinetics			Pseudo-second order kinetics		
C_0	q_e (exp)	k_i	r^2	C	q_1	k_1	r^2	q_2	k_2	r^2
(mg l ⁻¹)	(mg g ⁻¹)	(mg g ⁻¹ min ^{-1/2})			(mg g ⁻¹)	(min ⁻¹)		(mg g ⁻¹)	(mg g ⁻¹ min ⁻¹)	
10	1.95	0.0018	0.0354	1.9575	0.003	0.03	0.002	1.95	523.05	1
20	3.90	0.0091	0.0137	3.8861	0.017	0.03	0.001	3.87	111.02	0.999
50	9.91	0.0043	0.0472	9.9113	0.004	0.05	0.004	9.91	11.31	1
75	14.82	0.5571	0.8905	13.638	1.015	0.52	0.943	14.88	1.32	1
100	19.85	0.0651	0.5632	19.719	0.063	0.39	0.291	19.84	25.40	1
150	29.86	0.0582	0.8063	29.734	0.101	0.43	0.598	14.02	14.02	1

As seen from Figure 9, the column adsorption of BR2 was determined to be between 99.17 and 99.47% for all the concentrations. Besides it was observed that all the outlet samples are colourless and cleared off the red colour of BR2. This situation indicates a high affinity between the functional groups of BR2 molecules and activated biomass charcoal packed in column. Column exhaustion time was determined as 15.5 h. When the flow rate is doubled (ie. 0.70 ml min⁻¹ (42 ml h⁻¹)), the adsorption was found to be 99.50%. At the same time, when the flow rate is worked as 0.70 ml min⁻¹, the accumulation of dye solution in the column was observed. Therefore, it was seen that an increase in the flow rate had no effect on the column adsorption. Based on this, the flow rate was not further increased.

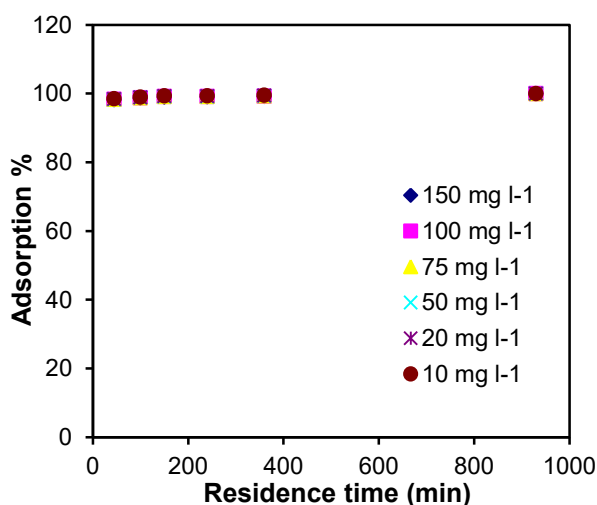


Figure 9. Initial BR2 concentration effect on the column adsorption. (C_0 : 150 mg l⁻¹, pH: 3, w: 2 g, v: 50 ml, flow rate: 21 ml h⁻¹).

3.7. Kinetic study

Adsorption kinetics was examined according to three commonly used models. The intra-particle diffusion model suggested by Weber and Morris is given in Eq. (3).⁴²

$$q_t = k_i t^{1/2} + C \quad (3)$$

The pseudo-first order kinetic model proposed by Lagergren is presented in Eq. (4).⁴³

$$\log (q_e - q_t) = \log q_1 - \frac{k_1}{2.303} t \quad (4)$$

The pseudo-second order kinetic model put forward by Ho and McKay is given in Eq. (5).⁴⁴

$$\frac{t}{q_t} = \frac{1}{k_2 q_2^2} + \frac{1}{q_e} t \quad (5)$$

where, k_i implies the intra-particle diffusion rate constant. k_1 and k_2 indicate the rate constants for the pseudo-first and -second order models, respectively. q_t and q_e indicate the amounts adsorbed of BR2 per unit of the adsorbent at any time and equilibrium time, respectively. The term $k_2 q_2^2$ indicates initial adsorption rate and is represented with h . All kinetic studies were conducted for the initial BR2 concentrations between 10 and 150 mg l⁻¹ at pH 3 and 40°C. The obtained all kinetic parameters are submitted in Table 2.

Firstly, the plots of q_t against $t^{1/2}$ for the intra-

particle diffusion were obtained. The values of coefficient of determination (r^2) from the linear regression analysis of the plots obtained were determined as 0.0354, 0.0137, 0.0472, 0.8975, 0.5632, and 0.8063 for the initial concentrations of 10, 20, 50, 75, 100, and 150 mg l⁻¹, respectively. These low values show that the adsorption does not follow the intra-particle diffusion model. Due to the low r^2 values, the plots are not given here. However, due to the surface adsorption, the boundary layer thickness (the value C) was determined to be rose with increasing initial dye concentration (see Table 2).

Secondly, the plots of $\log(q_e - q_t)$ against t for the pseudo-first order model were drawn. The values of the r^2 from the linear regression analysis of the plots were found as 0.0026, 0.0013, 0.0045, -0.9435, 0.2916, and 0.5989 for the initial concentrations of 10, 20, 50, 75, 100, and 150 mg l⁻¹, respectively. As seen, the r^2 values are very low. Also, there is no any harmony between the experimental adsorption capacities (q_{exp}) and theoretical adsorption capacities (q_i) from the pseudo-first order model. Therefore, the adsorption is not consistent with the pseudo-first order kinetic model. Due to low r^2 values, the plots are not given here. Finally, the linear plots of t/q_t against t for the pseudo-second order model were drawn (see Figure 10).

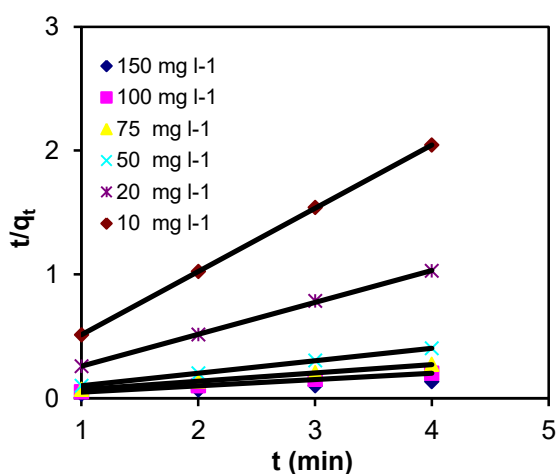


Figure 10. Concentration effect on the pseudo-second order kinetics.

From the regression analyses above, the values of the r^2 are very high. The values of r^2 are 1 for all initial concentrations between 10 and 150 mg l⁻¹ (except for 20 mg l⁻¹). At the same time, there is a harmony between the experimental adsorption capacities (q_{exp}) and theoretical adsorption capacities (q_2) from the pseudo-second order model (see Table 2). Therefore, the adsorption obeyed the pseudo-second order kinetics.

This situation may be inscribed to a chemical activation between BR2 dye molecules and the functional active sites of adsorbent. Similar findings have been noted for safranin adsorption by peanut shell,²⁷ carbonized spent coffee ground,⁴⁵ and kaolinite clay.⁴⁶

3.8. Isotherm study

Adsorption isotherm was investigated by the Langmuir and Freundlich models used commonly given elsewhere.^{3,16} According to isotherm analyses results, it is seen that the plot of C_e/q_e versus C_e is a contrary to the Langmuir model. However, the isotherm is in consistent with the Freundlich model. The k and n values were estimated from the intercept and slope of the plot of $\ln q_e$ against $\ln C_e$, respectively. The values of k and n were determined as 29.34 mg g⁻¹ and 0.58 g l⁻¹, respectively. The r^2 value for the Freundlich isotherm was estimated as 0.74. This low r^2 indicates a partial compatibility to the Freundlich model, which shown a randomness adsorption of the dye molecules on the adsorbent surface. A similar result has been noted for BR2 adsorption by peanut shell.²⁷

4. CONCLUSIONS

In this study, the charcoal was produced from peanut shells and then this charcoal was activated chemically with sodium hydroxide. The activated biomass charcoal obtained was used as an adsorbent in removing BR2, a cationic dye from aqueous solution in batch and column systems. The maximum adsorption of BR2 by the activated biomass charcoal (i.e. adsorbent capacity) was determined to be 99.91% and 99.50% in batch and column systems, respectively. It was seen that the adsorption obeyed the Freundlich isotherm and the pseudo-second order kinetic model. At the same time, a surface adsorption was estimated to be occurred on the heterogeneous adsorbent surface. Alternative to commercial activated carbon, the activated biomass charcoal produced from peanut shell was determined to be used easily for the adsorption of BR2 dye, a cationic dye.

ACKNOWLEDGEMENTS

This study was supported by The Scientific and Technical Research Council of Turkey (TUBITAK), project number: 107Y043.

Conflict of interest

Authors declare that there is no a conflict of interest with any person, institute, and company, etc.

REFERENCES

- Argun, M. E.; Dursun, S.; Gur, K.; Ozdemir, C.; Karatas, M.; Dogan, S. *Environ Technol.* **2005**, 26, 479-487.
- Acemioğlu, B.; Alma, M. H. *Fresenius Environ. Bull.* **2004**, 13(7), 585-590.
- Acemioğlu, B.; Alma, M. H.; Demirkıran, A. R. *J. Chem. Soc. Pak.* **2004**, 26 (1), 82-89.
- Acemioğlu, B. *Bioresour. Technol.* **2004**, 93, 99-102.
- Hamdaoui, O.; Saoudi, F.; Chida, M.; Naffrechoux, E. *Chem. Eng. J.* **2008**, 143, 73-84.
- Yagub, M. T.; Sen, T. K.; Ang, H. M. *Water Air Soil Pollut.* **2012**, 223, 5267-5282.
- Deniz, F.; Karaman, S. *Chem. Eng. J.* **2011**, 170, 67-74.
- Ofomaja, A. E.; Ho, Y. S. *Bioresour. Technol.* **2008**, 99, 5411-5417.
- Mane, V. S.; Vijay Babu, P. V. *Desalination* **2011**, 273, 321-329.
- Witek-Krowiak, A. *Chem. Eng. J.* **2011**, 171, 976-985.
- Dulman, V.; Cucu-Man, S. M. *J. Hazard. Mater.* **2009**, 162, 1457-1464.
- Acemioğlu, B.; Alma, M. H. *Holz Roh Werkst.* **2004**, 62, 268-272.
- Ning-Chuan, F.; Xue-yi, G. *Trans. Nonferrous Met. China*, **2012**, 22, 1224-1231.
- Annadurai, G.; Juang, R. S.; Lee, D. J. *J. Hazard. Mater.* **2002**, B92, 263-274.
- Sartepé, A. S.; Mandhare, A. M.; Jadhav, V. V.; Raut, P. D.; Anuse, M. A.; Kolekar, S. S. *Arabian J. Chem.* **2017**, 10, 3229-3238.
- Kule, L.; Acemioğlu, B.; Baran, E. *Int. J. Chem. Technol.* **2017**, 1, 58-66.
- Pagnenelli, F.; Mainelli, S.; Veglio, F.; Toro, L. *Chem. Eng. J.* **2003**, 4709-4717.
- Hodaifa, G.; Driss Alami, S. B.; Ochando-Pulido, J. M.; Victor-Ortega, M. D. *Ecol. Eng.* **2014**, 73, 270-275.
- Dagdelen, S.; Acemioğlu, B.; Baran, E.; Koçer, O. *Water Air Soil Pollut.* **2014**, 225 (3) Article Number: 1899, 1-15.
- Koçer, O.; Acemioğlu, B. *Desalin. Water Treat.* **2016**, 57 (35) 16653-16669.
- Öncel, M.; Guvenç, İ.; Acemioğlu, B. *Asian J. Chem.* **2012**, 24 (4), 1698-1704.
- Duran, C.; Ozdes, D.; Gundogdu, A.; Senturk, H. B. *J. Chem. Eng. Data.* **2011**, 56 (5), 2136-2147.
- Doğan, M.; Abak, H.; Alkan, M. *J. Hazard. Mater.* **2009**, 164, 172-181.
- Ding, D.; Zhao, Y.; Yang, S.; Shi, W.; Zhang, Z.; Lei, Z.; Yang, Y. *Water Res.* **2013**, 47, 2563-2571.
- Robinson, T.; Chandaran, B.; Nigam, P. *Bioresour. Technol.* **2002**, 85, 119-124.
- Wafwoyo, W.; Seo, C. W.; Marshall, W. E. *J. Chem. Technol. Biotechnol.* **1999**, 74, 1117-1121.
- Şakalar, N.; Bilir, M. H.; Acemioğlu, B.; Alma, M. H. *Asian J. Chem.* **2010**, 22 (7) 5649-5662.
- Şamil, A.; Acemioğlu, B.; Gültekin, G.; Alma, M. H. *Asian J. Chem.* **2011**, 23 (7), 3224-3230.
- Akkoc, Y.; Acemioğlu, B. *Fresenius Environ. Bull.* **2018**, 27 (12A), 9357-9365.
- Karaoğlu, M. H.; Uğurlu, M. *Fresenius Environ. Bull.* **2010**, 19 (12b), 3199-3208.
- Acemioğlu, B.; Şakalar, N. *Fresenius Environ. Bull.* **2017**, 26 (8), 5305-5313.
- Bilir, M. H.; Şakalar, N.; Acemioğlu, B.; Baran, E.; Alma, M. H. *J. Appl. Polym. Sci.* **2013**, 4340-4351.
- Acemioğlu, B.; Bilir, M. H.; Alma, M. H. *Int. J. Chem. Technol.* **2018**, 95-104.
- Acemioğlu, B. *Int. J. Coal Prep. Util.* **2019**, <https://doi.org/10.1080/19392699.2019.1644326>
- Kumar, K. V. *J. Hazard. Mater.* **2007**, 142, 564-567.
- Zaghbani, N.; Hafiane, A.; Dhahbi, M. *Desalination* **2008**, **222**, 348-356.
- Wakkal, M.; Khiari, B.; Zagrouba, F. *Environ. Sci. Pollut. Res.* **2019**, 26, 18942-18960.

DOI: <http://dx.doi.org/10.32571/ijct.650476>

E-ISSN:2602-277X

38. Dmitrienko, S. G.; Siviridova, O. A.; Pyatkova, L. N.; Senyamin, V. M. *Anal. Bioanal. Chem.* **2002**, 374(3), 361-368.

39. Hameed, B. H.; Mahmoud, D. K.; Ahmad, A.L. *J. Hazard. Mater.* **2008**, 158(2-3) 499-506.

40. Bayramoğlu, G.; Arica, M. Y. *J. Hazard. Mater.* **2007**, 143(1-2), 135-143.

41. Xu, R. K., S. C. Xiao, J. H. Yuan, and A. Z. Zhao. *Bioresour. Technol.* **2011**, 102, 10293-10298.

42. Weber, W. J. Morris, J.C. *J. Sanit Eng. Div.* 1963, **89** (SA2), 31-59.

43. Lagergren, S. K. *Sven. Vetenskapsakad. Handl.* Band 24, 1-39.

44. Ho, Y.S.; McKay, G. *Chem. Eng. J.* **1998**, 70, 115-124.

45. Lakshmi Prasanna, M.; Sumithra, S.; Madakka, M. *Int. J. Recent Sci. Res.* **2016**, 7(4), 10401-10405.

46. Adebowale, K. O.; Olu-Owalabi, B. I.; Chigbundu. C. E. *J. Encapsulation Adsorpt. Sci.* **2014**, 4, 89-104.

ORCID

 <https://orcid.org/0000-0002-0728-2747> (B. Acemioğlu)

 <https://orcid.org/0000-0001-7415-1088> (N. Karataş)

 <https://orcid.org/0000-0001-9987-1882> (M. H. Güler)

 <https://orcid.org/0000-0001-9218-5513> (M. Ertaş)

 <https://orcid.org/0000-0001-6323-7230> (M. H. Alma)



Inhibition effects of commonly used some antibacterial and antiviral drugs on purified human serum paraoxonase-1 (hPON1)

Hakan SÖYÜT*

on the last page

Department of Basic Education, Faculty of Education, Uludag University, Bursa, 16059, Turkey

Received: 26 November 2019; Revised: 07 December 2019; Accepted: 11 December 2019

*Corresponding author e-mail: hakansoyut@uludag.edu.tr

Citation: Söyüt, H. *Int. J. Chem. Technol.* 2019, 3 (2), 146-150.

ABSTRACT

hPON1 is an enzyme from the group of A-esterases which is capable of hydrolyzing the active metabolite paraoxon of parathion, an organic phosphorus insecticide. It is an important liver enzyme that plays a protective role against the hydrolysis of HDL-induced organophosphate agents and nerve gases, oxidation of LDL, formation of lipid peroxides and bacterial endotoxins. The fact that oxidation of LDL constitutes the initial stage of the atherosclerosis process reveals the importance of the antioxidant properties of the enzyme. In this study, human serum PON1 was purified using three simple biochemical purification techniques. Furthermore, the in vitro effects of some antibacterial and antiviral drugs on human serum PON1 enzyme activity were examined. IC50 values were determined.

Keywords: Paraoxonase, enzyme inhibition, antibacterial drug, antiviral drug.

1. INTRODUCTION

The relationship of bacteria and viruses to humans is as old as human existence. They cause various infections in children, young and old. Clarithromycin (Figure 1a) is a broad spectrum antibacterial drug. It is most commonly used for the treatment of respiratory infections.¹ In addition to its antibacterial activity, it shows a wide range of pharmacological effects.² Cefepime hydrochloride (Figure 1b) is a bactericidal cephalosporin for a wide variety of organisms. Cefepime hydrochloride which is a 4th generation cephalosporin is used widely as an antibacterial agent. It is effective against many types of

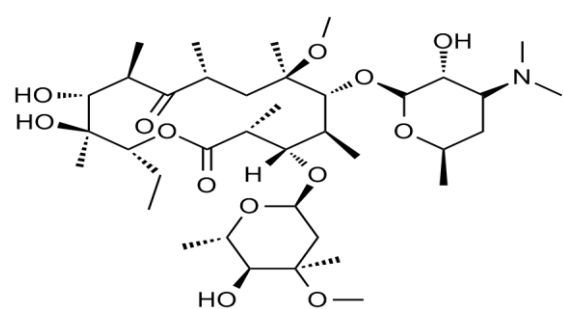
Sık kullanılan bazı antibakteriyel ve antiviral ilaçların saflaştırılmış insan serum paraoksonaz-1 (hPON1) üzerine inhibisyon etkileri

ÖZ

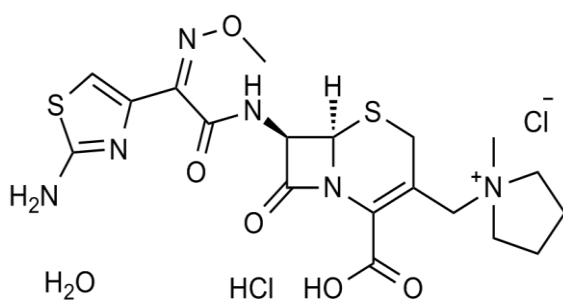
hPON1, bir organik fosfor insektisid olan parathion'un aktif metabolit paraoksonunu hidrolize edebilen A-esteraz grubundan bir enzimdir. HDL'nin neden olduğu organofosfat ajanlarının ve sinir gazlarının hidrolizine, LDL'nin oksidasyonuna, lipid peroksidlerin ve bakteriyel endotoksinlerin oluşumuna karşı koruyucu bir rol oynayan önemli bir karaciğer enzimidir. LDL'nin oksidasyonunun ateroskleroz sürecinin başlangıç aşamasını oluşturması, enzimin antioksidan özelliklerinin önemini ortaya koymaktadır. Bu çalışmada, insan serumu PON1, üç basit biyokimyasal saflaştırma tekniği kullanılarak saflaştırıldı. Ayrıca, bazı antibakteriyel ve antiviral ilaçların insan serumu PON1 enzim aktivitesi üzerindeki in vitro etkileri incelendi. IC50 değerleri belirlendi.

Anahtar Kelimeler: Paraoksonaz, enzim inhibisyonu, antibakteriyel ilaç, antiviral ilaç.

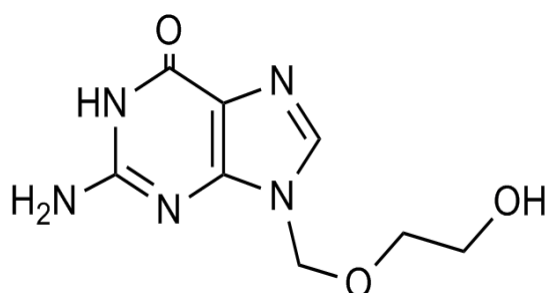
bacteria.³ Acyclovir (Figure 1c) is the most widely used powerful antiviral drug. It is used to inhibit replication of many viruses.⁴ Cefazolin sodium (Figure 1d) is a antibacterial drug classified as first generation cephalosporin. It is a semi-synthetic β -lactam for intravenous administration. It has a limited spectrum of destructive bacteria. It is used for prophylaxis in pregnancy interventions.⁵ hPON1 is a Ca^{2+} -dependent. It is called arildalkylalkyl phosphatase. It has been previously thought to be lactone because of its physiological effects, it has been found that the enzyme has many substrates and many functions. As a result of studies on mice, hPON1 enzyme has been determined to



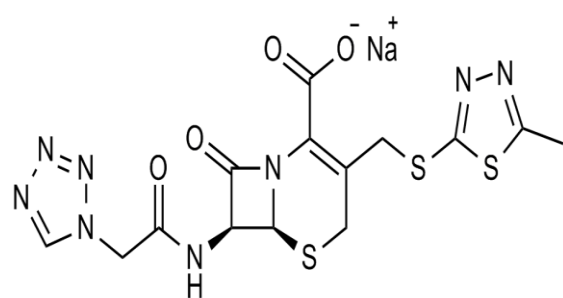
(a)



(b)



(c)



(d)

Figure 1. Chemical structures of the drugs: a) Clarithromycin, b) Cefepime hydrochloride, c) Acyclovir, d) Cefazolin sodium.

be an HDL dependent lactonase with antioxidant and antiatherogenic effects. It has been observed that the development of atherosclerosis is accelerated and oxidative stress is increased in mice lacking PON1 enzyme. It has been observed that hPON1 enzyme transferred mice has decreased both oxidative stress and the number of lesions.⁶

It has been found that it decreased lipid peroxide accumulation on LDL by an enzymatic mechanism when stored under HDL oxidizing conditions. hPON1 is one of the factors associated with this feature of HDL. Furthermore, hPON1 limits the accumulation of oxidized LDL and HDL particles. It inhibits the conversion of LDL to proatherogenic particles and reverses the biological effects of oxidized LDL particles. Thus, it has been shown to prevent the formation and progression of atherosclerosis lesions.⁷

Due to diseases affected by the change in hPON1 activity, the inhibition of antibacterial and antiviral drugs is important. If any drug causes a decrease in hPON1 enzyme activity, many vascular diseases may occur, including atherosclerosis. Indeed, due to the physiological role of hPON1, further studies on the inhibitory effects of drugs should be conducted. However, there are many studies about the inhibition effects of drugs on the hPON1.⁷⁻⁹

Antibacterial and antiviral drugs are used in the treatment of serious bacterial diseases. However, the patient is extremely important for adjusting drug doses. In this study, we purified hPON1 from human serum and examined the in vitro effects of antibacterial and antiviral drugs on enzyme activity.

2. MATERIALS AND METHODS

2.1. Materials

DEAE-Sephadex A50, Sepharose 4B, 1-naphthylamine, paraoxone, protein reagents and chemicals used for electrophoresis were obtained from Sigma Chemical Co. All other chemicals were obtained from Sigma-Aldrich or Merck. Clarithromycin, cefepime hydrochloride, acyclovir, and cefazolin sodium were obtained from local pharmaceutical manufacturing companies.

2.2. Paraoxonase activity assay

Human serum samples were supplied from the Research Hospital at Ataturk University. PON1 activity was determined at 250°C with paraoxon (diethyl p-nitrophenyl phosphate) (1mM) in 50 mM glycine/NaOH (pH 10.5) containing 1 mM CaCl₂. PON1 assay was based on the estimation of p-nitrophenol at 412 nm.

The molar extinction coefficient of p-nitrophenol ($\epsilon = 18.29 \text{ M}^{-1}\text{cm}^{-1}$ at pH 10.5) was used to calculate PON1 activity. One enzyme unit was defined as the amount of enzyme that catalyses the hydrolysis of 1 μmol of substrate at 25°C. Assays were performed using a spectrophotometer (CHEBIOS UV-VIS).

2.3. Ammonium sulphate precipitation

Human serum precipitated with 60–80% ammonium sulphate was carried out in our previous studies. The precipitate was obtained after centrifugation at $15,000 \times g$ for 20 minutes and redissolved in a 100 mM Na-phosphate buffer (pH 7.0).

2.4. DEAE-Sephadex A50 anion exchange chromatography

At first, the anion exchange column was equilibrated with a 100 mM Na-phosphate buffer (pH 7.0). Then, the enzyme solution, which had been dialyzed in the presence of 1 mM Na-phosphate buffer (pH 7.0) for two hours, was loaded onto the DEAE-Sephadex A50 anion exchange column (3 cm \times 30 cm). Later, the chromatography column was washed with a 100 mM Na-phosphate buffer (pH 7.0), and then elution was carried out by an increasing linear gradient of 0-1.5 M NaCl. The elution fractions collected were checked for enzyme activity at 412 nm. Tubes which displayed the same enzyme activity were combined. All these procedures were performed at 4°C.

2.5. Sephadex G-200 gel filtration chromatography

In the first process, the sephadex G-200 column (60 cm \times 2 cm) was equilibrated with 100 mM Na-phosphate buffer (pH 7.0). Fractions from the DEAE-Sephadex A50 anion exchange column were mixed with glycerol and loaded onto the gel filtration column with the same buffer. Finally, the enzyme solutions were separated from the sephadex G-200 column. Protein amount (at 280 nm) and enzyme activity (at 412 nm) were recorded for all tubes. Tubes showing enzyme activity were combined for other kinetic studies.

2.6. Protein Determination

Quantitative protein determination was performed by spectrophotometric purification steps at 595 nm according to Bradford method.

2.7. SDS polyacrylamide gel electrophoresis

SDS polyacrylamide gel electrophoresis was performed to check that the enzyme was purified according to the procedure of Laemmli. The resulting single band was photographed after electrophoresis.

2.8. In vitro studies for the drugs

We studied the inhibitory effects of four antibiotic drugs: Clarithromycin, cefepime hydrochloride, acyclovir, and ceftazidime sodium. All compounds were tested three times for each concentration used. hPON1 activities were measured in the presence of different drug concentrations. In the absence of an inhibitor, the control activity was assumed to be 100%. For each drug, activity % - [I] plots were plotted and IC₅₀ values were calculated from the equation of the curve.

3. RESULTS AND DISCUSSION

hPON1 is a calcium-dependent esterase that hydrolyzes esters such as organophosphate and lactone. hPON1 is a glycoprotein with a molecular weight of 43-45 kDa. It is mainly synthesized by the liver. hPON1 is one of the antioxidant defense mechanisms in the human body. There are many cleaning systems for reactive oxygen species, including paraoxones in the human body. hPON1 removes reactive oxygen species in living metabolism and protects LDL, HDL and macrophages against oxidative stress. Therefore, hPON1 prevents cardiovascular disease.¹⁰⁻¹³

There are many studies on hPON1 inhibition. For instance, Ekinçi and Beydemir researched the effects of some drugs, lornoxicam (a), indomethacin (b), tenoxicam (c), diclofenac sodium (d), ketoprofen (e) and lincomycin (f), on hPON1 activity from human serum. They founded that lornoxicam inhibits the enzyme activity significantly, compared to the other drugs. The inhibition order of the drugs determined as $a > b > c > d > e > f$.¹⁴ In another study, the impacts of some commonly used antibiotics as teicoplanin, rifamycin, tobramycin, ceftriaxone sodium, cefuroxime sodium, ceftazidime, ornidazole, and amikacin sulfate were investigated on human serum hPON1 activity. The major inhibitor was teicoplanin.¹⁵

For example, Türkeş and co-workers have investigated that some chemotherapeutic drugs, palonosetron hydrochloride, bevacizumab, and cyclophosphamide on hPON1 effects. Inhibition range of the drugs are in the order palonosetron hydrochloride > bevacizumab > cyclophosphamide. However, chemotherapeutic drugs are used to treat cancer patients. Therefore, this may be particularly critical for patients with atherosclerotic lesions.⁹ For instance, Türkeş and co-workers have reported that some antibacterial drugs, moxifloxacin hydrochloride (1), levofloxacin hemihydrate (2), cefepime hydrochloride (3), cefotaxime sodium (4) and ceftizoxime sodium (5) on hPON1 effects. It is important that antibiotic drugs are potent inhibitors of human serum hPON1.

Moxifloxacin hydrochloride was found to significantly inhibit enzyme activity compared to other antibiotics.

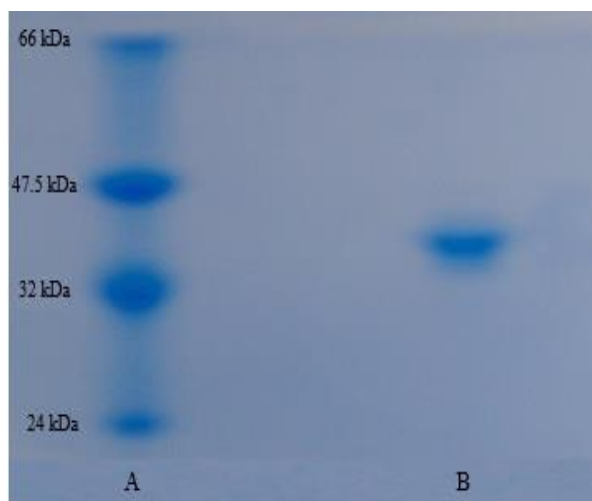


Figure 2. SDS-PAGE analysis of purified hPON1. Lane A is standard proteins (kDa): Bovine serum albumin (66 kDa), aldolase (47.5 kDa), triosephosphate isomerase (32 kDa), and soy bean trypsin inhibitor (24 kDa). Lane B contains a human serum sample.

Table 1. IC₅₀ values

Inhibitors	IC ₅₀ (mM)
Clarithromycin	0.459
Cefepime hydrochloride	14.518
Acyclovir	56.169
Cefazolin sodium	150.602

The order of inhibition of the drugs was determined as 1 > 2 > 3 > 4 > 5.⁸

In this study, a specific activity of 4060 EUx mg⁻¹ from hPON1 human serum was purified approximately 295-fold in 53.9% yield.

The purified human serum paraoxonase had a molecular weight of 43 kDa (Figure 2). Inhibition effect studies on paraoxonase activity of antibiotic drugs were performed. IC₅₀ values for (a) clarithromycin, (b) cefepime hydrochloride, (c) acyclovir, and (d) cefazolin sodium were determined by means of activity % - [I] graphs as 0.459, 14.518, 56.169, and 150.602 mM, respectively (see Table 1 and Figure 3). As a result of inhibition studies, it was observed that antibiotic drugs inhibit hPON1 enzyme. Clarithromycin showed the most inhibition.

It is known that an adult person has a total of about 5 liters of blood. Accordingly, cefepime hydrochloride (b), acyclovir (c), and cefazolin sodium (d) blood concentrations were calculated as 0.175, 0.0198, and

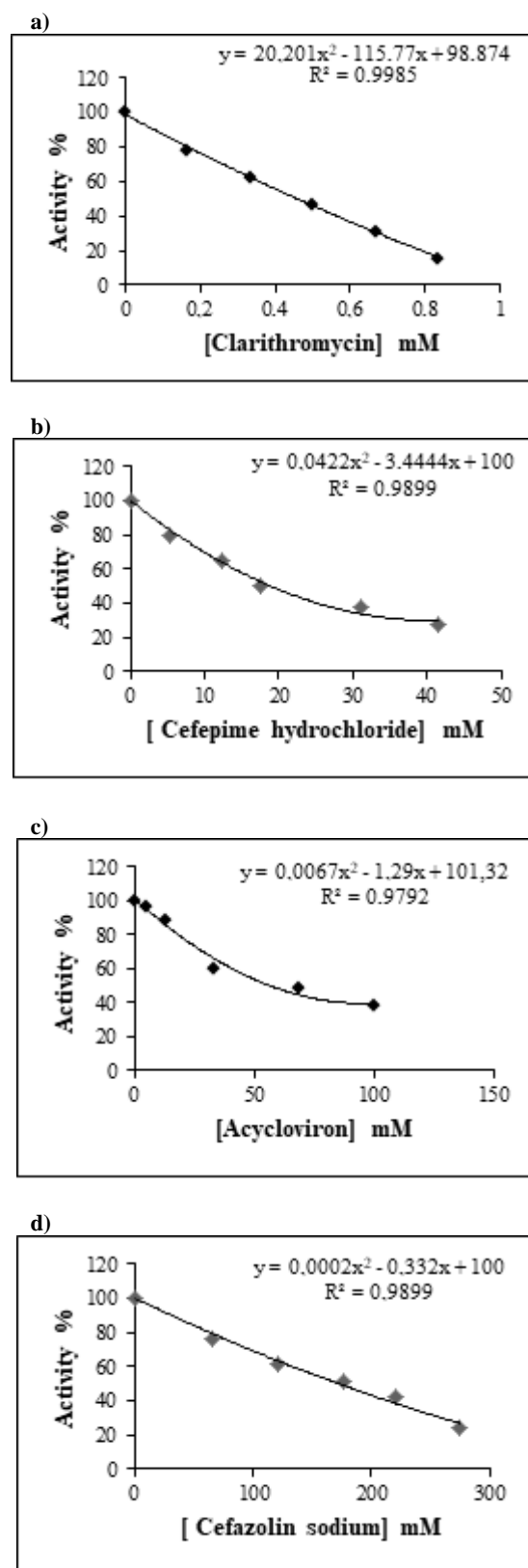


Figure 3. *In vitro* effect of antibacterial drugs: a) clarithromycin, b) Cefepime hydrochloride, c) Acyclovir, d) Cefazolin sodium at five different concentrations on hPON1 activity.

0.440 mM, respectively. These values are lower than IC50 values. However, (a) the blood concentration of clarithromycin was determined to be 0.134 mM near the IC50. This research can be clarified by in vitro studies. Because these antibacterial drugs are widely used in the treatment of bacterial infections.

4. CONCLUSIONS

As a result, hPON1 was purified using three simple purification steps. The in vitro effects of antibacterial drugs on hPON1 were investigated. Blood concentrations and IC50 drug values were then compared. However, clarithromycin is the most inhibition drug. Prolonged use of this drug may cause a decrease in enzyme activity. Decrease in enzyme activity may contribute to atherosclerosis. Consequently, it may increase cardiovascular diseases.

Conflict of interest

Author declares that there is no a conflict of interest with any person, institute, company, etc.

REFERENCES

- Bandettini di Poggio, M.; Anfosso, S.; Audenino, D.; Primavera, A. *J. Clin. Neurosci.* **2011**, 18, 313-318.
- Giamarellos-Bourboulis, E.J.; Antonopoulou, A.; Raftogiannis, M.; Koutoukas P, Tsaganos, T., Tziortzioti, V., Panagou, C., Adamis, T., Giamarellou, H. *BMC Infect. Dis.* **2006**, 21, 31.
- Cheatham, S. C.; Shea, K. M.; Healy, D. P.; Humphrey, M. L.; Fleming, M. R.; Wack, M. F.; Smith, D. W.; Sowinski, K. M.; Kays, M. B. *Int. J. Antimicrob. AG.* **2011**, 37 (1), 46-50.
- Feng, M.Q.; Cai, Q.S.; Huang, H.; Zhou, P. *Eur. J. Pharm. Biopharm.* **2008**, 68, 688-693.
- Singh, A. K.; Quraishi, M. A. *Corros. Sci.* **2010**, 52, 152-160.
- Khersonsky, O.; Tawfik, D. S. *Biochemistry* **2005**, 44, 6371-6382.
- Türkeş, C.; Söyüt, H.; Beydemir, Ş. *Pharmacol. Rep.* **2014**, 66, 74-78.
- Türkeş, C.; Söyüt, H.; Beydemir, Ş. *J. Enzyme Inhib. Med. Ch.* **2015**, 30, 622-628.
- Türkeş, C.; Söyüt, H.; Beydemir, Ş. *Environ. Toxicol. Phar.* **2016**, 42, 252-257.
- Gaidukov, L.; Tawfik, D. S. *Biochemistry* **2005**, 44, 11843-11854.
- Renault, F.; Chabriere, E.; Andrieu, J.P.; Dublet, B.; Massona, P.; Rochua, D. J. *Chromatogr. B.* **2006**, 836, 15-21.
- Aviram, M.; Rosenblat, M. *Free Radical Bio. Med.* **2004**, 37, 1304-1316.
- Rozenberg, O.; Shih, S. D.; Aviram, M. *Atherosclerosis* **2005**, 181, 9-18.
- Ekinci, D.; Beydemir, S. *J. Enzyme Inhib. Med. Ch.* **2009**, 24, 1034-1039.
- Ekinci, D.; Beydemir, S. *Eur. J. Pharmacol.* **2009**, 617, 84-89.


ORCID

 <https://orcid.org/0000-0002-0361-7458> (H. Söyüt)



The substituent group activity in the anion of cholinium carboxylate ionic liquids on thermo-physical, chemical reactivity, and biological properties: A DFT study

Afroza ZANNAT¹, Ajoy KUMER¹, Md. Nuruzzaman SARKER², Sunanda PAUL³

 on the last page

¹Department of Chemistry, European University of Bangladesh, Dhaka-1216, Bangladesh

²Department of Physics, European University of Bangladesh, Dhaka-1216, Bangladesh

³Department of Biochemistry and Molecular Biology, University of Chittagong, Chittagong, Hathazari-3443, Bangladesh

Received: 18 November 2019; Revised: 21 December 2019; Accepted: 24 December 2019

*Corresponding author e-mail: kumarajoy.cu@gmail.com

Citation: Zannat, A.; Kumer, A.; Sarker, Md. N.; Paul, S. *Int. J. Chem. Technol.* 2019, 3 (2), 151-161.

ABSTRACT

The thermo-physical, chemical reactivity and biological interaction of cholinium cation Ionic Liquids (ILs) were investigated as theoretical by density functional theory (DFT). Some thermo-physical parameters such as free energy, entropy, dipole moment, binding energy, nuclear energy, electronics energy, the heat of formation were computed. The chemical reactivity of molecule like highest occupied molecular orbital (HOMO), lowest unoccupied molecular orbital (LUMO), HOMO-LUMO gap, ionization potential, electronegativity, hardness, softness and electron affinity were calculated. Properties like charge density, surface area grid, volume, LogP, polarizability, refractivity, and molecular mass were calculated using the quantitative structure activity relationship (QSAR). The cholinium benzoate (IL01), cholinium-2-nitro-benzoate (IL02), cholinium-2-methylbenzoate (IL03), cholinium -2-hydroxy benzoate (IL04), cholinium -2-chlorobenzoate (IL05), and cholinium -2-fluorobenzoate (IL06) were taken for study. With adding of substituent groups to the anion, the chemical stability increased, and chemical reactivity decreased in the order of -H > -CH₃ > -OH > -Cl > F- > -NO₂ groups. The physical properties and biological activity are observed to be changed irregularly for different substituent groups.

Keywords: Choline, ionic liquids, HOMO-LUMO, QSAR, vibrational spectroscopy.

Kolinum karboksilat iyonik sıvıların anyonundaki süstitüe grubun thermo-fiziksel, kimyasal reaktivite ve biyolojik özellikler üzerine aktivitesi: Bir DFT çalışması

ÖZ

Cholinium katyon iyonik sıvılar (ILs) 'nin termo-fiziksel, kimyasal reaktivitesi ve biyolojik etkileşimi yoğunluk fonksiyonel teorisi (DFT) ile teorik olarak araştırılmıştır. Serbest enerji, entropi, dipol momenti, bağlayıcı enerji, nükleer enerji, elektronik enerji, oluşum ısısı gibi bazı termo-fiziksel parametreler hesaplanmıştır. En yüksek işgal edilen moleküler orbital (HOMO), en düşük boş moleküler orbital (LUMO), HOMO-LUMO boşluğu, iyonlaşma potansiyeli, elektronegatiflik, sertlik, yumuşaklık ve elektron afinitesi gibi moleküllerin kimyasal reaktivitesi hesaplanmıştır. Yük yoğunluğu, yüzey alanı ızgarası, hacim, LogP, polarizasyon, kırılma ve moleküler kütle gibi özellikler, nicel yapı aktivite ilişkisi (QSAR) kullanılarak hesaplanmıştır. Cholinium benzoat (IL01), cholinium-2-nitro-benzoat (IL02), cholinium-2-metilbenzoat (IL03), cholinium -2-hidroksi benzoat (IL04), cholinium-2-klorobenzoat (IL05) ve cholinium-2-fluorobenzoat (IL06) çalışma için alındı. Anyona süstitüe gruplarının eklenmesi ile kimyasal kararlılık arttı ve kimyasal reaktivite -H > -CH₃ > -OH > -Cl > F- > -NO₂ sırasına göre azaldı. Fiziksel özellikler ve biyolojik aktivite farklı süstitüe gruplar için düzensiz olarak değiştiği gözlemlendi.

Anahtar Kelimeler: Kolin, iyonik sıvılar, HOMO-LUMO, QSAR, titreşimsel spektroskopisi.

1. INTRODUCTION

Ionic Liquids (ILs) is defined as liquid salts or melted salts at room temperature.¹ Several types of ILs are documented last twenty years. The most important and

fascination to ILs for their vast applications belong to almost all areas of chemistry, chemical engineering, material science, and pharmaceutical industry. Due to tunable physical, and chemical properties like almost null vapor pressure, low volatility, low toxicity, high thermal

stability, and biodegradability, they have become green solvents for industrial uses.² Nowadays, the ammonium, imidazolium, pyridium, phosphonium, and thiazolium etc are the most common ILs using for various purposes. The last decades, the high rising voice of scientists and researchers for ILs is going to the pharmaceutical active ingredients and microbial activity with sustainable methods.³ Among them, ammonium, cholinium, and phosphonium cation based ILs are highly considerable cation to obtain the microbial activity and drug discovery. On the other hand, some ammonium carboxylate and cholinium carboxylate have established the biological activity against both of bacterial and fungal micro pathogens,⁴⁻⁷ even some cholinium and phosphonium ILs were found the anticancer potential.⁸

In general, the choline is considered as the natural molecule and mostly used as nutrient for animal especially in poultry farm. For this reason, the choline is effortlessly found in synthetic or natural form.⁹ In our study, the choline was taken to design the new cholinium based carboxylate ILs in view of theoretical investigation using a computational approach. The second point is noted that the carboxylate was selected as anion with cholinium cation for their biodegradable properties. As there were vast publications and documents on cholinium cation based ILs during last ten years particularly in experimental fields such as synthesis, antimicrobial, catalysis, application in chemical process and organic synthesis, there are well poor data for theoretical investigation. For this point, the cholinium carboxylate ILs were chosen for the development of thermophysical properties, chemical reactivity, and biological activity.¹⁰⁻¹² The computational approach is the best tool to explain the theoretical study of molecules. The estimation of HOMO and LUMO of molecules belongs to the region of electrophilic and electrophonic area. Our previous work for different investigation and prediction of ionic liquids and complex of metallic crystal^{13,14} shows that the HOMO, LUMO values vary from -9.00 to -7.00, and also the values used to calculate the chemical reactivity indices vary from -2.00 to 0.50.¹⁴⁻¹⁷ The second addressing documents for thermophysical and physical properties which contribute a theoretical profile for their applications were documented using the computational tools.¹⁸ Finally, the biological activity was evaluated by the quantitative structural activity relationship (QSAR) which includes the surface area, volume, refractivity, polarizability, logP, and molecular weight. The logP expresses the toxicity and non toxicity having value of positive and negative. Herein, because the all molecules were designed regarding new bioactive on basis of cholinium cation,¹⁹⁻²⁰ they have no scope to compare with experimental study or data. Due to have the lacking of experimental profile of predicted ILs, this study represents a theoretical profile using computational approaches only.²¹ The most beneficial of the study is safe the money including conducting cost of chemicals in

laboratory and consumption of time in the laboratory. It provides the theoretical prediction of the examined molecule to safe use in any area.

2. COMPUTATIONAL METHOD

To create the spatial chemical structure of each calculated molecule, the two-dimensional structure of the molecule shall be built step-by-step by drawing. Then hydrogen atoms are automatically added from building option and chemical structure is converted into a 3D structure. The first step in getting the main characteristic parameters of molecules is to optimize the molecular structure to obtain a configuration characterized by minimum free energy. In sitting the DFT was fixed via 6G-31G*, and B3LYP.²² For this calculation, model build was done at first, then fixed the 6G-31G*, total charge zero, spin multiplicity one, UHF, convergence limit is 1e-006. The cut off is fixed 1e-006 with core Hamiltain calculation and done geometry optimization to record the data of free energy, entropy, dipole moment, binding energy, nuclear energy, electronics energy, the heat of formation, the HOMO, LUMO, 3D mapped structure of electrostatic potential. The QSAR properties were also calculated.

3. RESULTS AND DISCUSSION

3.1 Optimized structure

A representation of the molecular structure optimized which contains the values of the reactivity indices is called the reactive molecular diagram. The optimized structures of molecules are represented in [Figure 1](#). All of the ILs (IL01 to IL06) belongs to the class asymmetry, and non-planar and they have more than one element of symmetry and the plane of the molecule.

3.2. HOMO and LUMO

The possible electronic transition is explained by HOMO and LUMO indicating the electrophilic and nucleophilic attraction region in the molecule. They are highlighted in [Figure 2](#), where the green color is a positive value and blue color is a negative value. The region of HOMO was found on the cation area, and LUMO on the anion area. The HOMO can be found of all molecules in near of -7.00 to 9.00 surrounding in cation. On the other hand, the LUMO was addressed in full of anion having -0.2 to 2.0. The magnitudes of HOMO and LUMO are introduced in [Table 1](#) for zero energy level.

3.3. Chemical reactivity

The energy difference between HOMO and LUMO orbital is called an energy gap which is an important parameter that determines the stability of the structures

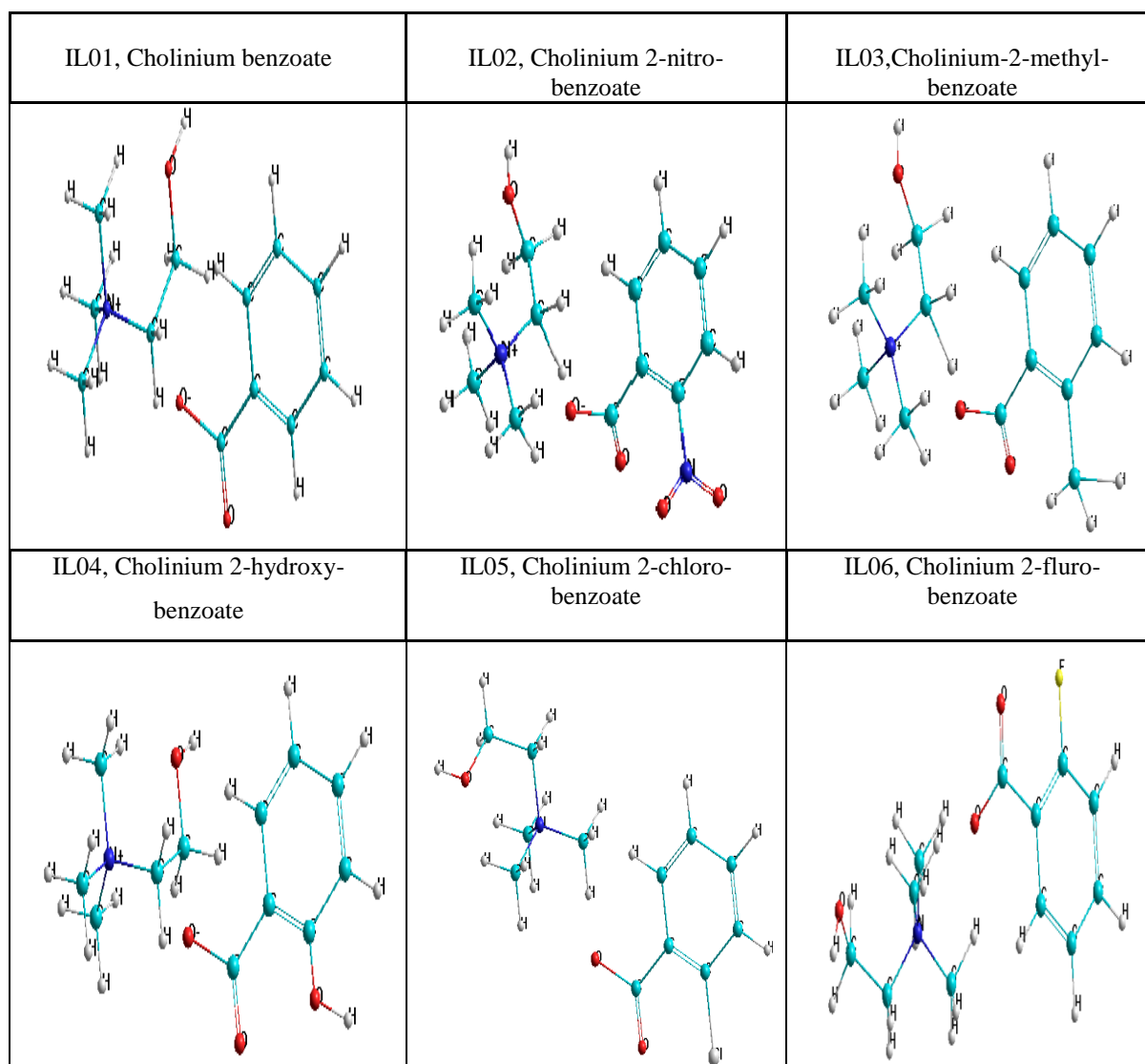


Figure 1. Optimized structure in a cylinder shape, Color: Red is oxygen, cyan is carbon, white is hydrogen, nitrogen is blue, chlorine is white in large size.

and chemical reactivity. The shorter LUMO-HOMO gap is considered to provide the high reactivity (Table 1). In addition, according to Koopmans' theorem the energy gap, ΔE , defined as the difference between HOMO and LUMO energy,¹⁸ it is represented by Eq. (1).

$$\Delta E = (E_{LUMO} - E_{HOMO}) \approx IP - EA \quad (1)$$

The ionization potential (I) and electron affinity (A) can be estimated from the HOMO and LUMO energy values using Equations (1) and (2).

$$I = -E_{HOMO} \quad (2)$$

$$A = -E_{LUMO} \quad (3)$$

The HOMO and LUMO energies are used for the determination of global reactivity descriptors. It is important that Electrophilicity (ω), the chemical potential (μ), Electronegativity (χ), hardness (η) and softness (S) are calculated from Equations (4-8), and they are listed in Table 1.

$$(\mu) = -\frac{I+A}{2} \quad (4)$$

$$(\eta) = \frac{I-A}{2} \quad (5)$$

$$(S) = \frac{1}{\eta} \quad (6)$$

$$(\chi) = \frac{I+A}{2} \quad (7)$$

$$(\omega) = \frac{\mu^2}{2\eta} \quad (8)$$

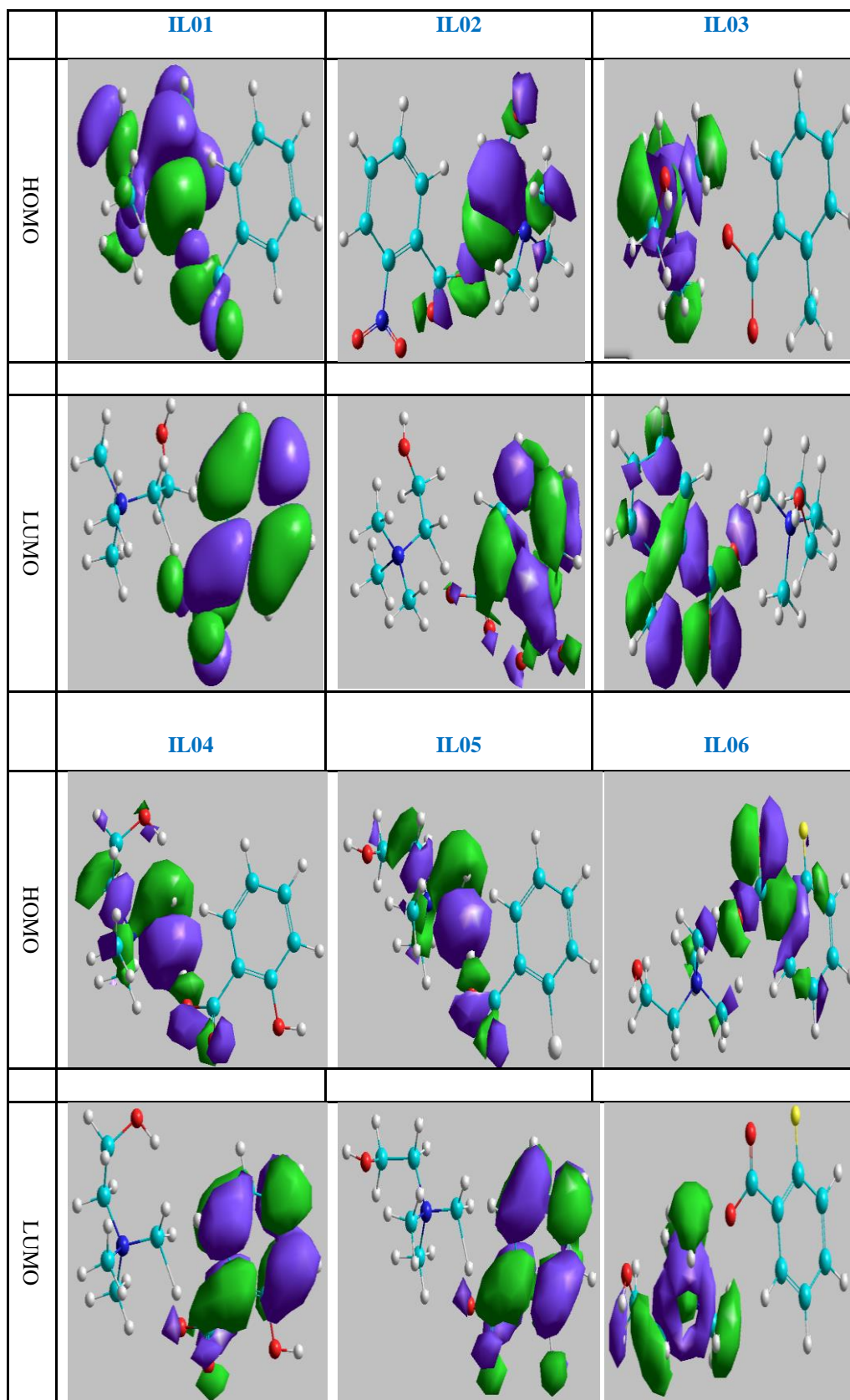


Figure 2. HOMO, LUMO orbitals.

Table 1. Data for LUMO- HOMO gap, ionization potential, and electron affinity

	IL01	IL02	IL03	IL04	IL05	IL06
HOMO, eV	-7.0353	-9.2864	-7.3580	-9.1795	-8.2770	-8.6962
LUMO, eV	-2.1986	-1.6350	-1.4058	-1.5770	-0.6715	-0.1868
ΔE , eV	4.8367	7.6496	5.9522	7.6025	7.6055	8.5100
Ionization potential (I), eV	7.0353	9.2864	7.3580	9.1795	8.2770	8.6962
Electron affinity (A), eV	2.1986	1.6350	1.4058	1.5770	0.6715	0.1868
Hardness (η)	2.4183	3.8257	2.9761	3.8012	3.8027	4.255
Softness (S)	0.4135	0.2613	0.3360	0.2630	0.2629	0.2350
Electrophilicity (ω)	4.0719	3.8972	3.2258	3.8047	2.6321	2.3113
Chemical potential (μ)	-4.6169	-5.4607	-4.3819	-5.3782	-4.4742	-4.4350
Electronegativity (χ)	4.6169	5.4607	4.3819	5.3782	4.4742	4.4350

Table 2. Thermochemical properties

Properties	IL01	IL02	IL03	IL04	IL05	IL06
Total energy (kcal mol ⁻¹)	-63530.50	-80368.10	-67003.00	-70316.80	-60113.70	-73371.5
Free energy (kcal mol ⁻¹)	-63530.50	-80368.10	-67003.00	-70316.80	-60113.70	-73371.5
RMS gradient (kcal mol ⁻¹)	8.51	1.56	1.81	1.92	2.81	0.0119
Binding energy (kcal mol ⁻¹)	-3369.24	-3528.57	-3673.75	-3483.02	-3120.46	-3422.2
Heat of formation (kcal mol ⁻¹)	-36.94	-16.26	-66.36	-91.17	-63.26	-123.07
Electronic energy	-395312.1	-489865.0	-449066.7	-425083.1	-369498.6	-453058.2
Nuclear energy	331781.64	409497.11	382063.77	354766.36	309385.00	379686.01

As seen from Table 1, fluorine atom shows the highest activity on hardness while each group shows activity and the opposite trends are found for softness and electrophilicity. The nitro and methyl groups show the highest chemical potential and electronegativity while all substituent groups show this activity.

3.4. Vibration spectrum

The vibration spectra of cholinium based ILs confirmed the presence of carboxylate (-COO-) from

the symmetric and asymmetric stretching peak at ~1770 cm⁻¹ to ~1550 cm⁻¹, respectively, with the former being overlapped by N-H vibrations. The broad absorption around ~3335-3441 cm⁻¹ can be assigned the presence of -OH groups. The aromatic ring is assigned the presence of C=C bond stretching of two values at ~1540 to ~1600 cm⁻¹ and ~1460 cm⁻¹. Then the C-O bond has also confirmed the peak of 1260-1000 cm⁻¹ in the carbonate salts. The board peak of 2400 cm⁻¹ to 2700 cm⁻¹ indicates the cholinium ion shown in Figure 3.

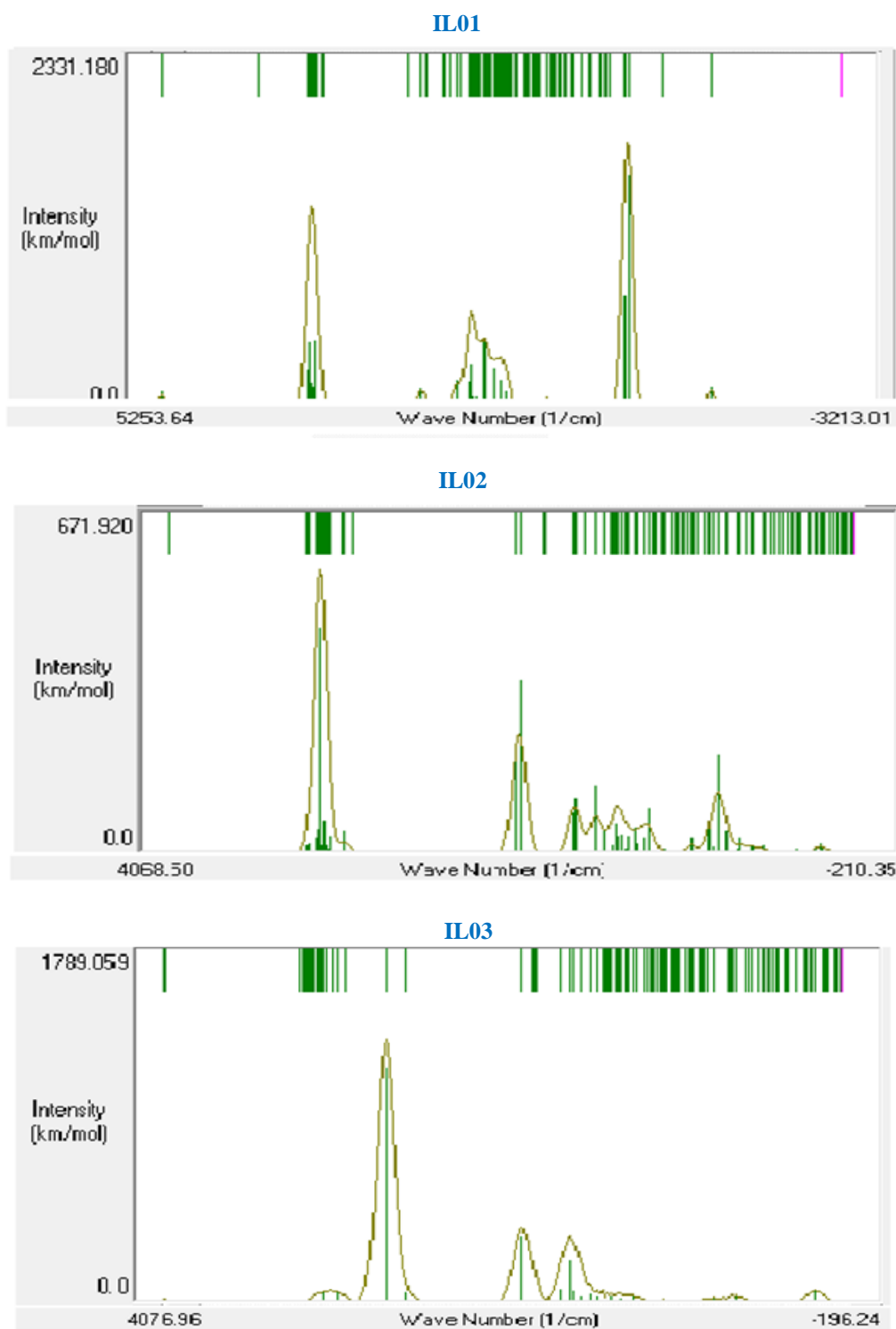


Figure 3. Vibration spectrum of IL01, IL02, IL03.

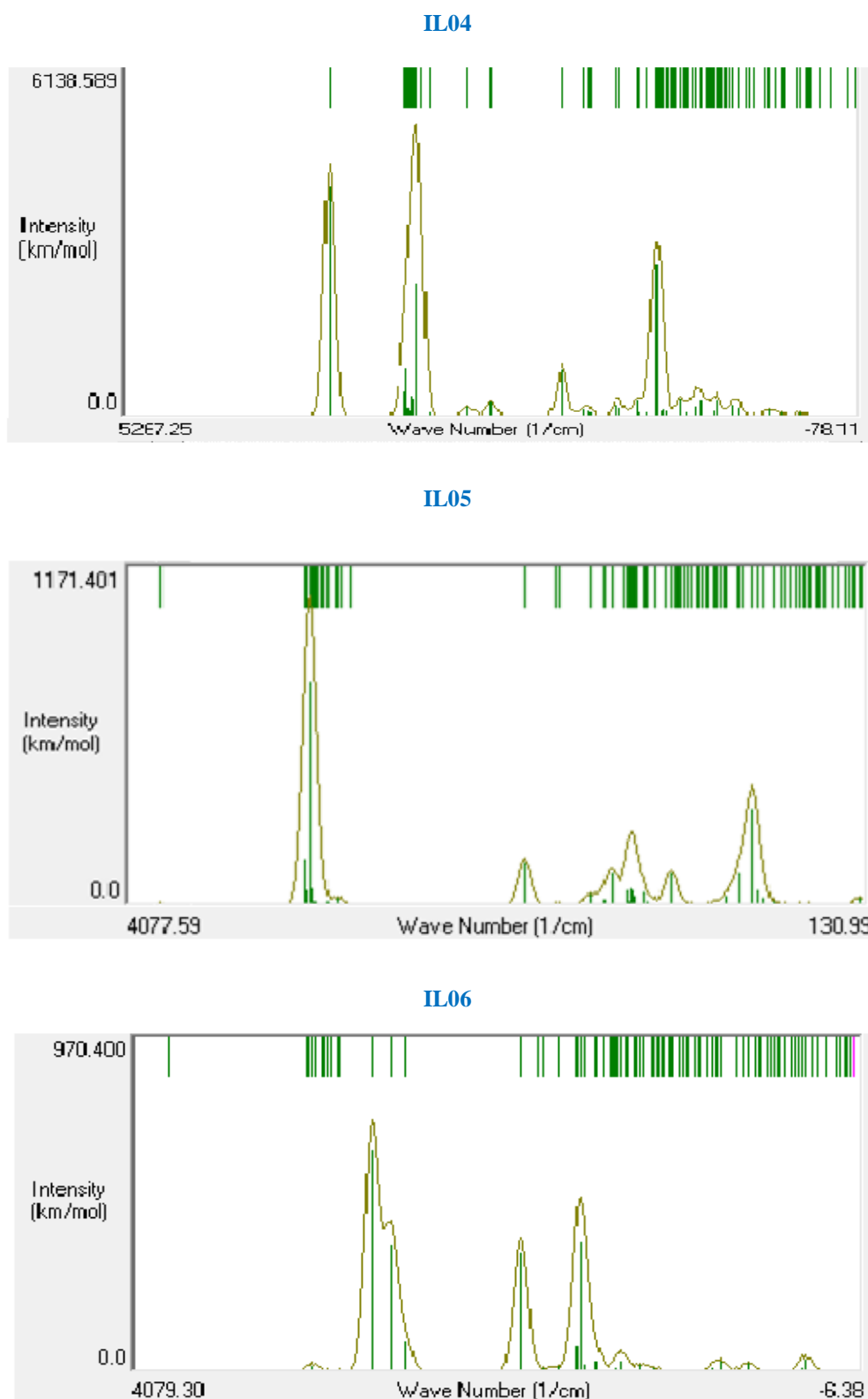


Figure 3. (continued) Vibration spectrum of IL04, IL05 and IL06.

3.5. Thermophysical properties

In order to correlate the molecular structure or properties derived from a molecular structure with a particular chemical or biochemical activity, this method is widely used in pharmaceutical chemistry in the environment and in the search for certain properties. The molecule with minimum binding energy will have the maximum binding affinity and having the maximum binding affinity, indicating as the best molecule for drug leads molecules targeting computationally. From Table 2, it is seen that all ILs have minimum binding energy and the values are very close.

4. BIOLOGICAL ACTIVITIES OF OPTIMIZED MOLECULES

4.1. Distribution electrostatic potential

Electrostatic potential maps or electrostatic potential energy maps, or molecular electrical potential surfaces demonstrate the charge distributions of molecules three dimensionally, which show variably charged regions of a molecule, and molecular interactions with one another.

According to the mechanism of antimicrobial activity and antimicrobial agents of bioactive molecules, the positive charge end of molecules is responsible for damage the plasma membrane of pathogens. To kill pathogens, the region of molecules was used in the positive charge area of the molecule. In this case, the most important factors are explained that the higher surface area having a positive charge is considered as the high antimicrobial activity. In Figure 4, the blue color is the highest charge distribution indicator, and red color as the lowest charge distribution. It can be said that the highest charge distribution occurs in IL05, then IL01, IL03, and IL06, and as lowest in IL02, IL04.

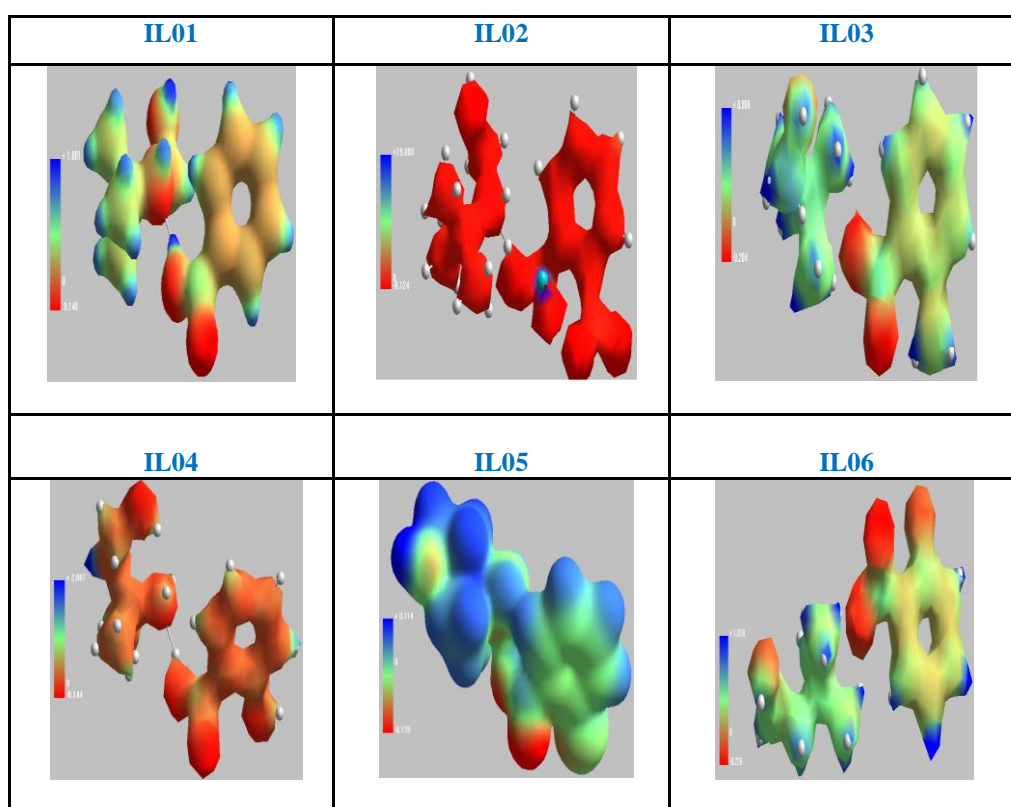


Figure 4. 3D electrostatic potential energy difference of two levels.

Here, E_1 = Electrostatic potential energy in positive value, E_2 = Electrostatic potential energy in negative

value, and ΔE = Electrostatic potential energy difference of two level.

Table 3. Data of electrostatic potential energy difference of two levels

	IL01	IL02	IL03	IL04	IL05	IL06
E1	+1.633	+2.1790	+1.424	+1.473	+2.729	+1.038
E2	-0.262	-0.088	-0.266	-0.385	-0.725	-0.226
$\Delta E = E2-E1$	-1.895	-2.0291	-1.690	-1.858	-3.454	+1.264

Table 4. Data of QSAR

	IL01	IL02	IL03	IL04	IL05	IL06
Partial charge (e)	0.00	0.00	0.00	0.00	0.00	0.00
Surface Area(grid), Å ²	460.15	549.25	470.40	496.51	473.31	455.22
Volume, Å ³	754.74	887.12	779.81	826.54	781.46	740.50
Log P	5.06	-1.89	2.74	2.56	4.28	1.83
Refractivity, Å ³	63.96	68.75	68.17	65.06	68.28	64.04
Polarizability, Å ³	23.90	25.74	25.73	24.53	25.28	23.81
Mass (amu)	225.29	270.29	239.31	241.29	259.73	243.31

Table 5. Correlation in case of substituent groups in anions

	Pi, π	Refractivity, (MR)		Surface Area, (SA)		
Pi, π	Biological activity	Biological activity	SA	Biological activity		
H	0.0	--	0.0	--	0.0	--
F-	+3.23	more	-0.08	more	4.93	more
Cl-	-0.78	Less	4.28	Less	13.16	more
-CH ₃	-2.32	Less	4.21	Less	10.25	more
-OH	-2.50	Less	1.1	Less	36.36	More
-NO ₂	+6.95	more	4.79	more	89.1	more

4.2. Biological study by QSAR

When the biological activity of a molecule is mentioned, its surface area is considered an important parameter. Greater charged surface area of a molecule can be able to kill more pathogens. The charged distribution from electrostatic potential completely depends on the surface area. The greater positive charged surface area means a higher biological activity.²³

On the other hand, a negative value of logP refers to the hydrophilicity, and a positive value of LogP indicates the hydrophobicity that plays an important role in

biochemical interactions and bioactivity. Hydrophobic drugs tend to be more toxic, because they are kept generally longer and have a wider distribution in the body. Also, they are somewhat less selective in their binding to molecules and finally are often extensively metabolized. Therefore ideal distribution coefficient for a drug is usually intermediate (not too hydrophobic or too hydrophilic). From the data in Table 4, the IL02 has -1.89 value that indicates lower hydrophobicity, and other are positive values having hydrophilicity as 1.83, 2.56, 2.74, 4.28 and 5.06 of IL06, IL04, IL03, IL05, and IL01, respectively. The bond dipole moment is the idea of an

electric dipole moment to measure the polarity of a chemical bond within a molecule. In view of pharmaceutical industries, the dipole moment was a parameter for the drug by which a drug is to be used open or close packet. If any drug has a dipole moment, it can be able to absorb the ultraviolet light and have a possibility of properties. The five optimized ILs show zero dipole moment so that it can be used without any protection from UV or sunlight.

4.3. Correlation in case of substituent groups in anions

The value of π (π), MR, and can be calculated as the following equation from Table 4. π , MR, SA = LogP of cholinium benzoate -LogP of cholinium benzoate derivative. From Table 5, it was accounted for the correlation on basis of their different substituent groups in cation, while the F and NO₂ show the highest biological activity.

5. CONCLUSIONS

As the cholinium cation is bioactive molecules, some benzoate anions have attached to form new theoretical ILs and use the computational tools to predict their activity using DFT method. It is summarized that the result optimized molecules of cholinium based ILs like cholinium benzoate, cholinium-2-nitro-benzoate, cholinium -2-methylbenzoate, cholinium -2-hydroxy benzoate, cholinium -2-chlorobenzoate, and cholinium -2-fluorobenzoate were recorded. To make a comparative study among all for the physical properties, chemical reactivity and biological activity, a computational method was used. From the LogP value, it can be said that all ILs are hydrophobic, trending to bioactive. There are five substituent groups in anion as benzene ring at which the nitro group has more active in biological properties.

Conflict of interests

Authors declare that there is no a conflict of interest with any person, institute, company, etc.

REFERENCES

- Hanke, C.; Price, S.; Lynden-Bell, R. *Mol. Phy.* **2001**, 99, 801-809.
- Zhao, H.; Xia, S.; Ma, P. *J. Chem. Tech. & Biotech.* **2005**, 80, 1089-1096.
- Ferraz, R.; Branco, L. C.; Prudencio, C.; Noronha, J. P.; Petrovski, Ž. *ChemMedChem.* **2011**, 6 (6), 975-985.
- Hossain, Md. I.; Kumer, A.; Begum, S. H. *Asian J. Phys. Chem. Sci.* **2018**, 5 (1), 1-9.
- Hossain, Md. I.; Bhuiyan, Md. M. H.; Kumer, A. *Asian J. Phy. Chem. Sci.* **2018**, 5 (3), 1-9.
- Hossain, Md. I.; Kumer, A. *Asian J. Chem. Sci.* **2017**, 3 (4), 1-10.
- Juneidi, I.; Hayyan, M.; Hashim, M. A. *RSC Adv.* **2015**, 5, 83636.
- Dias, A. R.; Costa-Rodrigues, J.; Fernandes, M. H.; Ferraz, R.; Prudêncio, C. *ChemMedChem* **2017**, 12, 11-18.
- Zeisel, S. H. *Nutrition*, 2000, 16 (7-8), 669-671.
- Sarker; Md. N.; Kumer; A.; Islam, J. M.; Paul, S. *Asian J. Nanosci. Mater.* **2019**, 2, 439-447.
- Kumer, A.; Sarker, Md. N.; Paul, S. *Int. J. Chem. Technol.* **2019**, 3, 26-36.
- Kumer, A.; Paul, S.; Sarker, Md. N.; Islam, M. J. *Int J. New. Chem.* **2019**, 6, 236-253.
- Islam, M. J.; Sarker, Md. N.; Kumer, A.; Paul, S. *Int. J. Adv. Biol. Biomed. Res.* **2019**, 7, 318-337.
- Paul, S.; Kumer, A.; Sarker, Md. N.; Islam, M. J. *Int. J. Adv. Biol. Biomed. Res.* **2020**, 8 (2), 112-127.
- Kumer, A.; Sarker, Md. N.; Pual, S. *Eurasian J. Env. Res.* **2019**, 3, 1-10.
- Kumer, A.; Sarker, Md. N.; Paul, S.; Zannat, A. *Adv. J. Chem. A.* **2019**, 2, 190-202.
- Kumer, A.; Sarker, Md. N.; Paul, S. *Turkish Comp. Theo. Chem.* **2019**, 3 (2), 59-68.
- Tsuneda, T.; Song, J. W.; Suzuki, S.; Hirao, K. *J. Chem. Phys.* **2010**, 133, 174101.
- Silva, F. A.; Siopa, F.; Figueiredo, B. F.; Gonçalves, A.M.; Pereira, J. L.; Gonçalves, F.; Coutinho, J. A.; Afonso, C. A. Ventura, S. P. *Ecotox. Environ. Safe.* **2004**, 108, 302-310.
- Araújo, J. M.; Florindo, C.; Pereiro, A. B.; Vieira, N. S.; Matias, A. A.; Duarte, C.M.; Rebelo, L. P.; Marrucho, I. M. *RSC Adv.* **2014**, 4, 28126-28132.
- Young, D. *Computational chemistry: a practical*

DOI: <http://dx.doi.org/10.32571/ijct.648409>

E-ISSN:2602-277X

guide for applying techniques to real world problems.
1st ed; John Wiley & Sons, New York, 2004.

22. Bickelhaupt, F. M.; Baerends, E. J.. *Rev. Comput. Chem.* **2000**, 15, 1-86.

23. Dudek, A. Z.; Arodz, T.; Gálvez, J. *Comb. Chem. High T. Scr.* **2006**, 9, 213-228.

ORCID

 ID <https://orcid.org/0000-0002-2121-1574> (A. Zannat)

 ID <https://orcid.org/0000-0001-5136-6166> (A. Kumer)

 ID <https://orcid.org/0000-0003-2760-0113> (M. N. Sarker)

 ID <https://orcid.org/0000-0001-7739-4018> (S. Paul)